Calcined clay and slag based alkali-activated materials

An experimental investigation for 3DCP

Youssra Boudouan

TU Delft

Bos Witteveen

Calcined clay and slag based alkali-activated materials

An experimental investigation for 3DCP

by

Youssra Boudouan

to obtain the degree of Master of Science
at the Delft University of Technology
to be defended publicly on March 21, 2023

Chair:	Prof.dr.ir Guang Ye
Thesis committee:	Dr.ir. Hua Dong
	Dr.ir Yu Chen
	Ir. Roel Schipper
External advisor:	Ir. Hans Laagland
Place:	Faculty of Civil Engineering, Delft
Project Duration:	May, 2022 - March, 2023
Student number:	4688066

An electronic version of this thesis is available at http://repository.tudelft.nl/.

Faculty of Civil Engineering · Delft University of Technology

”Everything is theoretically impossible, until it’s done”
- Robert A. Heinlein

Acknowledgement

Back in 2020, I first became familiar with the topic of 3D-printed concrete printing. From the very beginning, I was intensely intrigued by this topic. As my bachelor's thesis was about alkali-activated concrete, it only would make sense to combine the use of alkali-activated materials in 3D-concrete printing. I'm so glad that I got the opportunity to contribute to this innovative manufacturing method by doing this master's thesis. In the end, human curiosity will always remain the greatest driving force for innovation.

I want to take this opportunity to thank several people that helped establish this master's thesis. First of all, I would like to thank my daily supervisors, Hua Dong and Yu Chen, for their advice and support, while providing me with freedom to steer the project in the direction I wanted. Furthermore, I would like to thank professor Guang Ye for his critical view and encouragement during the project. I would also like to thank my supervisor Hans Laagland and Maartje Hoogeveen from Witteveen+Bos for the detailed discussions about use of 3DCP in practice. They provided me with all the information to bridge the gap between academic research and industry to ensure that my research is useful for the industry. Last but not least, I want to express my heartfelt gratitude for the unconditional support of my family and friends.

While working on this topic, I gained much appreciation for academics doing their bits to steer research in a more sustainable and innovative direction. I loved doing research and performing experiments, as I finally got the opportunity to link theory to practice. At last, I can say that I am happy with the end result. I can only hope that this thesis can contribute to your knowledge. Enjoy reading!

Youssra Boudouan
Rotterdam, March 2023

Summary

Concrete has been a popular building material for centuries. However, the use of concrete has one major downside: its colossal carbon footprint. At least 8% of the total carbon dioxide emissions is caused by concrete production *(Cement and Concrete: The Environmental Impact, 2020)*.

Additive manufacturing offers many opportunities to improve the sustainability of concrete as a building material. Compared to conventional construction processes, additive manufacturing offers a reduction in amount of labour, on-site construction time and material wastage, while offering more architectural freedom to create complex geometries. Additive manufacturing may therefore reduce the total amount of costs, while providing a more sustainable construction process. By replacing Ordinary Portland cement by an alkali-activated material, the environmental footprint can be further improved. Alkali-activated materials (AAMs) are considered to be a low carbon alternative to cement. The use of industrial by-products in AAMs, like fly ash and blast furnace slag, prevents exhaustion of natural resources, the deposition of material in landfills and high CO_2-emissions, hence resulting in a lower environmental footprint. Industrial by-products like fly ash and slag are relatively cheap and abundantly available at the moment, but this may change in the near future. As a result of the 'Betonakkoord' and decreasing levels of coal-fuelled power generation, the availability of fly ash and blast furnace slag will strongly decrease after 2030, due to effective usage in manufacturing of blending cements and concrete.

In the last couple of decades, the use of metakaolin, i.e. high purity calcined clay, has been extensively studied as an aluminosilicate source for concrete. As this high purity kaolin clay is used in different industries as well, there is a competing demand for this material. Lower grade calcined clay is considered to be a more cost-effective alternative, as less intensive purification is needed, while the supply is much larger. As a replacement for fly ash, low-grade calcined clay will be used as an aluminosilicate source.

This research is dedicated to the development of an alkali-activated calcined clay and slag-based material, specifically for the purpose of 3D-printing. The relationship between calcined clay content, fresh properties, mechanical properties, hydration and shrinkage is investigated, with a specific focus on 3D-printing applications. Furthermore, the potential of using calcined clay and slag based AAMs for 3D-concrete printing (3DCP) is assessed.

The study shows that partial replacement of blast furnace slag by calcined clay in AAMs results in a delayed setting, caused by the low CaO-content in calcined clay and the much lower reactivity compared to slag as a result of a lower amorphous content. The static yield stress, the dynamic yield stress and the initial storage modulus increase when calcined clay is incorporated into the binder. This effect is attributed to the larger specific surface area and total pore area of calcined clay compared to blast furnace slag. More water is adsorbed onto the surface of calcined clay particles and also absorbed into the open pores, therefore reducing the effective water to binder ratio. As less water is actually present in the alkali solution, separation of the particles is reduced. This ultimately results in a higher static and dynamic yield stress.

Calcined clay does not benefit the green strength evolution of slag-based AAMs. Extrusion is positively affected by addition of calcined clay. As a result of the decelerated setting, the printability window will increase and less pressure is needed for extrusion of the material. Furthermore, drying shrinkage and autogenous shrinkage increase with addition of calcined clay. The mechanical properties are improved for increasing calcined clay content in the binder. Results from isothermal calorimetry and thermogravimetric analysis suggest that calcined clay does not contribute to chemical reactions at early ages and is acting as a filler in an alkali-activated system. The improved compressive strength is probably a result of the denser microstructure and the smaller pores. Introducing calcined clay in slag based AAMs contributes to pore refinement and therefore a denser microstructure.

All in all, it can be concluded that the use of calcined clay and slag based AAMs is ineffective for 3D-printing applications. Although the mixtures with calcined clay show good rheology, green strength evolution, workability and mechanical properties, drying shrinkage and setting might still be a big issue. The mixture with 20% calcined clay shows a drying shrinkage that is four times larger than the target value.

In general, AAMs already show a drying shrinkage that is much larger than OPC-based cementitious materials. Introducing calcined clay into an AAM might even further increase the total drying shrinkage. As of now, it is not recommended to use this material for 3D-printing applications. Introducing admixtures might help in solving these problems, so that an application in 3DCP can be possible in the future to account for the lower supply of fly ash and blast furnace slag. Regarding the role of calcined clay in an alkali-activated system: it is highly probable that calcined clay mostly acts as a filler at early-ages in an alkali-activated system, hence the pore refinement, and barely contributes to gel formation. If it does contribute to gel formation, the gel is probably very porous and inhomogeneous.

There is still a lot of research that needs to be conducted to further improve the mixture designs. Admixtures and additives need to be introduced to further optimize the properties for an actual application in 3DCP. Problems related to shrinkage and fast setting need to be solved to ensure that the proposed mixture can be actually used in the industry. Furthermore, the use of this type of calcined clay is only recommended in small quantities (<20% in mass of the binder) for optimal performance. If the goal is to have a higher replacement of slag by calcined clay, the alkali-activator needs to be adjusted accordingly. The use of a stronger, more concentrated alkali activator is key in promoting more gel formation by calcined clay. Furthermore, more research is needed to properly describe the influence of calcined clay on reaction kinetics of AAMs. This study will provide a proper basis for further research.

Contents

Nomenclature

List of Abbreviations

AAM	Alkali-activated material
BET-SSA	Brunauer–Emmett–Teller specific surface area
BFS	Blast furnace slag
CC	Calcined clay
CC/BFS	Calcined clay to blast furnace slag mass ratio
FA	Fly ash
GGBFS	Ground granulated blast furnace slag
M NaOH	Molarity of Sodium Hydroxide solution
MIP	Mercury intrusion porosimetry
MK	Metakaolin
Ms	Modulus
OPC	Ordinary Portland cement
SAOS	Small amplitude oscillatory shear
SH	Sodium hydroxide
SS	Sodium silicate
TGA	Thermogravimetric analysis
W/B	Water to binder ratio
XRD	X-ray diffraction
XRF	X-ray fluorescence

List of Symbols

σ	Pore pressure
$\sigma_{c,1d}$	1-day compressive strength
$\sigma_{c,3d}$	3-day compressive strength
$\sigma_{c,7d}$	7-day compressive strength
τ	Shear stress
$\tau_{0,dyn}$	Dynamic yield stress
$\tau_{0,stat}$	Static yield stress
θ	Contact angle of liquid
n	Power index that represents the deviation from the Bingham behaviour
t	Time
$\dot{\gamma}$	Shear rate
γ	Surface tension of pore solution
K	Plastic viscosity
P	Pressure
r	Radius of the menisci

List of Figures

List of Tables

1

Introduction

1.1. Motivation for this research

Concrete has been used for the construction of buildings, roads, bridges and more for centuries. Concrete structures have proven to be strong and resilient, as they have survived wars and natural disasters. Concrete as a construction material is abundant, locally available and can be used for a variety of purposes. Besides the strength, durability and versatility of the material, concrete is also relatively cheap compared to other building materials, such as steel and wood. For this reason, concrete is the most used substance on the planet after water. According to the *Global Cement and Concrete Association (2020)*, roughly 14 billion m^3 of concrete is produced in the year 2020. This number is only expected to grow in the following years, as a result of a growth in world population.

The use of concrete has one major downside: its colossal carbon footprint. The production of Ordinary Portland cement (OPC) is very energy intensive and therefore a major generator of carbon dioxide, which is considered to be a potent greenhouse gas. High CO_2-emissions are caused by calcination of limestone and combustion of fossil fuel during an energy intensive production process. At least 8% of the total carbon dioxide emissions is caused by concrete production (Fig. 1.1).

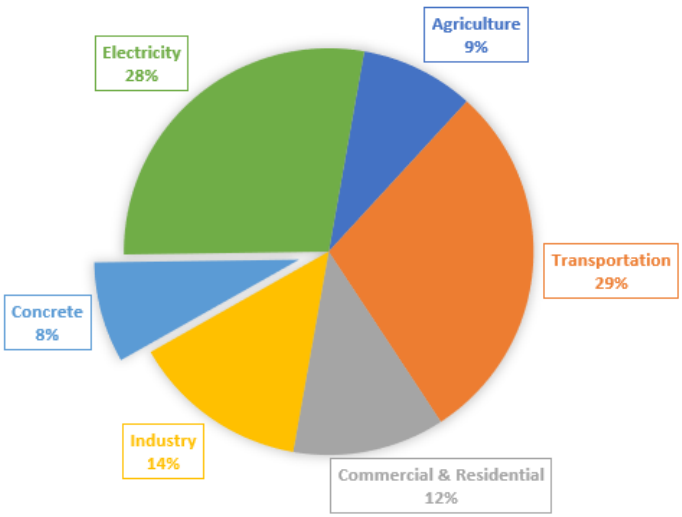

Figure 1.1: Global CO_2-emission by category. *(Cement and Concrete: The Environmental Impact, 2020).*

Additive manufacturing offers many opportunities to improve the sustainability of concrete as a building material. Compared to conventional construction processes, additive manufacturing offers a reduction in amount of labour, on-site construction time and material wastage, while offering more architectural freedom to create complex geometries. Additive manufacturing may therefore reduce the total amount of

costs, while providing a more sustainable construction process. In Fig. 1.2, Fig. 1.3 and Fig. 1.4, examples of projects are given in which additive manufacturing is used for construction.

However, to satisfy the requirements for 3D-printed concrete, larger quantities of Portland cement are used in the printable mixtures compared to traditional concrete to ensure good mechanical performance. To further improve the sustainability of this construction method, Portland cement needs to be replaced by alternative materials with a lower environmental footprint.

Figure 1.2: 3D-printed homes in Eindhoven. *(Parkes, 2022).*

Figure 1.3: 3D-printed house from mud, in which less than 6 kW of energy is consumed for production. *(Iago Corazza, 2021).*

Figure 1.4: 3D-printed bridge in Shanghai, with a length of 26.3 m. *(Ravencroft, 2022).*

By replacing Ordinary Portland cement by an alkali-activated material, the environmental footprint can be further improved. Alkali-activated materials (AAMs) are considered to be a low carbon alternative to cement. Alkali-activated materials are inorganic polymers acting as the binder agent in concrete, often containing by-products from the industry such as fly ash and blast furnace slag *(Davidovits, 1989)*. Unlike Ordinary Portland cement, AAMs are synthesized by activation of an aluminosilicate source (fly ash, slag) with alkaline activators. The use of industrial by-products prevents exhaustion of natural resources (limestone), the deposition of material in landfills and high CO_2-emissions, hence resulting in a lower environmental footprint. Carbon emission reductions vary between 40 and 80% compared to OPC *(GCCA, 2020)*. For the aforementioned reasons, AAMs have attracted a lot of attention in the industry. The material also shows advanced mechanical properties and greater durability. According to the *Global Cement and Concrete Association (2020)*, AAMs develop high strength at early ages and show good performance in exposure conditions, indicating a good resistance to chemically-aggressive environments and high temperatures.

Industrial by-products like fly ash and slag are relatively cheap and abundantly available at the moment, but this may change in the near future. As the share of geopolymer concrete in concrete production is still limited, there are currently hardly any supply problems for fly ash and blast furnace slag. However, as a result of the *Betonakkoord*, the availability of fly ash and blast furnace slag will strongly decrease after 2030, due to effective usage in manufacturing of blending cements and concrete. The *Betonakkoord* contains an agreement between various big players in the concrete industry, in which they aim to bring down the CO_2-emissions in the Netherlands with 30% by 2030 and in which 100% high quality reuse of concrete waste will be the norm, therefore fully closing the cycle. Also, due to decreasing levels of coal-fuelled power generation and the move towards natural gas and renewable energy sources, availability of fly ash will decrease even more, especially for the Netherlands. The availability and supply of industrial by-products like fly ash and slag is therefore quite uncertain in a couple of years.

In the last couple of decades, the use of metakaolin, i.e. high purity calcined clay, has been extensively studied as an aluminosilicate source for concrete. As high purity kaolin clay is used in different industries as well, there is a competing demand for this material. This competing demand for metakaolin and the intensive purification process to obtain metakaolin from kaolinite clay, both contribute to a relatively high price *(Zhou et al., 2017)*. A lower grade calcined clay is considered to be a more cost-effective alternative, as less intensive purification is needed, while the supply is much larger.

1.2. Research aim and questions

Combining the use of AAMs in an innovative and automated 3D-printing process may offer many advantages for the construction industry. As the demand of fly ash and slag is questionable in the near future, more research is needed in which the focus is shifted to alternative materials. This research is therefore devoted to the development of an alkali-activated calcined clay and slag-based material, specifically for the purpose of 3D-printing. The relationship between calcined clay content, fresh properties, mechanical properties, hydration and shrinkage is investigated, with a specific focus on 3D-printing applications.

The research questions are as follows:

Research Question 1

What is the influence of calcined clay content on fresh properties, mechanical properties, hydration and shrinkage behaviour of calcined clay and slag based AAMs?

Research Question 2

To what extent is calcined clay and slag based AAM interesting for use in 3DCP?

1.3. Outline of thesis

In Fig. 1.5, the outline of the thesis is illustrated. In part I, a literature review is presented, followed by the research framework and design. Part II includes the results and analysis of the results. Last but not least, in part III, the conclusions and recommendations for further research are presented.

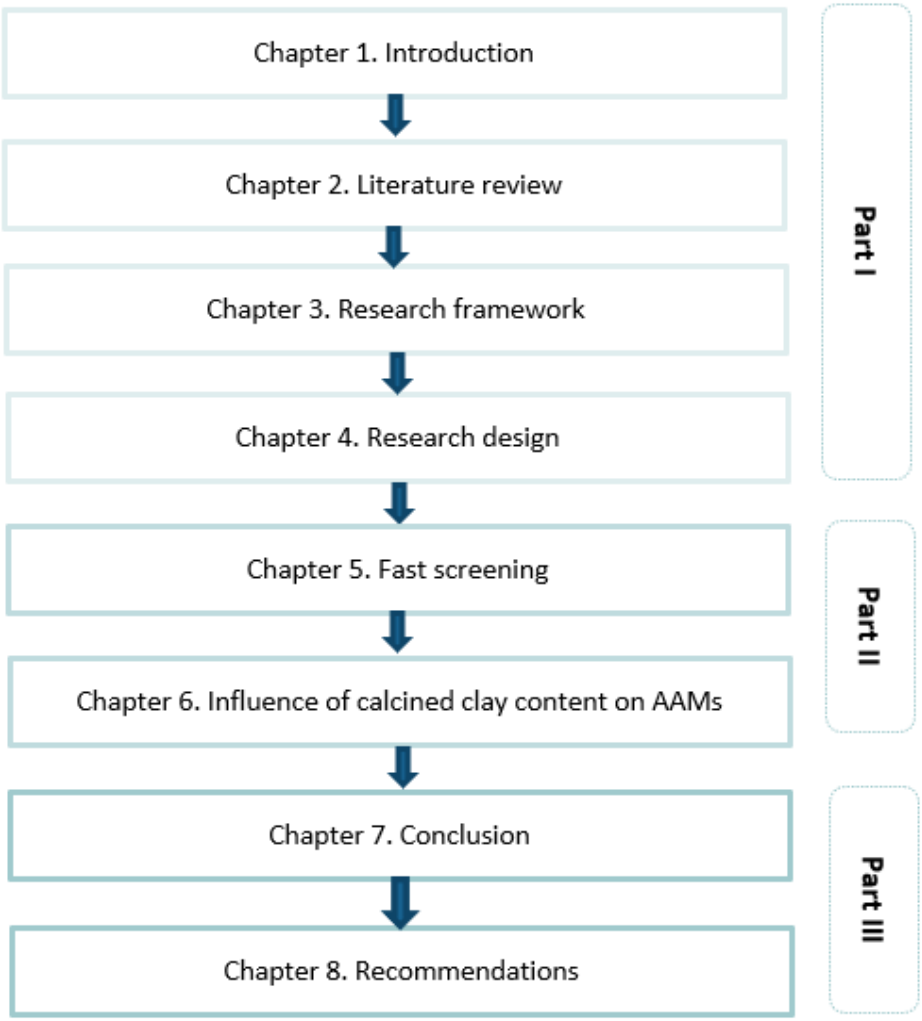

Figure 1.5: Thesis outline.

Part I

Literature review and research design

2

Literature Review

2.1. Calcined clay versus slag and fly ash in AAMs

To reduce the CO_2-emissions caused by concrete manufacturing, there is a growing interest in alternative and low CO_2-binders. A great example of alternative binders are alkali-activated materials (AAMs). Alkali-activated materials are inorganic polymers acting as the binder agent in concrete, often containing by-products from the industry such as fly ash and blast furnace slag *(Davidovits, 1989)*. Unlike OPC, AAMs are synthesized by activation of an aluminosilicate source with alkaline activators. AAMs have attracted a lot of attention in the industry. AAMs based on fly ash and blast furnace slag are currently very popular in the construction industry. Fly ash and slag are relatively cheap and abundantly available at the moment, but this may change in the near future. As the share of alkali-activated concrete in concrete production is still limited in the Netherlands, there are currently hardly any supply problems for fly ash and blast furnace slag.

In the next couple of years, the trade perspective of fly ash (vliegas) and slag (hoogovenslak) is considered to be negative, signifying that their availability will become a problem for the Netherlands in the near future. According to *Betonhuis (2021)*, the trade perspective of calcined clay (gecalcineerde klei) is positive (Fig. 2.1). Calcined clay is produced by heating kaolin clay at high temperatures in the range of 600-900 °C. Kaolinite (kaolin clay) is a naturally occurring mineral. This type of clay is abundantly available in the world, especially in Europe. According to *Sousa (2017)*, Belgium, Germany, France and Spain are among the largest exporting countries of kaolin clay. This type of clay is not present in the Netherlands, but it can be imported from countries nearby.

As a result of the *Betonakkoord* in the Netherlands, the availability of fly ash and blast furnace slag will strongly decrease after 2030, due to effective usage in manufacturing of blending cements and concrete. The *Betonakkoord* contains an agreement between various big players in the concrete industry, in which the aim is to reduce CO_2-emissions in the Netherlands with 30% by 2030 and in which 100% high quality reuse of concrete waste will be the norm. Also, due to decreasing levels of coal-fuelled power generation and the move towards natural gas and renewable energy sources, availability of fly ash will decrease even more. Therefore, it can be concluded that availability of industrial by-products such as fly ash and slag is quite uncertain for the Netherlands after the year 2030. From a long term point of view, it's therefore important to consider alternative materials for use in AAMs.

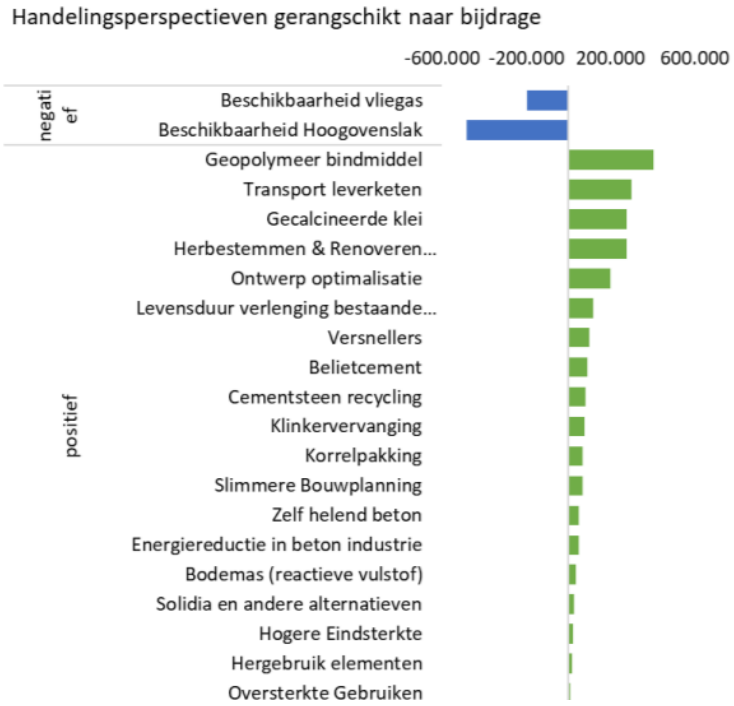

Figure 2.1: Trade perspective of various materials in concrete ranked according to their contribution, according to concrete manufacturer *Betonhuis (2021)*.

In the last couple of decades, the use of metakaolin, e.g. high purity calcined clay, has been extensively studied as an aluminosilicate source for concrete. As high purity calcined clay is used in different industries as well, there is a competing demand for this material. This competing demand for metakaolin and the intensive purification process to obtain metakaolin from kaolinite clay both contribute to a relatively high price *(Zhou et al., 2017)*. Calcined clay (low and/or high grade) is considered to be a more cost-effective alternative, as less intensive purification is needed, while the supply is much larger. Large supply is a result of enormous clay reserves due to clay waste generated by the ceramics industry and construction industry *(Lopez et al., 2009)*. The reactivity of calcined clay typically depends on the calcination process of kaolinite clay, as metakaolin, e.g. the reactive component in calcined clay, is formed during heating at high temperatures (600-900 °C). The environmental footprint of calcined clay is much lower than many construction materials. For comparison, the practical calcination temperature of Ordinary Portland Cement is around 1425-1500 °C, which is considerably larger than calcination temperature of metakaolin. According to *Hanein et al. (2021)*, the estimated CO_2-emission of metakaolin is smaller than 270 g CO_2 per kg, while the estimated CO_2-emission of OPC is around 809 g CO_2 per kg. This proves that the environmental footprint of calcined clay is much lower than the footprint of OPC.

Considering the worldwide abundance of calcined clay, as well as the low CO_2-footprint during production, calcined clay is highlighted as an alternative to fly ash and slag in manufacturing of AAMs. In this paragraph, calcined clay, fly ash and slag will be compared, with a special focus on use in AAMs.

2.1.1. Chemical and physical composition of calcined clay, fly ash and slag

Kaolinite [$Al_2Si_2O_5(OH)_4$] is a naturally occurring (abundant) mineral in the earth's crust. Raw clays usually have low or moderate pozzolanic reactivity. To activate the clay, e.g. to increase the reactivity of kaolinite, it is heated at high temperatures in the range of 600-900 °C. It is important to limit the heating temperature during the calcination of kaolin-containing clay, as the over-calcination of kaolinite clay reduces its reactivity. Generally, the production of calcined clay is done with carefully controlled heat treatment of kaolin at 700–800 °C for optimal properties *(Shvarzman et al., 2003)*. During the activation process, clay minerals undergo processes of dihydroxylation and amorphization, which results in a change in coordination of the Al-ions. Dihydroxylation refers to the loss of water, e.g. tearing off of OH-groups in the O-layer, causing a collapse of the structure and the formation of a new amorphous phase. The process of dihydroxylation

also results in increased exposure of Al-ions on the surface of mineral grains, hence greater solubility of the Al- and Si-ions, accompanied by a greater reactivity. The post-heating amorphous phase that is formed during heating is also known as **metakaolinite** [$Al_2O_3.2SiO_2$], e.g. **metakaolin**. The reactivity of calcined clay typically depends on the calcination process of kaolinite clay, as this determines the metakaolin (reactive) content in calcined clay. Metakaolin is formed during heating at high temperatures. Based on the calcination process, either low or high grade calcined clay is obtained.

In Fig. 2.2, both rotary kiln calcined clay and flash calcined clay under two magnifications (5 and 50 μm) are depicted. Calcined clay mainly consists out of hexagonal plates and clusters of plates *(Nguyen et al., 2020)*. Spherical particles with sizes between 5 and 10 μm are only detected in flash calcined clay, therefore indicating that the calcination process influences the morphology of calcined clay particles greatly. The usability of calcined clay as a source of aluminosilicates in alkaline activation depends on the particle size, purity and crystallinity of the initial kaolinite. *Li et al. (2010)* states that as a rule, the particles should be under 5 μm.

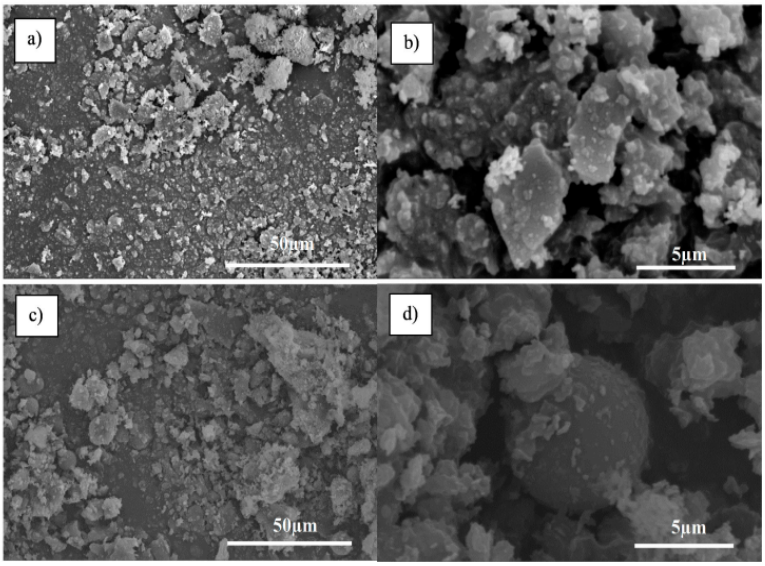

Figure 2.2: SEM images of calcined clays. (a,b): Rotary kiln calcined clay. (c,d): Flash calcined clay. *(Nguyen et al. 2020)*.

Fly ash is another pozzolanic industry by-product and is formed during coal combustion. Fly ash is the finest, heterogeneous residue after burning coal in boilers. It rises with flue gases and is captured by special filters before entering the chimneys.

The properties of fly ash vary significantly depending on the source and composition of the burned coal. Silica (SiO_2), aluminium oxide (Al_2O_3) and lime (CaO) are the main chemical components that are present in fly ash. The mineralogy of fly ash is very diverse: main phases are a glass phase, together with quartz, mullite and the iron oxides hematite, magnetite and/or maghemite. Other trace elements can be found in fly ash as well, depending on the composition of the burned coal.

According to the *American Society for Testing and Materials (ASTM) C618*, fly ash can be classified into two main groups, depending on the content of calcium, silica, alumina and iron:

1. **Class F**: This type of fly ash contains a lime (CaO) content of less than 7% and is pozzolanic in nature. It is a product of burning harder, older anthracite and bituminous coal. It is the most abundant type of ash and is frequently re-used. Class F fly ash requires either a cementing agent (OPC) to produce cementitious compounds or some kind of alkaline activator to form a geopolymer. This type of fly ash is most often used for geopolymer synthesis.
2. **Class C**: This type of fly ash contains more than 20% of lime (CaO). It is a product of burning younger lignite or sub-bituminous coal. As a result of its pozzolanic and self-cementing properties, no alkaline activator or cementing agent is needed to form a gel that strengthens over time. Solely in the presence of water, the materials hardens rapidly and gains strength over time. Alkali and sulphate is higher in class C fly ash, in comparison to class F fly ash.

Morphology of coal fly ash shows that the particles are spherical in shape with some irregular shaped particles in agglomerated form (Fig. 2.3). A spherical particle shape generally contributes to an increase in flowability by packing of material when used in concrete.

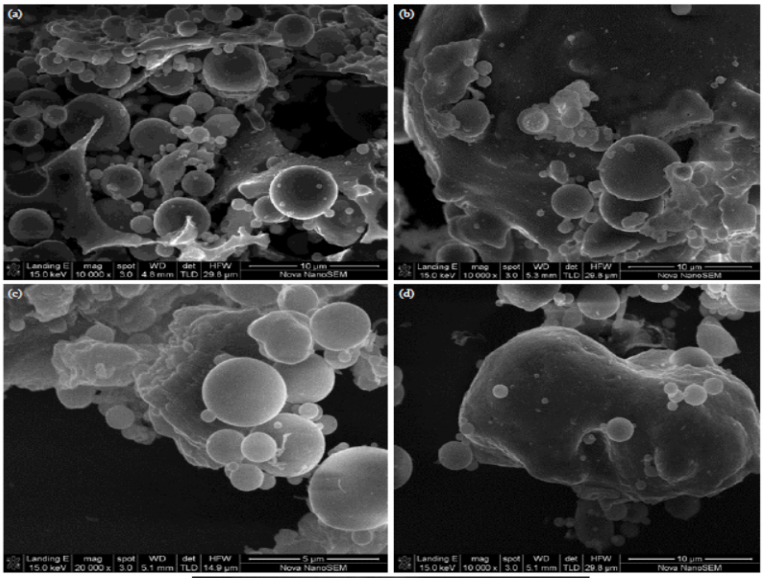

Figure 2.3: SEM micrographs of coal fly ash from various sources. *(Alegbe et al. 2018)*.

Another popular industrial by-product used in the manufacturing of concrete is **(ground-granulated) blast furnace slag**. Blast furnace slag is a pozzolanic by-product from the steel industry, formed when iron ore or iron pellets, coke and flux (limestone or dolomite) are melted together in a blast furnace, quenched in water or steam, after which the dried product is ground into a fine powder. Properties of blast furnace slag strongly depend on the composition of raw materials in the iron production process. Slag primarily consists out of CaO (35–40%), SiO_2 (25–35%), MgO (5–10%) and Al_2O_3 (5–15%), with traces of S, Fe_2O_3, MnO and K_2O (with percentages of under 1%) *(Provis and van Deventer, 2009)*. Furthermore, slag is highly cementitious and high in calcium silicate hydrates (CSH), a compound that is known to improve strength, durability and appearance of concrete. The shape of blast furnace slag particles is irregular with a glassy surface (Fig. 2.4).

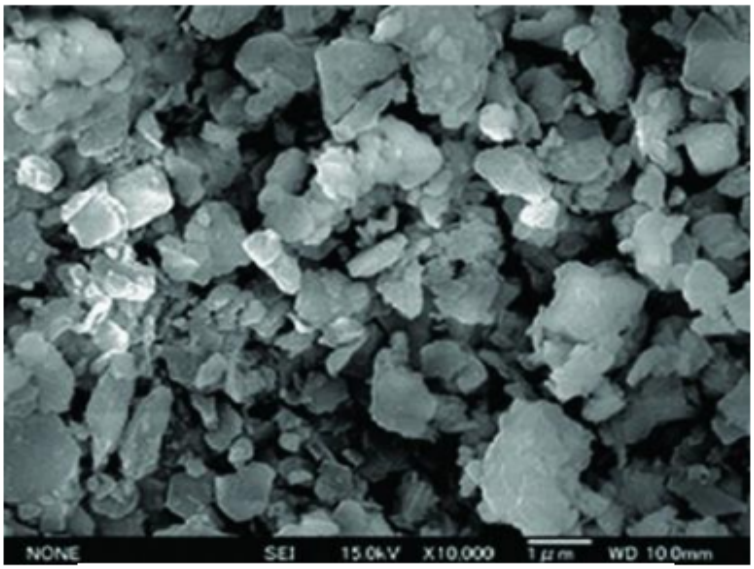

Figure 2.4: Microstructure of blast furnace slag, obtained through field emission scanning electron microscope (FESEM). *(Khan et al., 2014)*.

2.1.2. Reaction mechanisms of calcined clay, fly ash and slag in AAMs

Professor Joseph Davidovits *(1979)* was the first to introduce the term *geopolymer* to classify the family of alkali-activated aluminosilicate binders, now used for a number of industrial applications. Geopolymers are produced from the polycondensation of inorganic compounds and are alkali-activated materials, produced by the reaction of aluminosilicate materials with an alkaline activator. Alkali-activated materials act as the binder agent in concrete, often containing by-products from the industry such as fly ash and blast furnace slag or metakaolin *(Davidovits, 1989)*.

For the manufacturing of AAMs, cementitious components with either hydraulic (OPC, slag) or pozzolanic properties (metakaolin, fly ash) can be used (Fig. 2.5). Alkali-activated materials is considered to be a high potential technology for concrete manufacturing, as both natural materials and industrial by-products can be utilised as main materials.

A wide variety of alkali-activated materials has been developed in the last couple of decades. Based on the nature of the materials, alkaline binders can be grouped into three main categories:

1. High calcium binder ($(Na,K)_2O$-CaO-Al_2O_3-SiO_2-H_2O system)
2. Low calcium binder ($(Na,K)_2O$-Al_2O_3-SiO_2-H_2O system)
3. Hybrid alkaline binder

These three types of alkaline binders will be discussed in the following paragraphs, together with the reaction mechanism of each binder.

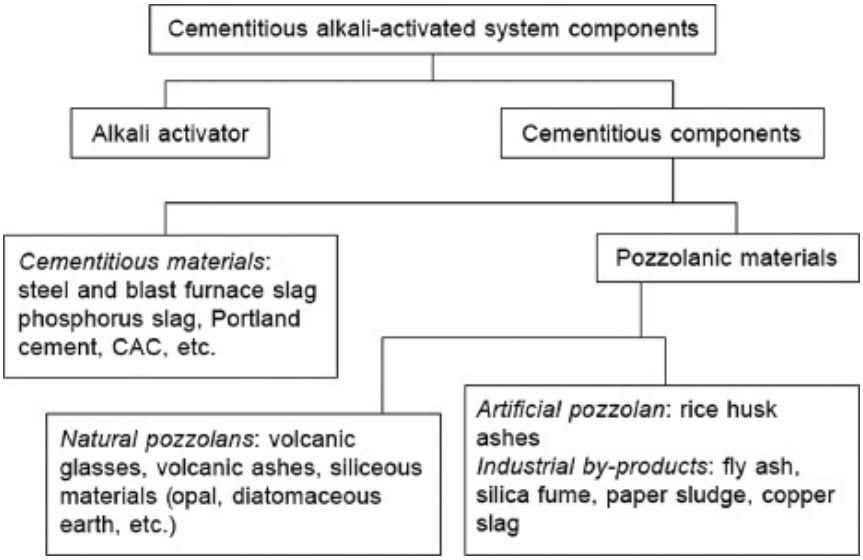

Figure 2.5: Alkali-activated system components *(Garcia-Lodeiro et al., 2015).*

Reaction mechanism high calcium binder
High calcium binders **(**$(Na,K)_2O$-CaO-Al_2O_3-SiO_2-H_2O system**)** include calcium- and silicon- rich materials, like blast furnace slag. They are activated under moderate alkaline conditions without external heating. The main reaction product is C-A-S-H-gel (calcium silicate hydrate gel). The same gel is formed in hydration of Portland cement. *(Garcia-Lodeiro et al., 2015).* Note that calcium rich cements show fast early-strength development compared to low calcium cements. The amorphous phases in blast furnace slag contribute to an increase of the dissolution rate and therefore an accelerated hardening process.

Glukhovsky and Krivenko (1994) have proposed a model to explain the alkaline activation of silica- and lime-rich materials such as blast furnace slag (Fig. 2.6).

$$= \text{Si-O}^- + \text{R}^+ == \text{Si-O-R}$$
$$= \text{Si-O-R} + \text{OH}^- == \text{Si-O-R-OH}^-$$
$$= \text{Si-O-R-}OH^- + \text{Ca}^{2+} == \text{Si-O-Ca-OH} + R^+$$

Figure 2.6: Series of reactions for the alkaline activation of silica- and lime-rich materials, as proposed by *Glukhovsky & Krivenko (1994).*

From the model depicted in Fig. 2.6 can be seen that the alkaline cation (R^+) acts as a catalyzer in the initial phases of hydration by cationic exchange with Ca^{2+}-ions. As reactions advance, the cations are incorporated into the structure. The alkaline activation of slag is considered to be a complex process, in which slag is slowly discomposed, followed by polycondensation of the reaction products. The activation of slag may vary depending on the composition of the slag and also depends on the type and composition of the activator that is used. Sodium hydroxide and waterglass are commonly used to activate blast furnace slag. Regardless of the type of activator, the main reaction product is always C-A-S-H gel with a low Ca/Si ratio *(Wang et al., 1995)*.

Reaction mechanism low calcium binder
In *low calcium binders* ($(Na,K)_2O$-Al_2O_3-SiO_2-H_2O system), the alkaline materials primarily consist out of aluminium and silicon. Examples of such materials are metakaolin and type F fly ash. These materials contain low amounts of CaO and therefore require more aggressive working conditions to activate the alkaline materials at a fast rate, such as higher alkalinity of the activator and elevated curing temperatures.

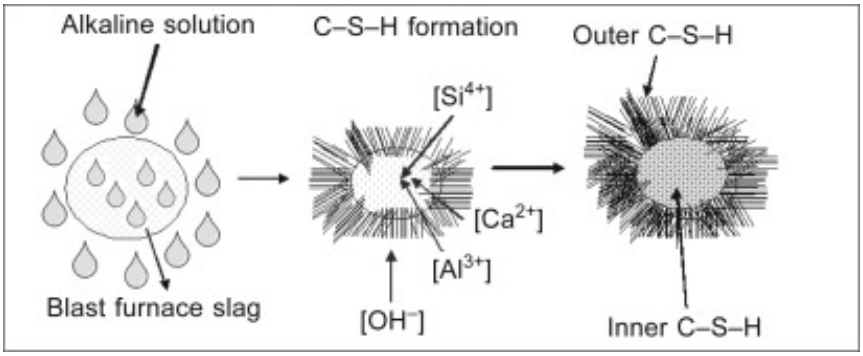

Figure 2.7: Theoretical model for the reaction mechanism in alkali-activated slag.

The main reaction product is N-A-S-H-gel (alkaline aluminosilicate hydrate gel), which is considered to be a zeolite precursor *(Garcia-Lodeiro et al., 2015)*.

Palomo et al. (2005) proposes a model to describe the alkaline activation of low calcium alkaline cement based on zeolite synthesis. The model consists of two stages: 1) nucleation and 2) growth. In the nucleation stage, aluminates dissolve and complex ionic species are formed via polymerisation. In the growth stage, the nuclei reach a critical size and the crystal starts to grow. The final result is an amorphous matrix with main component N-A-S-H gel.

Various authors have revised this model. In the new model, the formation of N-A-S-H gel is established through a series of stages (Fig. 2.8). The aluminosilicate source dissolves into several species (silica and alumina monomers) when it comes into contact with the alkaline solution. These monomers interact and are transformed into polymers. When the solution reaches saturation, N-A-S-H gel precipitates. This gel is initially rich in alumina, as a result of the high Al^{3+} content in the alkaline medium in the early stages, as aluminium dissolves more quickly than silicon. Al-O bonds are weaker than Si-O bonds and therefore easier to break. As reaction progresses, more Si-O is dissolved and consequently, the silicon concentration in the medium and N-A-S-H gel increases.

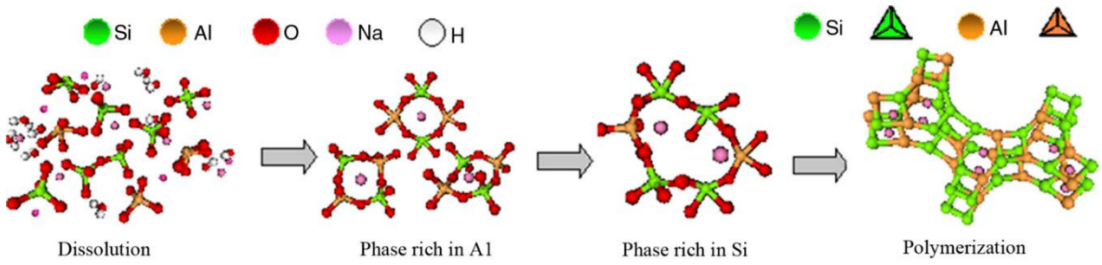

Figure 2.8: Model proposed for N-A-S-H gel formation *(Fernández-Jiménez et al., 2005b; Shi et al., 2011).*

Reaction mechanism blended binder

A third activation model is the combination of high and low calcium binder, often denoted as *blended* or *hybrid alkaline binder*. The reaction products in this third activation model are very complex. Blended binders can be divided into two groups:

1. Materials with low OPC-content and high content of mineral additions (>70%) *(Palomo et al., 2007)*.
2. Blends with no OPC-content.

In the case of a hybrid alkaline or blended binder, a mix of cementitious gels is formed, containing C-A-S-H-gel and (N,C)-A-S-H-gel *(García-Lodeiro et al., 2010a-b)*. Studies have shown that co-precipitation of both gels is possible *(Alonso and Palomo, 2001, Yip et al., 2005, Palomo et al., 2007)*. Recent research has shown that both gels do not develop as two separate gels. Instead, they interact *(García-Lodeiro et al., 2011)*. Research on hybrid binders show that the characteristics of the gel are impacted by the pH and the calcium concentration in the system. In the case of a high calcium content and high pH level, C-A-S-H gel

formation is favoured over N-A-S-H gel formation. Note that little is known about the reaction mechanism of hybrid alkaline cements, especially in the early stages.

Nedeljcovic et al. (2016) states that the combination of low and high calcium binders provides a more uniform development of the microstructure and therefore optimal properties. This indicates the importance of using hybrid alkaline binders in 3DCP for optimal properties. In this study, the focus will therefore be on AAMs containing slag (high calcium binder) and high-grade calcined clay (low calcium binder).

Concluding remarks

As a result of the positive long-term trade perspective of calcined clay in the forthcoming years, it is regarded as an interesting material for use in manufacturing of AAMs. Metakaolin (pure calcined clay) has a higher reactivity than many other pozzolanic materials and has therefore proven to be a valuable admixture for concrete applications, e.g. OPC-concrete with metakaolin as supplementary cementitious material. The high reactivity is often attributed to the relatively high specific surface area (SSA). However, as a result of this high SSA, the water demand is higher to ensure enough workability for casting. It is therefore not often used for mass production of concrete and only used in small quantities. Low- and high-grade calcined clay do not contain 100% metakaolin and therefore show lower reactivity as well as lower water demand. The properties and reactivity strongly depend on the type of clay that is used and its physical and chemical composition, e.g. density, mineralogical composition, specific surface area (SSA), particle size, metakaolin content, thermal treatment history, etc. Furthermore, heat treated natural pozzolans like calcined clay are often used to improve the resistance of concrete to sulphate attack, to mitigate alkali-silica reactions (ASR) and are very useful for applications in which low permeability and very high strength is required.

A disadvantage of using calcined clay in AAMs is the higher concentration of alkali activator that is needed. According to *Provis & Winnefeld (2018)*, calcined clay requires the highest amount of alkaline activator in comparison to fly ash and slag based AAMs. Yet again, this suggests that a blend of different types of cement is ideal to guarantee the best properties and a stable microstructure, while ensuring normal curing conditions (room temperature curing) and moderate alkaline conditions.

2.1.3. Alkaline activator solutions

Not only the type of binder is relevant to describe the properties of AAMs. Alkaline activator solutions are another essential component of AAMs. According to *Glukhovsky et al. (1994)*, six groups of activators can be distinguished, based on their chemical composition:

- Caustic solution: MOH;
- Slightly alkaline, non-siliceous salts: M_2CO_3, M_2SO_3, M_3PO_4, MF;
- Highly alkaline, non-siliceous salts: M_2SO_4;
- Aluminosilicates: $M_2O.Al_2O_3.SiO_2$;
- Silicates: $M_2O.nSiO_2$;
- Aluminates: $M_2O.nAl_2O_3$.

Alkaline solutions containing either hydroxides (caustic solutions) or silicates are typically used to activate the source materials. The type of solution that is used for the activation of the binder agent is essential in explaining the strength development. When using a solution with soluble silicate (sodium silicate), reactions occur at a higher rate than when hydroxides (sodium hydroxide) are used. In case of a soluble silicate as an activator for the binder agent, reaction steps overlap, meaning that dissolution, accumulation of reaction products, and polycondensation of the structures occur simultaneously. Strength development is therefore very fast, resulting in a high early age strength *(Palomo et al., 1999).* Blends of hydroxides and silicates are also common to generate high alkalinity. For AAMs containing slag, sodium silicate is the most suitable activator for good workability and mechanical strength. Silicate-type activators contribute to high strength development at older ages, while the use of hydroxides improve the development of mechanical strength at early ages *(Shi and Qian, 2000)*. When both types of alkaline activators are combined, e.g. a binary alkaline activator, this ensures that characteristics possessed by each alkaline activator can be complementary used. This phenomenon is supported by numerous studies.

Palomo et al. (1999) shows that the addition of waterglass (sodium silicate) to a sodium hydroxide solution (NaOH) for a fly ash based AAM significantly improves the mechanical strength. The same trend is observed for metakaolin based geopolymers. *Granizo et al. (2007)* supports the idea that alkali activation of MK using solution containing sodium silicate and NaOH results in enhanced mechanical strength compared to activation with only sodium hydroxide. For this reason, the alkali activator should contain a silica source, e.g. a water glass solution, in addition to sodium hydroxide for optimal properties. Other important parameters for the alkaline solution are the modulus (M_s) and the sodium oxide content (Na_2O). The sodium oxide content is often described by the sodium oxide to precursor mass ratio.

For this study, a blend of sodium silicate and sodium hydroxide will be used to activate the slag and calcined clay.

2.1.4. Calcined clay in AAMs – an overview

In previous paragraphs, the potential of partially replacing fly ash and/or blast furnace slag with metakaolin is discussed. In this paragraph, the focus will be on examining fresh and mechanical properties of geopolymer concrete in which metakaolin is incorporated. The possibility of incorporating a low-grade calcined clay in AAMs is yet to be explored. For this reason, the focus is on literature in which metakaolin is used in AAMs.

Fresh properties of AAMs containing MK

In the study of *Albidah et al. (2020)*, the influence of four parameters on properties of metakaolin based geopolymer is investigated:

- Sodium silicate to sodium hydroxide solids ratio;
- Alkaline solids to MK ratio;
- Aggregate content and water to solids ratio.

Locally available raw kaolin is calcined at 750°C for 3 h to produce the MK, i.e. calcined clay with 100% metakaolin content. Mixes with low sodium silicate to sodium hydroxide (solids) ratio (in the study 1.3 and 1.6) show low slump and therefore low workability and fast setting. A low sodium silicate to sodium hydroxide ratio is also related to a low modulus (SiO_2/Na_2O molar ratio) of the alkaline activator. A low modulus indicates a high Na_2O content relative to the SiO_2 content, resulting in chemical reactions that occur at a faster rate. Increasing the sodium silicate to sodium hydroxide solids ratio to 2 and 2.5 produces more workable mixes with a slump of about 30 mm. Exceeding a certain limit of the sodium silicate to sodium hydroxide ratio (3.0 in the study) results in a more cohesive mix with lower slump values of 20 mm. In general, it can be concluded that increasing sodium silicate to sodium hydroxide solids ratio improves the workability. Furthermore, *Albidah et al.* reports zero slump for alkaline solids to MK ratios of 0.21, 0.25 and 0.3. An improved workability, i.e. higher slump, is achieved for mixes with higher alkaline solids to MK ratios.

In the study of *Huseien et al. (2018)*, the effect of substituting slag with metakaolin (0-15%) on early strength properties of geopolymer concrete is investigated. Besides the varying metakaolin content, the influence of the moduli of the alkaline solution (1.08–1.26) and the sodium oxide to dry binder ratios (7-13%) on fresh and mechanical properties is reviewed. The study shows an increasing setting time and flow for increasing MK content, i.e. better workability. The reduction in slag content contributes to better flow of the mixture as a result of a reduction in angular particles in the mixture. The fineness in the particle size of MK (75% of the particles smaller than *10* μm) is also mentioned as possible reason for the increase of workability of the geopolymer mortar for increasing MK content. The particle size thus plays an important role in the dissolution process and flow of the mortar. Moreover, MK has a lower calcium content and higher silica and aluminium content than slag. In the case of a high MK content, the calcium content in the mixture is much lower, resulting in decelerated setting. Thus, MK, as part of a binary blended binder, actively decelerates the setting time of geopolymer mortars under ambient curing conditions.

Huseien et al. also reports higher flow of the mortar at lower Na_2O contents, supporting the findings of *Albidah et al.* An increase in Na_2O content (higher molarity of NaOH solution) contributes to an increase in the Na^+-content, a fast rate of chemical reaction and a reduction of the SiO_2:Na_2O content. More heat is released for higher Na_2O content, resulting in a lower flow rate and accelerated setting time (Fig. 2.9). Curing at high temperature can accelerate this reaction rate even further.

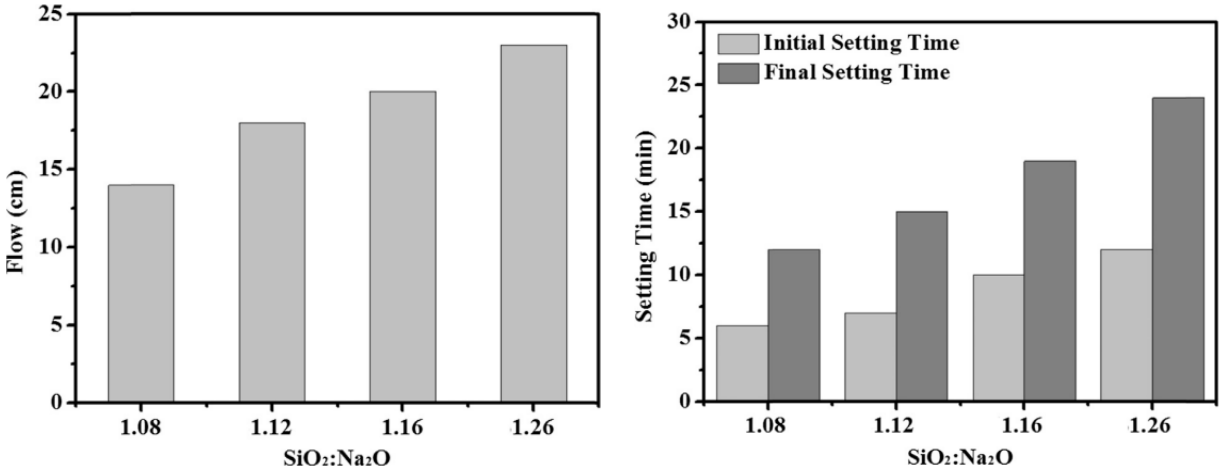

Figure 2.9: Impact of moduli (M_s) of the alkaline solution on the flow and setting time of geopolymer mortar. *(Huseien et al., 2018).*

Huseien et al. reports an increase in flowability for increasing alkali solids to binder ratios. The water content increases for an increasing content of the alkali solids. An increase in water content directly contributes to higher workability of the mixtures. The setting time is also increased considerably for increasing alkali solids to binder ratios (Fig. 2.10).

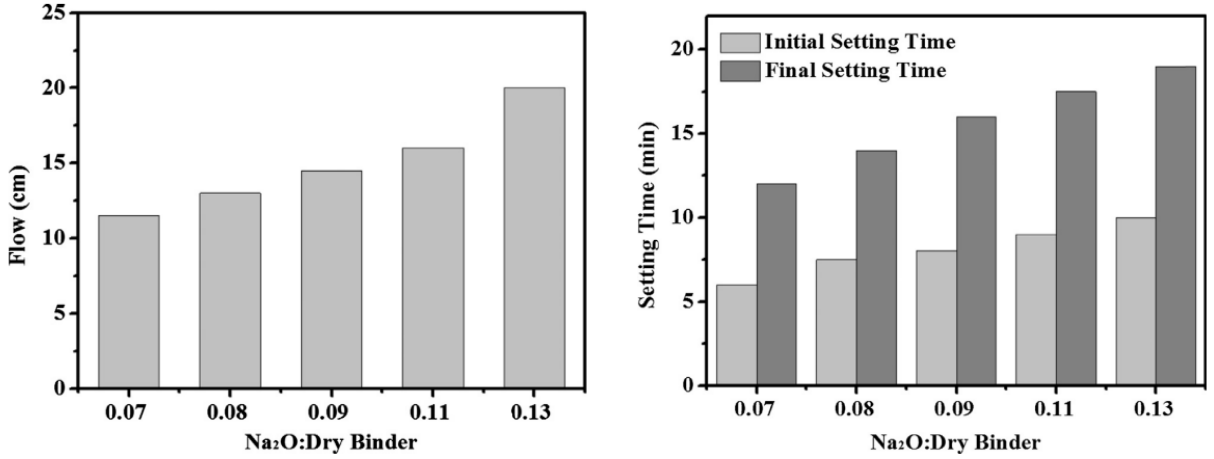

Figure 2.10: Impact of Na_2O:dry binder on the flow and setting time of geopolymer mortar. *(Huseien et al., 2018).*

In the study of *Hasnaoui et al. (2019)*, an optimization approach is presented to find an optimum formulation for a metakaolin and slag based geopolymer mortar. The rheology, porosity and mechanical properties are investigated for various mortar mix designs. Parameters in the study are the slag/metakaolin ratio, the modulus of the alkaline solution and the precursor/activator ratio. An increasing flow time is reported for increasing metakaolin content (Fig. 2.11). A lower flow time indicates greater flowability and workability. This increase in flow time can be assigned to the high fineness and high specific surface area (SSA) of MK. The plastic viscosity of geopolymer mortars are found to increase as well with increasing content of MK, due to an increase in specific surface area. An increase of the modulus contributes as well to an increasing flow time, hence a lower flowability. The silica content in the alkali solution increases for increasing moduli, resulting in a rise in solution viscosity.

The influence of the GBFS/MK ratio and MR on the setting time is reported as well in this study. Mixtures with high slag content show a low initial and final setting time (Fig. 2.12). The accelerated setting is caused by the high calcium content (CaO) in GBFS. This result is in accordance with the findings of *Huseien et al.*,

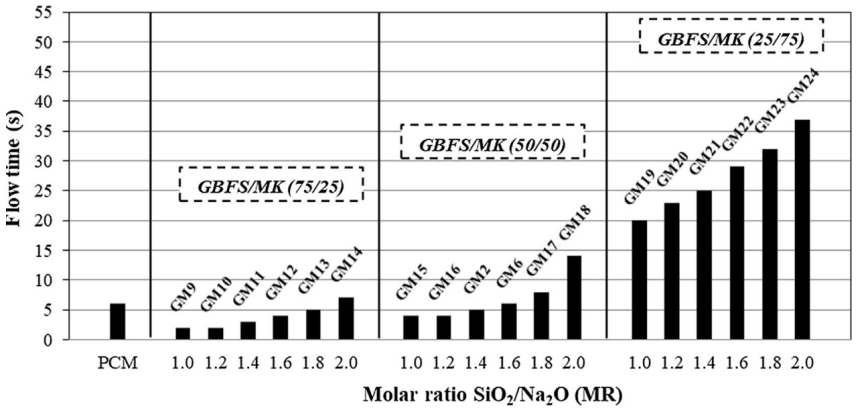

Figure 2.11: Flow time of Portland cement and geopolymer mortars. *(Hasnaoui et al., 2019).*

in which accelerated setting is found for higher slag content. No clear correlation is found for the modulus and the setting time of the different geopolymer mixtures.

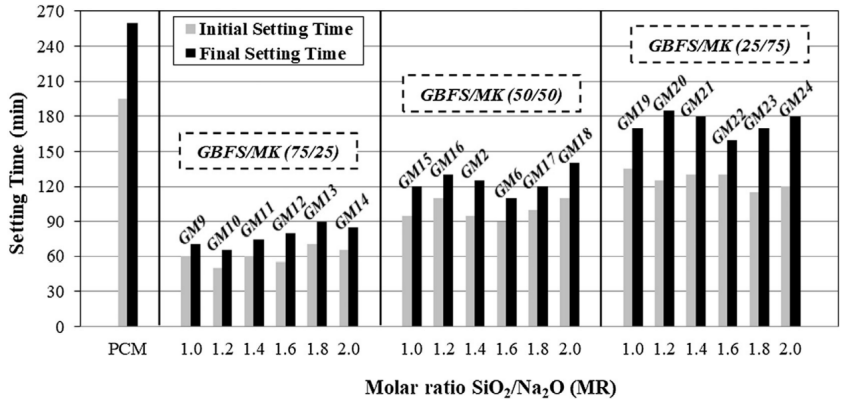

Figure 2.12: Initial and final setting time of Portland cement and geopolymer mortars. *(Hasnaoui et al., 2019).*

Alanazi et al. (2017) has studied the effect of modifying the modulus of the alkaline solution (0.8-1.8) and the effect of partially replacing metakaolin by slag (30%) by focusing on the early strength and durability of the geopolymer pastes. This study shows that partially replacing the metakaolin with slag (30%) results in an increase in workability and an decelerated setting time. In other studies, an increase in slag content typically contributes to accelerated setting.

In the study of *Favier et al. (2014)* , the flow properties of metakaolin based geopolymers are described and compared to Ordinary Portland Cement. Metakaolin-based geopolymers are described as Newtonian fluids in the study and the viscosity is mainly determined by the properties of the alkaline solution instead of the contact between metakaolin particles. In the case of OPC, viscosity mainly depends on colloidal interaction between the particles. This implies that additives and admixtures used for OPC-based materials will not be efficient in controlling the rheological behaviour of geopolymers. Furthermore, the apparent viscosity increases for an increasing value of the modulus of the alkaline activator (Fig. 2.13).

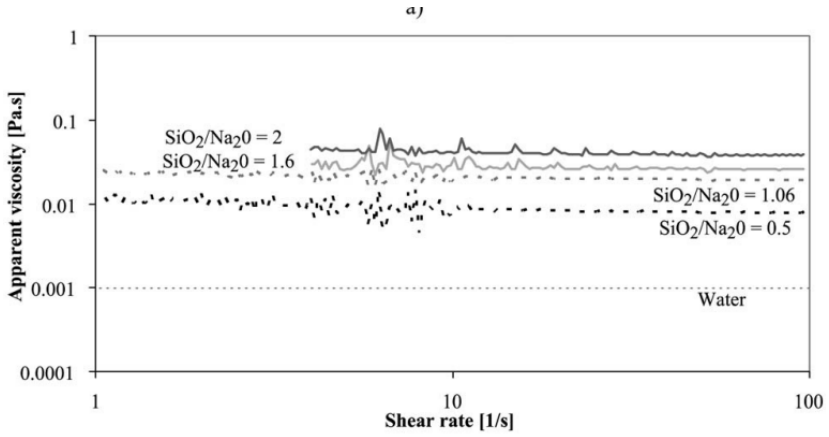

Figure 2.13: Viscosity as a function of shear rate at 20°C for different SiO_2/ Na_2O silicate solutions (H_2O/Na_2O = 16). *(Favier et al., 2014).*

Fresh properties - concluding remarks
The following can be concluded from the literature review:

- An increasing MK content contributes to an increase in setting time and flow, i.e. better workability. The reduction in slag content contributes to better flow of the mixture as a result of a reduction in angular particles in the mixture. Moreover, MK has a lower calcium content and higher silica and alumina content than slag. In the case of a high MK content, the calcium content in the mixture is much lower, resulting in a decelerated setting. Thus, MK, as part of a binary blended binder, actively decelerates the setting time of AAMs under ambient curing conditions.
- The plastic viscosity of AAMs is found to increase as well with increasing content of MK, due to an increase in specific surface area. This is especially interesting for 3DCP. An increase of the modulus contributes to an increase in flow time, hence a lower flowability. The silica content in the alkali solution increases for increasing moduli, resulting in a rise in solution viscosity.
- A low modulus of the alkaline solution indicates a high Na_2O content relative to the SiO_2 content, resulting in chemical reactions that occur at a faster rate. In multiple studies, an optimum modulus is observed for the fresh properties. Exceeding a certain limit of the sodium silicate to sodium hydroxide ratio results in a more cohesive mix with lower slump.
- An increase in Na_2O content (higher molarity of NaOH solution) contributes to an increase in the Na^+-content, a fast rate of chemical reaction and therefore a reduction of the molar ratio SiO_2:Na_2O. More heat is released for higher Na_2O content, resulting in a lower flow rate and accelerated setting time.
- An improved workability, i.e. higher slump, is achieved for mixes with higher alkaline solids to binder ratios. The setting time is also increased considerably for increasing alkali solids to binder ratios.

In Table 2.1, an overview of the reviewed literature on calcined clay based geopolymers is presented.

Table 2.1: Overview of the literature on fresh properties of metakaolin based AAMs. N.R. = not reported. N.A. = not applicable.

CC (%)	BFS (%)	FA (%)	M_s	SS/SH solids ratio	Na_2O/ binder	Molarity NaOH	w/b	Fresh properties
100%	0%	0%	0.74-1.16	1.30-3.00	0.06-0.11	14 M	0.38-0.54	Mixes with low NS/NH solids ratio (1.3, 1.6) show almost no slump. Increasing the NS/NH ratio to 2 and 2.5 produced more workable mixes (slump=30 mm). Exceeding a certain limit of the NS/NH ratio resulted in a more cohesive mix with lower slump values of 20 mm. (Al-bidah et al., 2020).
0-15%	85-100%	0%	1.08–1.26	3.0	0.07-0.135	10, 14, 16, 18 M	0.20-0.37	The study showed that the setting time and the flow increased, while the density decreased with increasing MK content. Another observation was that the flow was reduced from 23 to 15 cm when the molarity of the sodium hydroxide solution was increased from 10 to 18 M, as this resulted in a higher Na_2O content. The flow ability increased with an increasing alkali solids to binder ratio (S:B). The setting time was also improved considerably for increasing S:B ratios. (Huseien et al, 2018).
25-75%	25-75%	0%	1.00-2.00	2.2-85.6	0.06-0.14	N.R.	0.50	A study by Hasnaoui et al. (2019) reports optimum fresh properties (workability and setting time) for mixtures with a GBFS + MK/Activator ratio of 3.0. Higher metakaolin content results in a higher flow and setting time and therefore less good fresh properties in comparison with Portland cement mortars. An increase in molar ratio SiO_2/Na_2O leads to an increase in flow time (lower workability) for all mixtures. No clear correlation is found for the molar ratio and the setting time of the mixtures.

70-100%	0-30%	0%	0.80-1.80	2.8-10.6	0.10-0.19	N.R.	0.17-0.19	In a study by Alanazi et al. (2017), the effect of modifying the modulus of the alkaline solution and the effect of slag content on metakaolin based geopolymer is investigated by focussing on the early strength and durability of the geopolymer pastes. The study showed that the maximum compressive strength for a metakaolin based (100%) geopolymer mortar was obtained for a modulus of 1.0. This study also showed that partially replacing the metakaolin with slag (30%) resulted in a mixture with a higher workability but not necessarily higher compressive strength.
100%	0%	0%	0.50-2.00	N.R.	N.R.	N.R.	N.R.	The flow properties of metakaolin based geopolymers are described and compared to Ordinary Portland Cement. The viscosity of metakaolin-based geopolymers is mainly determined by the properties of the alkaline solution. Furthermore, the apparent viscosity increases for an increasing value of the modulus of the alkaline activator. (Favier et al. 2014).

Mechanical properties of AAMs containing MK

According to *Padmakar et al. (2017)*, a maximum 7-, 14- and 28-day strength is obtained for geopolymer concrete containing only metakaolin (100%) as pozzolanic material in the binder. In this study, the compressive strength, tensile splitting strength and flexural strength are determined for various proportions of metakaolin and ground granulated blast furnace slag in geopolymer concrete. The composition of the alkaline solution, containing sodium silicate and sodium hydroxide, is kept constant to eliminate the influence of this variable on the results. The improved strength development of the geopolymers with high metakaolin content indicates an enhanced geopolymerization due to the availability of soluble silicate species and therefore an improved dissolution of silica and alumina in metakaolin.

In the study of *Albidah et al. (2020)*, the influence of the sodium silicate to sodium hydroxide mass ratio is investigated for metakaolin based geopolymer concrete. The highest 28 day-compressive strength is achieved for mixes with sodium silicate to sodium hydroxide mass ratios within the range of 1.3-2. The high amount of reactive silica contributes to a higher density of Si-O-Si bonds. Further increasing the ratio to 2.5-3.0 results in a strength drop of approximately 10-20 MPa. This observation is assigned to the excess silica content, which impedes the geopolymerization process. This shows that there is optimum dosage of the alkali activator, which also applies to the fresh properties of geopolymer concrete for this specifically selected combination of parameters. These findings are in line with the study of *Morsy et al. (2014)*. In the study of *Morsy et al.*, the changing parameter is the sodium silicate to sodium hydroxide solids ratio (0.50-2.50) for a fly ash based polymer mortar. *Morsy et al.* observes a maximum compressive strength for a ratio of 1.0. As the ratio increases, the strength decreases. An increase of this ratio results in an increase of the sodium and silica concentration. Excessive sodium silicate hinders structure formation and therefore led to lower strength of the geopolymer. Furthermore, *Albidah et al.* shows a positive trend of the 28-day compressive strength of geopolymer concrete when the alkaline solids to MK ratio is increased from 0.21 to 0.37 (decreasing MK content). For higher ratios than 0.37, a strength drop is observed, which is attributed to the excessive silica content which contributes to the impedance of the geopolymerization.

The study conducted by *Huseien et al. (2018)* shows the effect of metakaolin as substitution (0-15%) for ground granulated blast furnace slag (BFS) on the early strength of geopolymer mortars (Fig. 2.14). Geopolymer mortars containing MK show lower early strength than the reference mixtures containing only blast furnace slag. However, the 28-day compressive strength of mixtures containing MK (5-15%) is higher compared to the reference mixes. This indicates a delayed geopolymerization process of mixtures containing MK. The higher 28-day strength is a result of the higher Al_2O_3 and SiO_2 content in metakaolin in comparison to blast furnace slag, which improves geopolymerization due to the enhanced production of NASH- and CASH-gel.

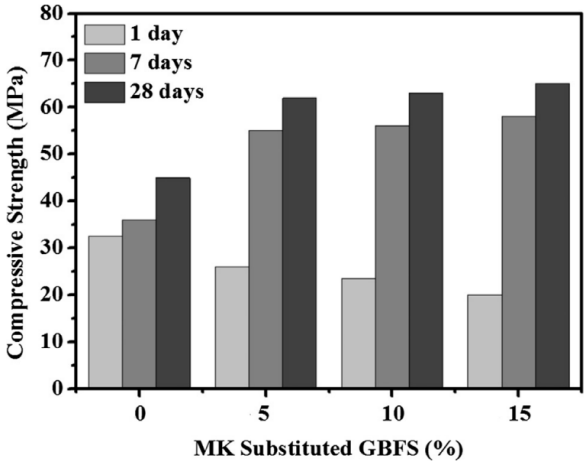

Figure 2.14: Impact MK substituted GBFS on the early compressive strength of GPMs. *(Huseien et al., 2018).*

The composition of the alkaline solution is also considered as a parameter in the study of *Huseien et al* (Fig. 2.15). Sodium hydroxide solutions with various molar concentrations (10-18 M) are prepared and combined with a sodium silicate solution to obtain an alkaline solution with various SiO_2:Na_2O mass ratios. The sodium silicate to sodium hydroxide solids ratio is fixed. An increase in molarity of the sodium hydroxide solution consequently will result in an increased Na_2O content and thus a reduction of the SiO_2:Na_2O mass ratio. The compressive strength increases with increasing SiO_2:Na_2O mass ratios, as an increase of this ratio enhances the degree of dissolution of silica and alumina and accelerates the hydrolysis, while impeding the polycondensation. The highest 1-day strength is observed for a molarity of 14 M (SiO_2:Na_2O mass ratio of 1.16). This is considered to be the optimum concentration for the NaOH solution. For higher molarities, the dissolution of calcium is inhibited, resulting in less hydration products and a lower rate of hydration. It was also reported that an excess in hydroxide ions (OH^-) caused the aluminosilicate gel to precipitate at an early age, resulting in lower strength. Last but not least, the influence of alkali solids to binder ratio on strength is reported. A high early age and 28-day strength for a low Na_2O:binder ratio (8%) is reported. An excess in water, i.e. higher water to binder ratios, reduces the geopolymerization rate (the amount of CASH- and NASH-gel) and therefore results in poor microstructure and lower strength.

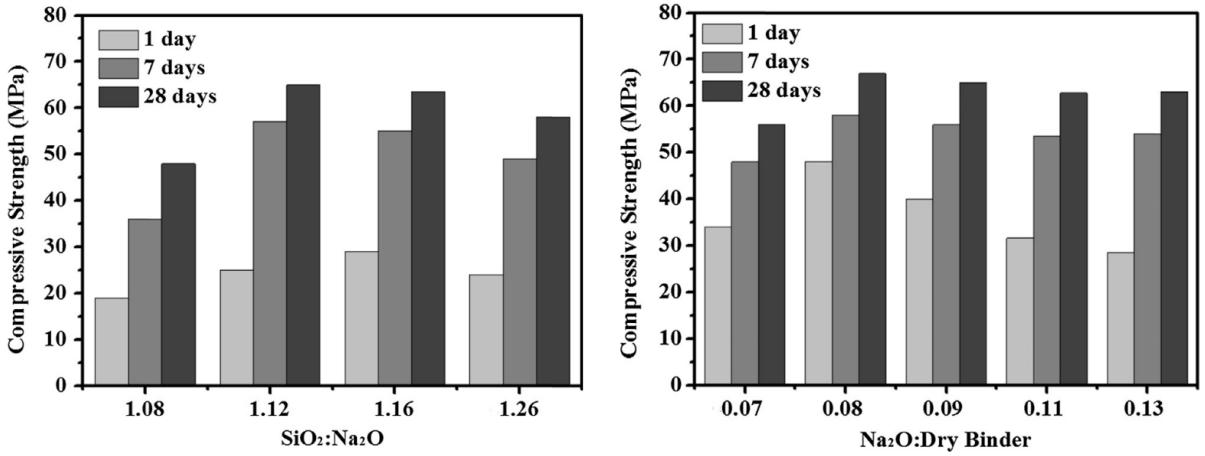

Figure 2.15: Impact of SiO_2:Na_2O ratio and Na_2O:dry binder ratio on the early compressive strength of GPMs. *(Huseien et al., 2018).*

Alanazi et al. (2017) shows that the best mechanical performance is achieved for a modulus of 1.0, for a metakaolin based geopolymer mortar. In this study, the influence of the modulus is studied by varying the modulus in the range of 0.8-1.8. Optimum early strength for a metakaolin based mortar is achieved for a modulus of 1.0, independent of the number of curing days (Fig. 2.16). Silica and alumina dissolve at a high rate for this molar ratio, hence accelerating the geopolymerization process. Exceeding this modulus will result in impedance of the geopolymerization process. *Skvára et al. (2006)* states that the presence of sodium ions plays an important role in the geopolymerization process, as sodium ions have a charge balancing function. An excess in sodium ions prevents the precipitation phase from contacting the precursor and alkaline activator and therefore hinders the structural formation, leading to lower strength. *Alanazi et al.* shows that high SiO_2/Na_2O ratios do not necessarily lead to better strength properties. In the study of *Alanazi et al.*, metakaolin is partially replaced by slag (30%) to observe the strength and fresh properties. The results show that a mix of slag blended with metakaolin is found to have less compressive strength than metakaolin alone.

In the study of *Srinivas et al. (2020)*, the focus is on determining the influence of various concentrations of the sodium hydroxide solution on the strength of metakaolin (30%) and fly ash (70%) based geopolymer concrete. The alkaline solution is comprised of a sodium silicate solution and a sodium hydroxide solution with different concentrations of 8 M, 11 M and 15 M. No optimum is observed for various concentrations of the sodium hydroxide solution. Strength increases for an increasing concentration of the sodium hydroxide solution and maximum strength is obtained for a concentration of 15 M, for oven curing as well as for ambient curing conditions. This positive trend is in line with the findings of *Huseien et al. (2018)*. Maximum

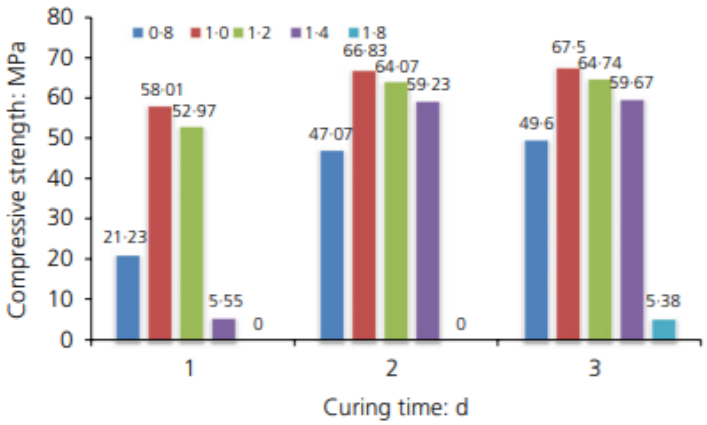

Figure 2.16: Average compressive strength of geopolymer mortar with different ratios of silicon dioxide/sodium oxide (0.8, 1.0, 1.2, 1.4 and 1.8) at curing ages of 1, 2 and 3 days. *(Alanazi et al., 2017).*

strength is obtained for oven curing, as this activates the geopolymerization process at an early age, contributing to high early age strength.

Hasnaoui et al. (2019) aims to find the optimum formulation for metakaolin and slag based geopolymer mortar for varying metakaolin and slag content and different compositions of the alkali solution. In this study, the effect of GBFS/MK ratio (25/75, 50/50 and 75/25) and the modulus of the alkaline solution (1.0, 1.2, 1.4, 1.6, 1.8 and 2.0) are inspected. Geopolymer mortars with low metakaolin and high slag content show the lowest 28-day compressive strength (Fig. 2.17), which is in accordance with the study by *Huseien et al. (2018)*. This is a result of the high calcium oxide content in slag, which contributes to higher early strength but lower 28-day strength. A higher metakaolin content contributes to a significantly improved 28-day compressive strength. MK provides a source of amorphous Al_2O_3 and SiO_2, which enhances the geopolymerization process and improves the mechanical properties. However, an excess in MK can negatively influence the strength properties. Therefore, the impact of MK on the strength properties was less significant for high incorporation ratios (Fig. 2.17). Furthermore, the study shows improvement in mechanical properties for higher molar ratios of SiO_2/Na_2O. An increase of this molar ratio results in an increase of the Si/Al ratio, which contributes positively to the formation of Si-O-Si bonds. These bonds are stronger than those of Si-O-Al and Al-O-Al and thus, an increase of the overall strength properties is reported.

Davidovits (2013) reports that a good geopolymer binder consists of 55 to 70% by weight of raw materials (MK + GBFS) and 25 to 35% of alkaline solution. Furthermore, *Davidovits* recommends a molar ratio SiO_2/Na_2O of the alkaline solution in the range of 1.45-1.95 for user-friendly conditions.

According to *Burciaga-Díaz et al. (2010)*, for higher replacement ratios of blast furnace slag by metakaolin, a higher amount of Na_2O is needed to obtain the highest maximum strength. A higher amount of Na_2O coincides with a lower modulus (SiO_2/Na_2O molar ratio) of the alkaline solution. It can therefore be concluded that for higher replacement ratios of slag, an alkaline solution with a lower modulus is needed. These findings are in contradiction with the study of *Hasnaoui et al. (2019)*. Hasnaoui et al. has found increasing strength (28-day compressive strength) for increasing moduli of the alkaline solution, for various replacement ratios of slag by metakaolin. The main difference between the two studies is the number of curing days. In the study of *Burciaga-Díaz et al.*, the mean strength after 1, 28, 90 and 360 days of curing is reported, while *Hasnaoui et al.* reports the compressive strength after 28 days of curing.

Burciaga-Díaz et al. also recommends a modulus in the range of 1–1.5 to promote adequate activation of binders containing BFS or MK and their binary mixes. A Na_2O/dry binder ratio of 10% is reported to be a good amount for adequate activation of a binary BFS and MK binder.

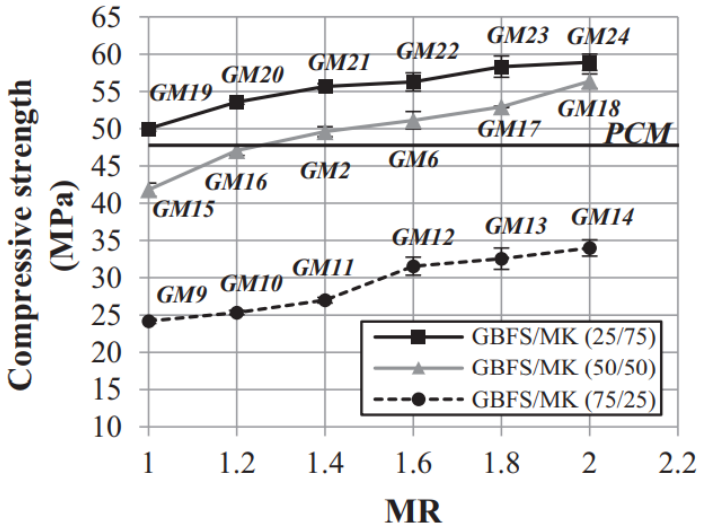

Figure 2.17: Compressive strength of GMs at 28 days as a function of molar ratio. *(Hasnaoui et al., 2019).*

Mechanical properties - concluding remarks
The following can be concluded from the literature review:

- Geopolymer mortars with high metakaolin content generally show lower early strength than reference mixtures containing only blast furnace slag. However, the 28-day compressive strength of mixtures with high metakaolin content is higher compared to the reference mixes. The low early strength is caused by a delayed geopolymerization process. Note that the geopolymerization rate is improved at later ages as a result of the higher Al_2O_3 and SiO_2 content in metakaolin in comparison to blast furnace slag, which improves geopolymerization due to the enhanced production of NASH- and CASH-gel.
- For higher replacement ratios of blast furnace slag by metakaolin, a higher amount of Na_2O is needed to obtain the highest maximum strength. A higher amount of Na_2O coincides with a lower modulus (SiO_2/Na_2O molar ratio) of the alkaline solution. It can therefore be concluded that for higher replacement ratios of slag, an alkaline solution with a lower modulus is needed.
- The compressive strength increases with increasing SiO_2:Na_2O mass ratios, as an increase of this ratio enhances the degree of dissolution of silica and alumina and accelerates the hydrolysis, while impeding the polycondensation. Furthermore, an optimum is observed for the strength of metakaolin based geopolymer concrete. Exceeding this optimum formulation for the binder, i.e. for higher moduli of the alkaline solution, results in an inhibited dissolution process of calcium. This leads to a reduced production of hydration products and therefore a lower rate of hydration. An excess in hydroxide ions (OH^-) causes the aluminosilicate gel to precipitate at an early age, resulting in lower strength
- An excess in water, i.e. higher water to binder ratios, reduces the geopolymerization rate (the amount of CASH- and NASH-gel) and therefore results in poor microstructure and lower strength.
- In the majority of the literature, pure metakaolin is used, despite the competing demand for this material. Insight in the behaviour of calcined clay in geopolymer concrete is needed. An option would be to use low- or high-grade calcined clay instead of pure metakaolin. Low- or high-grade calcined clay is considered to be a more cost-effective alternative, as less intensive purification is needed, while the supply is much larger.

In Table 2.2, an overview of the reviewed literature on calcined clay based geopolymers is presented.

Table 2.2: Overview literature on the mechanical properties of metakaolin based geopolymer concrete. N.R. = not reported. N.A. = not applicable.

CC (%)	GGBFS (%)	FA (%)	M_s SiO_2:Na_2O	SS/SH solids ratio	Na_2O/ binder	Molarity NaOH	w/b	Mechanical properties
100%	0%	0%	0.74-1.16	1.30-3.00	0.06-0.11	14 M	0.38-0.54	According to the study of Albidah et al. (2020) with only metakaolin as pozzolanic material, the highest 28 day-compressive strength was achieved for mixes containing NS/NH ratios of 1.3-2. However, increasing the ratio to 2.5-3.0 resulted in a strength drop of approximately 10-20 MPa. The study also showed a positive trend of increase in the 28-day compressive strength when the alkaline solids to MK ratio is increased from 0.21 to 0.37. For higher ratios, a strength drop is observed.
50-100%	0-50%	0%	N.R.	N.R.	N.R.	10 M	N.R.	The geopolymer concrete specimens are cast and tested for different types of strengths for 3, 7, and 28 days. Mechanical strength properties increased with increasing metakaolin content, irrespective of curing period. (Padmakar et al., 2017).
0-15%	85-100%	0%	1.08–1.26	3.0	0.07-0.135	10, 14, 16, 18 M	N.R.	The compressive strength of samples with MK showed lower early strength in all cases (5, 10, 15% replacement). However, the 28 day-strength was in all cases higher for the MK substituted samples than was the case for samples prepared without any MK. The compressive strength increased with increasing SiO_2:Na_2O ratios and is at an optimum for a molarity of 14M. A high early age and 28 day strength is reported for a low Na_2O:binder ratio (8%). (Huseien et al, 2018).
0%	0%	100%	N.R.	0.5-2.5	N.R.	10M	N.R.	In the study of Morsy et al. (2014), the changing parameter was the sodium silicate to sodium hydroxide solids ratio (0.50-2.50) for a fly ash based polymer mortar. They observed a maximum compressive strength for a ratio of 1.0. As the ratio increases, the strength decreases.

70%	0%	30%	1.12-1.37	2.5	0.09-0.11	8 M, 11 M, 15 M	0.39-0.41	Solutions with a concentration of 8M, 11M and 15M are used for metakaolin (30%) and fly ash based (70%) geopolymer concrete, with the goal of determining the mixture with maximum compressive strength. Strength increases for increasing concentration of the sodium hydroxide solution and maximum strength is obtained for a concentration of 15M. According to the observations, workability increases as well for increasing concentrations of the sodium hydroxide solution. Maximum strength is obtained for oven curing. (Srinivas et al., 2020).
25-75%	25-75%	0%	1.0-2.0	2.2-85.6	0.06-0.14	N.R.	0.50	A study by Hasnaoui et al. (2019) reports optimum mechanical properties for mixtures with a GBFS + MK/Activator ratio of 3.0. A significant decrease of strength is observed for increasing GBFS + MK/Activator ratios. For ratios smaller than 3.0, higher mechanical properties are obtained in comparison to Portland cement mortar. Increasing MK content and increasing MR result in better mechanical properties.
0-100%	0-100%	0%	0-2.0	N.R.	0.05-0.15	N.R.	N.R.	According to Burciaga-Díaz et al. (2010), for higher replacement ratios of blast furnace slag by metakaolin, a higher amount of Na_2O and therefore a lower modulus is needed to obtain the highest maximum strength. For higher replacement ratios of slag, an alkaline solution with a lower modulus is needed. Burciaga-Díaz et al. (2010) recommends a modulus in the range of 1–1.5 to promote an adequate activation of binders of BFS and MK and their binary mixes. 10% of Na_2O/dry binder was reported to be a good amount for adequate activation of a binary BFS and MK binder.

70-100%	0-30%	0%	0.80-1.80	2.8-10.6	0.10-0.19	N.R.	0.45-0.59	In a study by Alanazi et al. (2017), the effect of modifying the modulus of the alkaline solution and the effect of slag content on metakaolin based geopolymer is investigated by focussing on the early strength and durability of the geopolymer pastes. The study showed that the maximum compressive strength for a metakaolin based (100%) geopolymer mortar was obtained for a modulus of 1.0. This study also showed that partially replacing the metakaolin with slag (30%) resulted in a mixture with a higher workability but not necessarily higher compressive strength.

2.2. Additive manufacturing

Additive manufacturing of cementitious materials is currently gaining ground in the construction industry. As a result, different manufacturing methods are being developed and improved continuously. In the traditional manufacturing process of (in situ) concrete, the use of formwork is indispensable. The assembly of formwork is a relatively labour intensive process and very difficult for complex, geometrical shapes. 3D-printing of concrete removes the need for formwork and enables the industry to create complex shapes as well as optimization of material use. It also provides an opportunity for an automated building process with a minimal amount of labour and material wastage.

According to *Kothman et al. (2019)* and *Bos et al. (2016)*, 3D-printing of concrete offers the following advantages in comparison to the traditional construction method of concrete:

- The ability to optimize the material distribution according to the need of application;
- Freeform structure printing capability;
- Printing on demand;
- The reduction of material waste.

However, there are still some obstacles standing in the way of large-scale application of 3DCP. This will be discussed at the end of the chapter.

2.2.1. Printing techniques

3D-printing techniques that are used in the industry can be classified into two main groups:

- Extrusion-based 3D-printing;
- Powder-based 3D-printing.

For extrusion based printing, cement paste is extruded through a nozzle to print a structure layer by layer. For powder-based 3D-printing, construction elements are created by spraying binder liquids onto the deposited powder layers. It is a layer-by-layer process, similar to extrusion-based 3D-printing. The extrusion printing technique can be used for on-site construction applications, e.g. large scale building components with complex geometries. The powder printing technique can only be used off-site for small-scale precast building components. An advantage of using a powder printing technique is the ability to produce components with fine details and intricate shapes. For this research, the focus will only be on extrusion-based 3D-printing, as the goal is to facilitate the manufacturing of large-scale building components for the industry.

In Fig. 2.18, a schematic representation of a typical extrusion-based 3D-printing process is given. The process consists of a mixing stage, a pumping stage, a stage in which the material is transported from the pump to the end of the hose pipe and a extrusion stage.

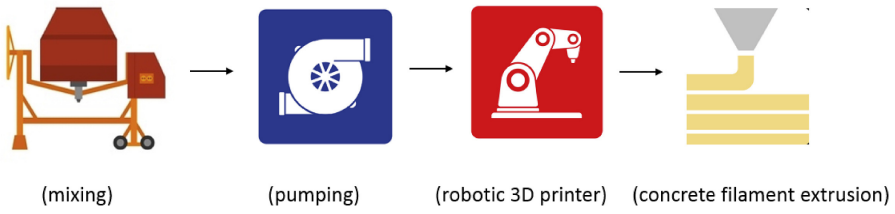

Figure 2.18: A schematic representation of a typical concrete printing process (extrusion-based 3DCP). *(Panda et al., 2018)*

2.2.2. Interlayer bond of 3D-printed concrete

During the past 10 years, 3D concrete printing (3DCP), as an additive manufacturing method of concrete, has been under development by more than 30 research groups worldwide. Eliminating formworks in 3DCP brings many advantages, e.g., reducing costs, labour works, and wastes. However, many challenges and difficulties for cement-based materials have arisen. The bonding strength between subsequent layers is believed to be one of the main weaknesses in printed structures. The layer interfaces are weakly connected

and generally show higher porosity. This weak interlayer adhesion is caused by a lack of intermixing between layers. Many printing parameters may influence the interlayer bonding strength. The presence of interfaces between concrete layers is a well-known phenomenon in the industry of concrete manufacturing. It seems to occur in in-situ cast projects, combinations of in-situ cast elements and precast elements and concrete repair. In other words, interfaces are generally observed between a hardened (old) and a fresh (new) concrete layer (Fig. 2.19). Besides traditional concrete manufacturing, the presence of interfaces is also observed in 3DCP. The bond between printed layers is considered to be the weakest link of 3D-printed concrete elements.

In theory, different types of bond formation are described. Bond formation can either be classified as mechanical or chemical. In the case of chemical bonding of cementitious materials, hydration and bonding of the cement particles across the interface are important factors. Mechanical bonding relies only on the physical attributes of the layers, e.g. interlocking of subsequent layers *(Zareiyan & Khoshnevis, 2017)*. In addition to chemical and mechanical bonding, *Sadowski (2019)* also mentions physical bonding, which is the formation of hydrogen bridges and van der Waal forces between layers. Chemical and physical bonding are generally considered to be weak in comparison to the mechanical bonding and therefore contribute very little to the overall interlayer bond strength. To improve the interlayer bond strength, the focus will be on mechanical interlocking. Due to lack of mechanical interlocking, the void content is higher at the interfaces of printed elements. The printed layer is unable to anchor into the pore structure of the underlying layer, resulting in reduced contact area between the layers, higher void content and therefore lower interlayer bond strength.

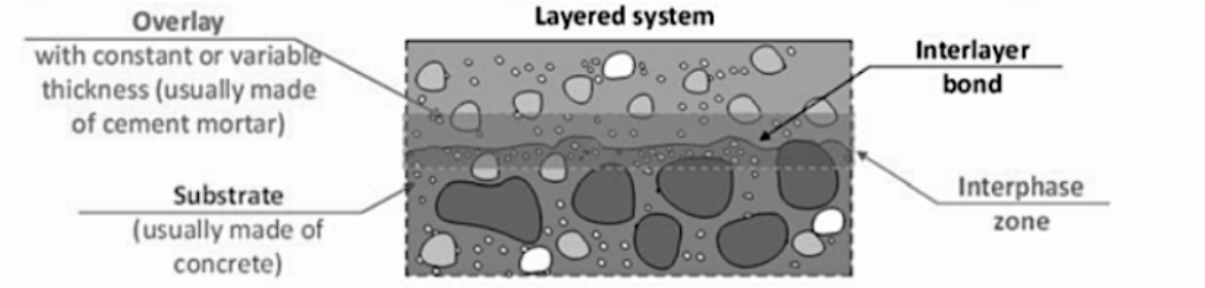

Figure 2.19: System of a layered composite (Sadowski, 2019).

Various printing parameters can influence the quality of printed concrete, such as:

- Printing speed
- Nozzle stand-off distance
- Nozzle type
- Surface moisture conditions
- Interval time between layers
- Layer orientation

Not only material properties, but also parameters like printer settings and configurations affect the quality of printed concrete considerably. Several methods have been proposed in literature to improve this interlayer bonding. This is however not within the scope of this research.

2.2.3. Extrusion based 3D-printing - an overview

3D-printing of AAMs

*Zainab Aldin (2019)*is among the first to explore 3D-printing of alkali-activated materials. The goal of her research is to propose a methodology for printable geopolymer concrete mixtures containing fly ash and blast furnace slag, while focusing on optimal ratios for the binder (FA:BFS) and for the alkaline solution ($NaOH$:Na_2SiO_3). The author first focuses on finding the optimal binder ratio and then continues with a selected mixture to find the optimum ratio for the alkaline solution.

In the first phase of the study, *Aldin* found increasing mechanical strength (3, 7 and 14 days) for mixtures with increasing slag content as a result of the higher reactivity of blast furnace slag. Fly ash to

blast furnace slag ratios between 100:0 and 50:50 are investigated in the research, while the ratio of the alkaline solution is kept constant ($NaOH:Na_2SiO_3$=50/50). The study shows an accelerated setting time and lower extrudability for increasing slag content. Higher content of fly ash generally allows for better flow and extrudability due to the presence of spherical particles. Although mixtures with high slag content show superior mechanical properties, *Aldin* continues with optimization of mixtures with low slag content (20%) to ensure high printability of the mixtures. In the second stage of the study, the fly ash to blast furnace slag ratio is kept constant (80:20), while the focus is shifted to studying the influence of Na_2SiO_3/NaOH mass ratios (0, 0.25, 0.43, 1, 2.33 and 4) on mechanical and setting time. The moduli of the alkaline solutions, e.g. the SiO_2/Na_2O molar ratios often denoted as M_s, are respectively 0, 0.82, 1.1, 1.51, 1.78 and 1.91 for Na_2SiO_3/NaOH mass ratios of 0, 0.25, 0.43, 1, 2.33 and 4. From the results can be concluded that there is an optimum value for the modulus as regards the mechanical strength. Maximum strength is obtained for a modulus of 1.51. The setting time is accelerated significantly for this value of the modulus. For this reason, the author decides to go for a modulus of 0.82 (Na_2SiO_3/NaOH=0.25) to ensure adequate strength while reaching the desired target value for the setting time of approximately 90 minutes. Note that the molarity of the sodium hydroxide is kept constant at 4M. After finding the optimal mixture with respect to mechanical strength and setting time, *Aldin* continues the research by finetuning the selected mixture with the addition of Acti-gel. Rheological properties such as the plastic viscosity and shear stress apparently increase for increasing content of Acti-gel (0-1.5%).

In the research of *Panda et al. (2019)*, a similar study is conducted to investigate the influence of fly ash and slag content on mechanical properties and fresh properties such as yield stress, viscosity and thixotropy for concrete printing applications. The solid activator consists out of potassium silicate together with potassium hydroxide to reach a modulus (M_s) of 1.5. In this study, the same trend with respect to mechanical and rheological properties is observed for various blast furnace slag contents. Partial replacement of fly ash by blast furnace slag (15-40%) positively affects the yield stress, thixotropy and compressive strength for a constant activator content of 15%. This effect is mainly attributable to the angular morphology of the slag particles. In the case of low replacement levels of fly ash by slag (up to 10%), rheological properties are not significantly influenced, unlike the early age strength properties.

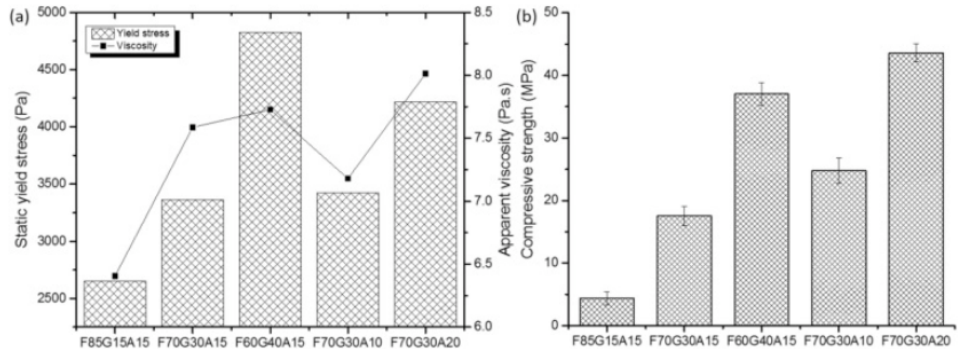

Figure 2.20: (a) Static yield stress and viscosity and (b) compressive strength of the various mixtures. F = fly ash content, G = slag content, A = activator content. *(Panda et al., 2019).*

The activator dosage is investigated as well in the study of *Panda et al. (2019)*. Increasing the activator content from 10 to 20% for a mix with 70% fly ash and 30% slag contributes to a higher yield stress and compressive strength. No such trend is found for the apparent viscosity.

In the study of *Kashania & Ngo (2018)*, the focus is on mixture optimization for 3D-printing of geopolymer concrete. Key factors in finding an optimum mixture design are the fresh properties such as rheology and open time, as well as mechanical strength. After finding an optimum mixture design, *Kashania & Ngo* continue with process optimization, e.g. exploring different pumping pressures and printing speed to ensure successful 3D-printing. Water to binder ratios of 0.31, 0.33 and 0.35 are explored, together with alkali activator to precursor ratios of 8 and 10% (Na_2O/precursor ratios of respectively 3.68 and 4.60).

The study shows that for increasing water to binder ratios, the yield stress is reduced (Fig. 2.21). This observation is a result of excess water that is not used for filling the voids, hence covering the surfaces of

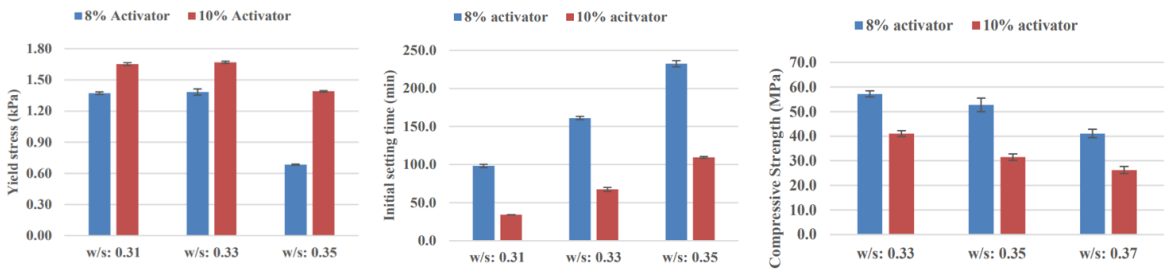

Figure 2.21: (a) Initial yield stress; (b) initial setting time; (c) compressive strength at 21 days. *(Kashania & Ngo, 2018).*

particles and leading to separation of the particles. Because of this separation of the particles in AAMs, the yield stress is reduced for increasing water to binder ratios. At the same time, the authors observe an increase in yield stress for increasing alkali activator to precursor ratios. An increase in activator dosage contributes to faster reaction and therefore a faster increase in yield stress. The yield stress is an important factor to ensure buildability and shape stability of the 3D-printed material after extrusion. The goal is to find a mixture with a fast increase in yield stress after extrusion, so that deformation of the underlaying printed layers is limited. Furthermore, the setting time is accelerated for higher wt. % of the activator as a result of fast reaction and high rate of dissolution of particles. Meanwhile, higher water to binder ratios lead to a deceleration in setting time as a result of a lower pH and therefore a lower rate of dissolution and reaction (Fig. 2.21). The setting time indicates the rate in which the material is increasing in strength. A short setting time ultimately means that the material is rapidly gaining strength and buildability, but adhesion between layers (interlayer bond strength), workability and pumpability may decrease. Also, the 21-day compressive strength increases for decreasing water to binder ratios, while the strength decreases for increasing activator dosage (Fig. 2.21). *Panda et al. (2019)* reports improved mechanical strength for increasing activator dosage. One would typically expect the strength to be larger for increasing reaction rate and higher yield stress evolution over time, which is the case for a higher activator dosage. However, lower alkalinity of the binder for a lower activator dosage drives formation of a geopolymer gel that increases the mechanical performance.

In the end, the authors show successful 3D-printing for a mixture with an activator dosage of 8% (Na_2O/precursor ratio of 3.68%) and a w/b ratio of 0.33. This mixture has an initial yield stress of 1.38 kPa and an initial setting time of roughly 160 minutes.

3D-printing of OPC-based materials

Panda & Tan (2018) have presented an optimization approach, in which a high-volume slag mortar is formulated for 3D-concrete printing. In this mortar, slag, Portland cement and hydrated lime are incorporated. The study shows a higher water demand for hydrated lime than Portland cement. For increasing lime content, the flowability therefore decreases. The study also shows an increase in yield stress and early mechanical strength for replacement of slag with Portland cement, which is attributed to the strong colloidal interaction (flocculation) of Portland cement. Ensuring a high yield stress is key in ensuring successful 3D-concrete printing. This increase in yield stress is also observed for decreasing water to binder ratios. Another important parameter in ensuring successful 3D-printing is thixotropic behaviour of the cementitious material. Thixotropic behaviour is characterized by two phases: (a) structural break down and (b) recovery. It describes how fast a material can break down (during pumping) and recover (after extrusion). The structural breakdown is crucial in ensuring pumping without any discontinuity, while the recovery is important to ensure high yield stress and good buildability after printing.

To measure structural breakdown, constant shearing is applied and the shear stress of the material is monitored. To measure structural recovery, three different shear rates are applied, i.e. (i) 0.01 s^{-1} for 60 seconds (ii) 300 s^{-1} for 30 seconds and last (iii) 0.01 s^{-1} for 60 seconds (Fig. 2.22). The change in apparent viscosity is measured during these three different phases. The phases are chosen to capture the apparent viscosity at (i) rest, (ii) during extrusion and (iii) after extrusion, again at rest. The mixture with the highest PC-content (20%), 10% limestone, 70% slag and a water to binder ratio of 0.45 shows the best thixotropic behaviour (Fig. 2.22). Shear thinning behaviour is observed for this mixture, i.e. the structure is

gradually broken down at a constant shear rate. During 3D-printing, this particular material will lose its interparticle bonding and will flow without discontinuity as a result of the (constant) shearing action of the pump.

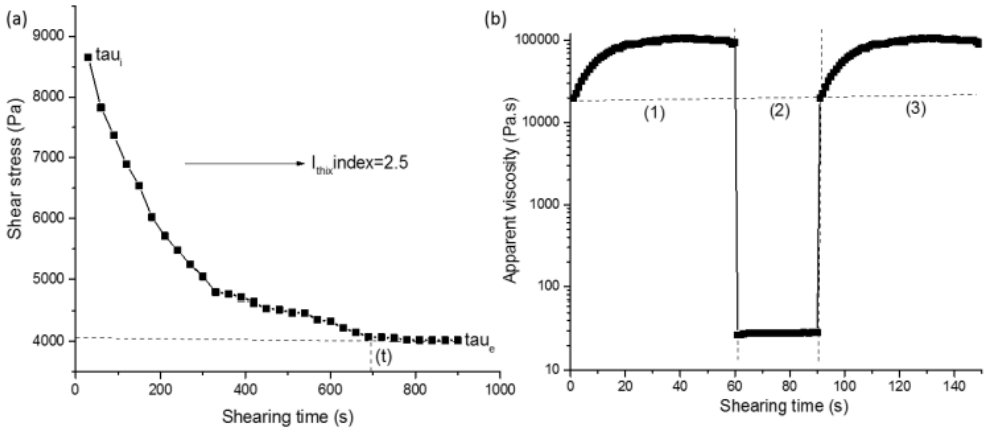

Figure 2.22: (a) Shear thinning, (b) thixotropy recovery behaviour of mortar mixture with 20% PC, 10% LP, 70% BFS. *(Panda & Tan, 2018).*

In the study of *Chen et al. (2020)*, the influence of different grades of calcined clay on properties such as printability, compressive strength (7d) and hydration for 3DCP is investigated. Different compositions of the cementitious material are investigated, which contains varying amounts of limestone (LP), calcined clay (CC) and Portland cement (PC). Different grades of calcined clay (LCC, MCC, HCC) are obtained by blending low-grade (LGCC) and high-grade calcined clay (HGCC) in three different proportions. The reactive contents of LGCC and HGCC are respectively 48.8% and 75.1%. In Fig. 2.23, an overview of the mixture designs is presented.

Mixture	Mix Proportion							
	Binder [wt.%]				Sand and Water mass ratios		Admixture mass ratio	
	PC	LGCC	HGCC	LP	Sand/Binder	Water/Binder	SP/Binder	VMA/Binder
REF[a]	40	0	0	60	1.5	0.3	0.02	0.0024
LCC	40	40	0	20	1.5	0.3	0.02	0.0024
MCC	40	30	10	20	1.5	0.3	0.02	0.0024
HCC	40	20	20	20	1.5	0.3	0.02	0.0024

Figure 2.23: Mixture designs of cementitious materials prepared in the study of *Chen et al. (2020).*

The study shows that increasing the high-grade calcined clay content from 0 wt.% to 50 wt.% generally results in an increase of the flow consistency, improvement of the buildability, a reduction of the printability window and an accelerated cement hydration. A downside of using increasing contents of HGCC is the increased air void content in the interlayers, contributing to a reduced compressive strength. Due to the higher structuration rate of mixture HCC, a cold-joint is formed between layers, therefore weakening the bond between layers. Optimal strength was achieved for mixture MCC, with the calcined clay consisting of 25% HGCC and 75% LGCC.

Chen et al. (2021) continues his study by investigating the influences of high Portland cement substitutions by low-grade calcined clay (reactive content of 48.8%) and limestone for 3DCP. Besides OPC, limestone and calcined clay and admixtures such as a superplasticizer (SP) and a viscosity modifying agent (VMA) are used. The dosages of these admixtures are kept constant in the study. The pumping rate is kept constant as well, at 58-60 rpm. Properties like the printability, the stiffness-evolution and the early-age hydration are assessed for various mixture designs. The results show that an increase of the limestone and calcined clay content actively reduces the slump, flowability, initial setting time and the initial material flow rate. Furthermore, the buildability and stiffness evolution are improved for increasing content of limestone and calcined clay. *Chen et al.* reports a dilution effect on hydration for increasing content of limestone and calcined clay, resulting in a reduction of the compressive strength for high cement replacement.

Moreover, the study shows that for an increase in the VMA content (0.12% increment), shape retention and water retention capacity are enhanced. An increase of the SP content (0.5% increment) results in an increase of the material flow rate, extrudability, operation windows and the initial setting time, while the buildability of the various mixtures is reduced.

Extrusion based 3DCP - concluding remarks

In the reviewed literature, a trend with respect to fresh and mechanical properties is observed for various slag/fly ash ratios for geopolymer concrete. An increasing slag content contributes to an improved mechanical strength as a result of the higher reactivity of slag. Setting is accelerated in this case, i.e. shorter setting time, and the workability and extrudability are reduced. Replacement of fly ash by slag positively affects rheological properties, such as yield stress and thixotropy. Based on the reviewed literature, it is expected that mixtures with higher slag content will show faster yield stress evolution, due to the higher reactivity of blast furnace slag compared to calcined clay. Higher slag content will therefore result in an acceleration of the hardening process. Also, a higher activator content (activator/precursor ratio) is associated with a shorter setting time and a higher yield stress. An increase of the modulus of the alkaline solution will contribute to an increased viscosity of the mixtures. The trendline of the mechanical properties for various activator dosages is not conclusive based on the reviewed literature, meaning that there is high interdependency between various parameters.

For Portland cement-based materials, a different behaviour is observed. PC-based materials show colloidal interaction between particles, often denoted as flocculation. As a result of this colloidal interaction, a high yield stress is observed. Besides the high yield stress, PC-based materials often show shear thinning behaviour: structural breakdown is achieved during shearing (pumping), while the materials recover quite fast after extrusion. For AAMs, this behaviour is not always observed. Incorporation of calcined clay in PC-based materials actively reduces the slump, flowability and initial material flow rate, while the buildability and stiffness evolution are improved for increasing content of calcined clay. The early age strength generally decreases for increasing calcined clay content in PC-based cementitious material.

To ensure successful 3D-printing of cementitious materials, the following material properties are highlighted in literature:

- Shear-thinning behaviour, i.e. the structure is gradually broken down at a constant shear rate. This property ensures continuity during pumping. During pumping, the apparent viscosity should be low.
- Fast recovery after extrusion. The material regains its strength rapidly after extrusion. This property is related to the apparent viscosity, which should be high at rest.
- High yield stress after extrusion. The yield stress is an important factor to ensure buildability and shape stability of the 3D-printed material after extrusion. A high yield stress ensures limited deformation of the underlaying printed layers.
- High early strength to maintain good buildability of the printed structure. This property is related to the yield stress. High yield stress coincides with high early strength.
- Long initial setting time to ensure continuity during printing. A short setting time ultimately means that the material is rapidly gaining strength and buildability, but adhesion between layers (interlayer bond strength), workability and pumpability may decrease.

In Table 2.3, a summary of the reviewed literature is presented.

Table 2.3: Overview literature on 3DCP of AAMs and PC-based materials. N.R. = not reported. N.A. = not applicable.

GP/PC	PC [%]	BFS [%]	FA [%]	CC [%]	LP [%]	w/b [-]	M_s [-]	Acti-vator dosage [%]	Na_2O/ precursor [%]	Comment
GP	0	0-50	50-100	0	0	0.35	0-1.91	N.R.	1.86-4.15	*Aldin (2018)* finds increasing strength for increasing slag content in the binder. As the slag content increases, the setting time is accelerated and the workability is reduced. The addition of Acti-gel positively influences the rheological properties of printed geopolymer concrete.
GP	0	15-40	60-85	0	0	N.R.	1.50	10-20	N.A.	*Panda et al. (2019)* find increasing strength, thixotropy and yield stress for increasing slag content. An increase in activator dosage results in higher compressive strength and yield stress. An optimum viscosity is reached for a dosage of 15%.
GP	0	66.7	22.2	0	0	0.31-0.35	N.R.	8-10	N.R.	The remaining part of the precursor consists out of silica fume (11.1%). Yield stress increases for increasing activator to precursor ratios and decreasing water to binder ratios. Setting time is decreased for increasing activator dosage and increased for higher w/b ratios. (*Kashania & Ngo, 2018).*
PC	10-20	70-85	0	0	5-10	0.45-0.50	N.A.	N.A.	N.A.	In the study of *Panda & Tan (2018)*, a high-volume slag mortar is formulated. The results show that a ternary blind of slag, Portland cement and lime exhibits a shear-thinning flow behaviour as well as high yield stress as a result of the colloidal interaction between particles.

PC	40	0	0	40	20	0.30	N.A.	N.A.	N.A.	In the study of *Chen et al. (2020)*, the influence of different grades of calcined clay on properties such as printability, compressive strength (7d) and hydration for 3DCP is investigated. The study shows that increasing the high-grade calcined clay content from 0 wt.% to 50 wt.% generally results in an increase of the flow consistency, improvement of the buildability, a reduction of the printability window and an accelerated cement hydration. A downside of using increasing contents of HGCC is the increased air void content in the interlayers, contributing to a reduced compressive strength.
PC	10-100	0	0	0-60	20-60	0.30	N.A.	N.A.	N.A.	The influences of high Portland cement substitutions by low-grade calcined clay and limestone is investigated for 3D concrete printing. The results show that an increase of the limestone and calcined clay content actively reduces the slump, flowability and initial material flow rate, while the buildability and stiffness evolution are improved for increasing content of limestone and calcined clay. Compressive strength decreases for increasing calcined clay content. *Chen et al. (2021).*

2.2.4. Challenges of 3DCP

Research trends are moving towards building applications with AAMs as a suitable concrete material for eco-friendly 3D-printed construction materials.

Even though concrete-based 3D-printing is gaining popularity, daily practice still seems far away as a result of several technological challenges. These challenges will be discussed below.

Challenge 1: Material properties

The main challenge in developing a printable mix is to ensure that the mix has fast early-age strength development for buildability and stiffness, while being flowable enough to fuse with other layers and to ensure good pumpability. These competing demands make it very difficult to develop a mixture for 3D-concrete printing. A material with high static yield stress and low viscosity is suitable for use in 3D-printing of concrete. Therefore, a conventional concrete mix design is not valid for 3D-printing.

Challenge 2: Weak interlayer bond

Another large problem related to 3DCP is the interlayer bond strength. Due to the anisotropic behaviour of the material, the material shows different strength in different directions. This anisotropic behaviour may be caused by the heterogeneity generated by the contact between layers, i.e. the interlayer bond. The interlayer bond between printed layers is often reported as the weakest link of 3DCP. The interlayer bond strength can be influenced by many parameters, e.g. printing speed, nozzle shape and offset height, interval time between layers, surface moisture conditions and material properties.

Challenge 3: Incorporation of reinforcement

Moreover, there are still huge limitations to incorporation of reinforcement in 3D-printed concrete. Incorporation of steel and composites in concrete is very common to carry the tensile stresses and to ensure some ductility of the material. In order for 3D-printed concrete to be considered an attractive and feasible alternative to traditional concrete, effective solutions for reinforcement should be explored. There are currently various reinforcing methods and technologies for 3DCP, e.g. post-installed reinforcement, fibre reinforcement, in-layer direction reinforcement and pre-installed reinforcement. These methods are generally not considered to be effective in continuously reinforcing the weakest link of printed concrete, i.e. the interlayer direction, and generally impede the design freedom of 3DCP.

Challenge 4: Sustainability

At the moment, most printable mortars consist of Portland cement. The production of OPC is very energy intensive and therefore a major generator of carbon dioxide, which is considered to be a potent greenhouse gas. High CO_2-emissions are caused by calcination of limestone and combustion of fossil fuel during an energy intensive production process. The production of concrete is responsible for 8% of the global CO_2-output *(Warburton, 2019)*. To effectively minimize CO_2-emissions during concrete manufacturing, use of AAMs is essential. However, there are additional challenges related to 3D-printing of AAMs, that will be discussed in the next paragraph.

Challenge 5: Mortar vs. concrete

As a result of limitations to the nozzle size and the need for a high printing resolution, coarse aggregates are typically not used for manufacturing of printable concrete. Aggregates with a maximum size of 2 mm are therefore commonly selected for 3DCP. A printable cementitious material can be considered as concrete when coarse aggregates (particle size larger than 4 mm) are incorporated. As this is not the case for most printable blends, these materials are considered to be mortars. Due to the absence of coarse aggregates, mortars are not as durable and strong as concrete. Furthermore, mortars show much more shrinkage than concrete. The presence of coarse aggregates therefore provides a higher resistance to shrinkage, improved strength and higher durability.

Challenge 6: Missing regulations

Last but not least, there are hardly any guidelines and research available about upscaling mixture designs for 3DCP from lab to industry. The structural engineers need to be involved in material production as well as on-site construction. To ensure that 3DCP will be used in larger construction projects, upscaling techniques need to be evaluated and new methodologies need to be proposed, so that the gap between demand and supply for cost-effective and sustainable 3D-printed structures can be closed.

2.2.5. Additional challenges of 3D-printing of AAMs

From an environmental point of view, it would be interesting to consider AAMs for 3D-printing applications, as industry by-products are used instead of OPC. Replacement of OPC by more sustainable materials will effectively reduce the environmental footprint of the material. However, using AAMs for 3D-printing applications may lead to even more challenges.

According to *Favier et al. (2014)*, AAMs do not show adequate material properties for extrusion based 3D-printing, i.e. a high static yield stress and low viscosity. *Favier et al.* mentions that unlike regular cement, AAMs does not show colloidal interaction. This colloidal interaction provides initial yield stress in the fresh stage of the material.

The performance of AAMs largely depends on the precursors and the type and concentration of the activators. A fly ash based AAM shows a very slow setting and low early-age strength for example, while a slag based AAM shows very fast setting, high early-age strength and carbonation *(Komljenović et al., 2013)*. Also, AAMs show in almost all cases much higher autogenous and drying shrinkage compared to OPC. To ensure that AAMs are a viable alternative to OPC, the early-age properties and the hardened properties must be well-controlled and within a similar range as OPC.

In short, it can be concluded that AAMs have additional variables that influence the material behaviour in fresh state. A successful application of AAMs in 3DCP requires a comprehensive understanding of its behaviour in fresh and hardened state.

3

Research framework

3.1. Research justification

Over the years, concrete structures have proven to be strong and resilient, as they have survived wars and natural disasters. Concrete as a construction material is abundant, locally available, relatively cheap and can be used for a variety of purposes. For this reason, concrete is the most used substance on the planet after water. The use of concrete has one major downside: its colossal carbon footprint. The production of OPC is very energy intensive and therefore a major generator of carbon dioxide, which is considered to be a potent greenhouse gas.

In an attempt to reduce the CO_2-emissions in the construction industry, additive manufacturing of cement based materials has emerged as a promising construction technology due to its many advantages. Additive manufacturing offers many opportunities to improve the sustainability of concrete as a building material. Compared to conventional construction processes, additive manufacturing offers a reduction in amount of labour, on-site construction time and material wastage, while offering more architectural freedom to create complex geometries. Additive manufacturing may therefore reduce the total amount of costs, while providing a more sustainable construction process. There is already much research available about 3D-printing of cement based materials. However, to satisfy the requirements for 3D-printed concrete, larger quantities of Portland cement are used in the printable mixtures compared to traditional concrete to ensure good mechanical performance. To further improve the sustainability of this construction method, Portland cement needs to be replaced by alternative materials with a lower environmental footprint. The focus therefore slowly shifts to 3D-printing of AAMs, in which local (low CO_2) materials are used to increase the level of sustainability in the construction industry.

As a result of the *Betonakkoord* in the Netherlands, the availability of fly ash and blast furnace slag will strongly decrease after 2030, due to effective usage in manufacturing of blending cements and concrete. Also, due to decreasing levels of coal-fuelled power generation and the move towards natural gas and renewable energy sources, availability of fly ash will decrease even more. For these reasons, it can be concluded that availability of industrial by-products such as fly ash and slag is quite uncertain for the Netherlands after the year 2030. From a long term point of view, it's therefore important to consider alternative materials for use in AAMs. Considering the worldwide abundance of calcined clay, as well as the low CO_2-footprint during production, calcined clay is highlighted in many studies as an alternative in manufacturing of AAMs. To ensure good performance of the calcined clay based AAM, it is recommended to use a hybrid alkaline binder, e.g. a combination of a low and high calcium alkaline binder for a more uniform development of the microstructure and therefore optimal properties. As calcined clay is a low calcium binder, it is therefore recommended to combine calcined clay with slag, a high calcium binder, for optimal material properties.

There are still a lot of challenges regarding 3D-printing of AAMs. Furthermore, there is limited research available on 3D-printing of AAMs and no research about 3D-concrete printing of calcined clay and slag based AAMs. Another observation is that hardly any focus is placed on shrinkage of 3D-printed concrete, although this has proven to be one of the main issues related to printing on industry scale.

This research will be devoted to the development of alkali-activated calcined clay and slag-based materials. The relationship between calcined clay content, fresh properties, rheology, mechanical properties, hydration and shrinkage is investigated, with a focus on 3D-printing applications.

3.2. Research aim and objectives

3.2.1. Research aim

The aim of this project is to propose a methodology for optimization of alkali-activated calcined clay and slag based materials (AACCSMs), specifically for the purpose of 3D-printing. In doing so, several parameters will be investigated for optimization of the mixture design to compile with the printing process, such as the water to binder ratio, the modulus of the alkaline solution, the calcined clay/slag ratio and the sodium oxide to precursor mass ratio.

This study also aims to describe the influence of incorporation of calcined clay on fresh properties, mechanical properties, hydration and shrinkage of alkali-activated calcined clay and slag based materials. The data can be used to further fundamentally understand the role of calcined clay in an alkali-activated material, to enhance the knowledge and control of AASCCMs for 3D-printing applications.

3.2.2. Research objectives

In order to reach the goal, the following objectives are considered:

1. To optimize the alkali-activated calcined clay and slag based material as per the requirements of 3D-printed concrete;
2. To study the effect of different replacement levels of calcined clay on fresh properties, mechanical properties, hydration properties and shrinkage behaviour of alkali-activated calcined clay and slag based material;
3. To assess the potential of using calcined clay and slag based AAMs for 3DCP.

3.2.3. Main research questions

Research Question 1

To what extent is calcined clay and slag based AAM interesting for use in 3DCP?

Research Question 2

What is the influence of calcined clay content on fresh properties, mechanical properties, hydration and shrinkage behaviour of calcined clay and slag based AAMs?

3.3. Framework

The framework for this research is divides into two main stages:

Stage 1
In the first stage, the focus will be on mixture optimization of calcined clay and slag based alkali-activated materials. In doing so, several parameters will be investigated for optimization of the mixture design to compile with the printing process, such as the water to binder ratio, the modulus of the alkaline solution, the calcined clay/slag ratio and the sodium oxide to precursor mass ratio. This will happen on mortar level. The most promising mixtures will be selected for further research based on a fast screening.

Stage 2
The research will continue with one selected mixture. The influence of different replacement levels of calcined clay on fresh properties, mechanical properties and hydration will be investigated in the second phase. The characterization of hydration will be performed based on isothermal calorimetry, thermogravimetric analysis (TGA), Brunauer-Emmett-Teller specific surface area (BET SSA) and mercury intrusion porosimetry (MIP).

In Fig. 3.1, a schematization of the framework is presented.

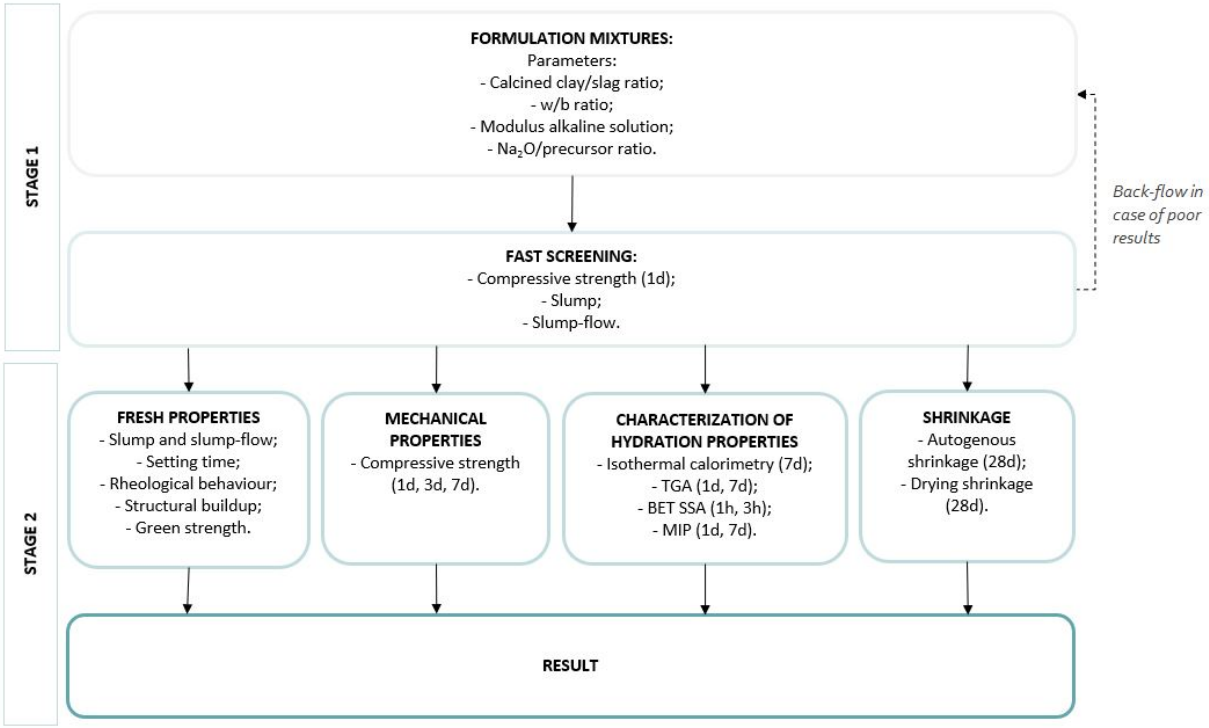

Figure 3.1: Schematization of the framework.

4

Research design

4.1. Design parameters

For the fast screening, 4 material parameters are selected as variables to find promising mixtures:

- Calcined clay to slag mass ratio of the precursor.
- Modulus of the alkaline solution (M_s): $\frac{SiO_2}{Na_2O}$ molar ratio of the activator.
- Water-to-binder ratio: ratio of total amount of water to the sum of solid precursor and solid activator.
- Sodium oxide-to-precursor ratio: (Na_2O) percentage by mass of precursor, denoted as Na_2O%.

The material parameters for the fast screening are illustrated in Fig. 4.1.

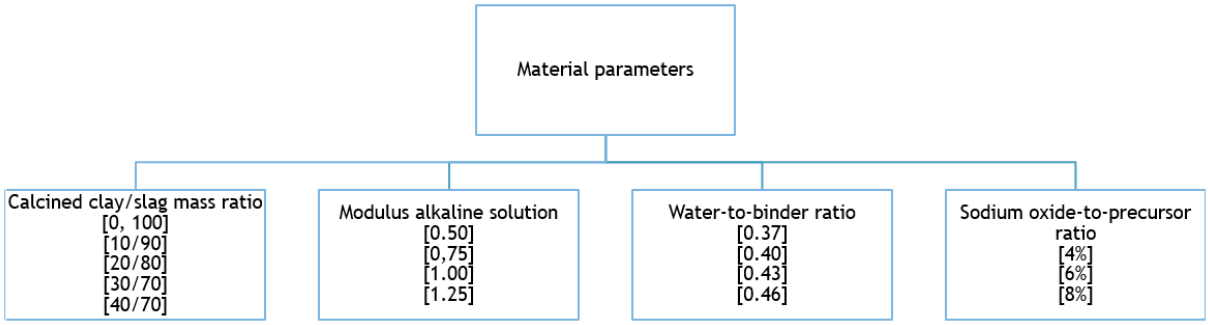

Figure 4.1: Material parameters

4.2. Materials and preparation methods

4.2.1. Calcined clay (CC)

The high-grade calcined clay is provided by Argeco in France. The chemical composition is presented in Table 4.1.

Table 4.1: Chemical composition of high-grade calcined clay. Manufacturer: Argeco.

Chemical composition [%]											
	SiO_2	**Al_2O_3**	**CaO**	**Fe_2O_3**	**K_2O**	**TiO_2**	**MgO**	**$SO_3{}^{2-}$**	**Cl^-**	**S^{2-}**	**Na_2O**
CC	62.4	30.5	1.8	1.4	0.1	1.5	0.5	0.3	$<$0.01	0.5	0.05

Table 4.2: Characteristics of calcined clay.

	BET-SSA [m^2/g]	Average pore width by BET [nm]	Total pore volume [cm^3/g]	Bulk density [kg/m^3]	Amorphous content [%]
CC	12.02	1.24	0.003722	2580	70

In Fig. 4.2, the measured XRD pattern is displayed in black after background subtraction and small displacement correction. The coloured sticks give the peak positions and intensities of the possibly present crystalline phases.

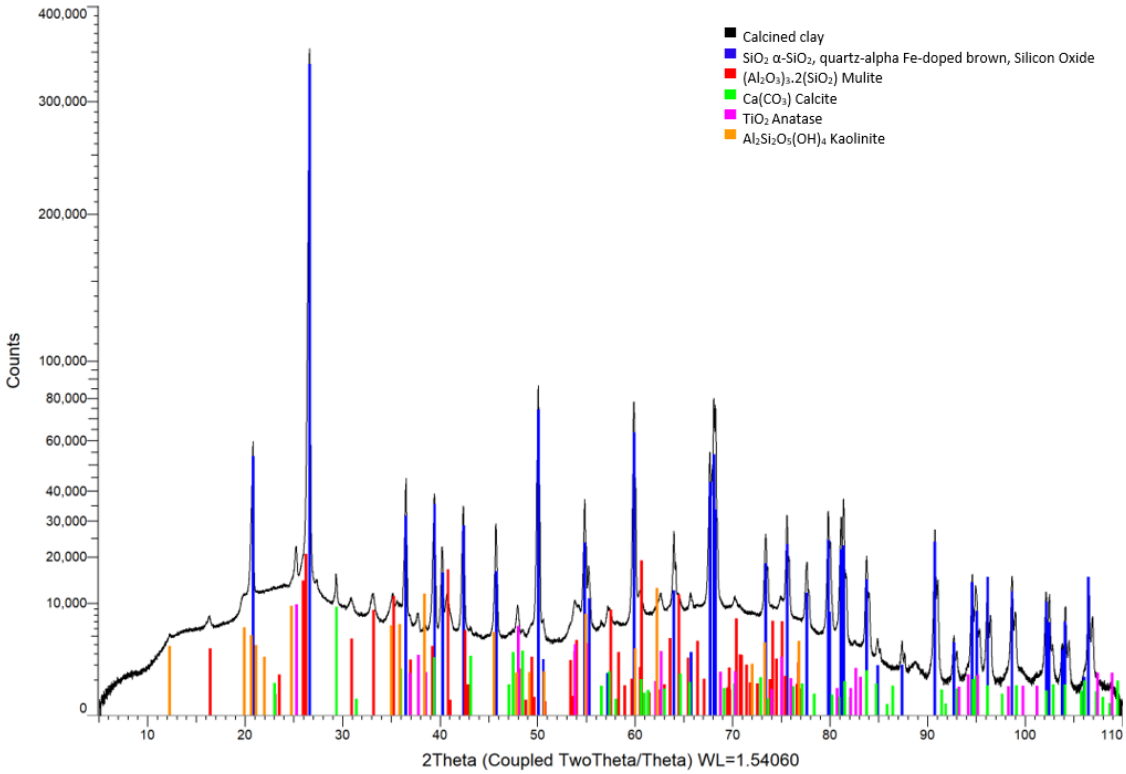

Figure 4.2: XRD pattern sample calcined clay, intensity scale is square root.

4.2.2. Blast furnace slag (BFS)

The ground granulated blast furnace slag (BFS) is provided by Ecocem. The chemical composition is presented in Table 4.3.

Table 4.3: Chemical composition of BFS. Manufacturer: Ecocem.

Chemical composition [%]											
	SiO_2	**Al_2O_3**	**CaO**	**Fe_2O_3**	**K_2O**	**TiO_2**	**MgO**	**SO^3**	**Cl^-**	**S^{2-}**	**Na_2O**
BFS	35.60	13.12	37.97	0.37	0.66	0.7	7.24	0.08	0.028	0.91	0.31

Table 4.4: Characteristics of blast furnace slag.

	BET-SSA [m^2/g]	Average pore width by BET [nm]	Total pore volume [cm^3/g]	Bulk density [kg/m^3]	Amorphous content [%]
BFS	1.44	1.10	0.000396	2890	100

4.2.3. Fine aggregate (FA)

For the lab-scale printing setup, there is a size limitation to the particles used in 3D-printed concrete. Sand with a maximum grain size of 2 mm will be used as fine aggregate. The fine aggregate falls in the size range of 0.125 mm - 2 mm. The proportion of each grading by weight is as follows:

- 0.125-0.25 mm - 25%
- 0.25-0.50 mm - 50%
- 0.50-1.00 mm - 20%
- 1.00-2.00 mm - 5%

4.2.4. Activator solution

A sodium silicate solution (SS) with a molar ratio (MR) of SiO_2/Na_2O = 3.3 – 3.5 will be used. Its composition by weight is as follows:

- Na_2O - 8.25%
- SiO_2 - 27.50%
- H_2O - 64.25%

Sodium hydroxide (NaOH), with a purity of $>$ 98%, is first dissolved in regular tap water. The solution is then allowed to cool for at least 24 h and then mixed with sodium silicate solution (SS) to achieve the desired modulus for the alkaline activator.

4.2.5. Particle size distribution of BFS, CC and FA

The particle size distribution of the fine aggregate, blast furnace slag and calcined clay is given in Fig. 4.3. For the binding materials, the grain size distribution is measured with laser diffractometry. For the fine aggregate, the particle size distribution is determined by using a sieving machine. The particle size distribution of the dry binders containing 0-40% calcined clay is given in Fig. 4.4. In Table 4.5, volume dimensions with median size for calcined clay and blast furnace slag are given.

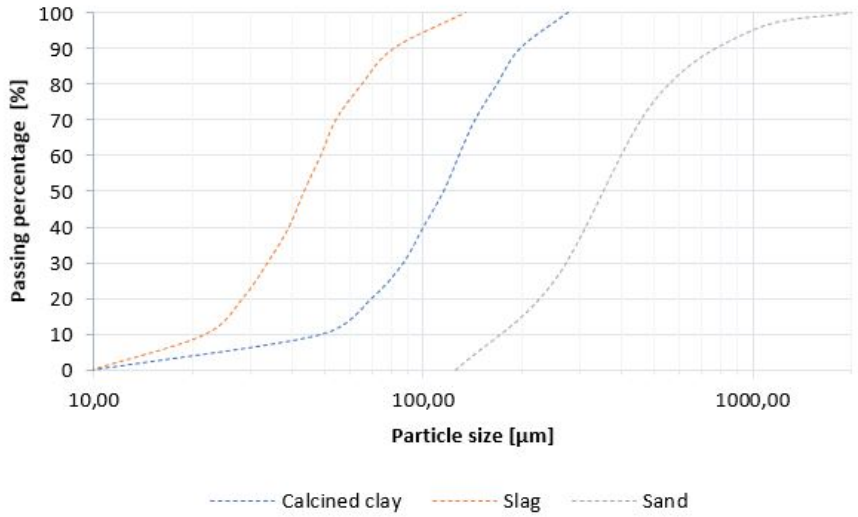

Figure 4.3: Particle size distribution of calcined clay, blast furnace slag and sand. The particle size of sand is determined by using a sieving machine. The grain size of the binding materials is measured with laser diffractometry.

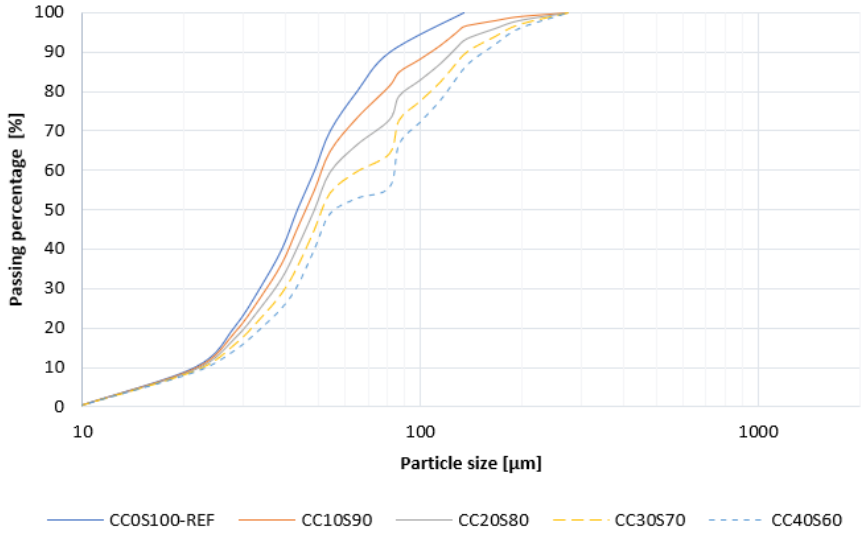

Figure 4.4: Particle size distribution of dry binders containing 0-40% calcined clay. Grain size of blast furnace slag and calcined clay is measured with laser diffractometry. The particle size distribution of the combined binders is calculated.

Table 4.5: Volume dimensions of precursors with median size.

Precursor	D_{10} [µm]	D_{50}[µm]	D_{90} [µm]
BFS	21.65	43.30	81.18
CC	48.71	114.74	195.92

From Fig. 4.3 and Table 4.5 can be seen that slag has a much smaller particle size compared to calcined clay. Adding calcined clay will improve the grading of the binder.

4.2.6. Preparation method

For 3D printing, the fresh mixtures will be prepared according to the procedure similar as proposed by *Chen et al. (2020)*. The procedure is given in Table 4.6.

Table 4.6: Timeline and procedures of fresh mortar preparation.

Time (min:s)	Steps followed
-4:00	Homogenizing the dry materials (binder + sand) at speed 1 (60 rpm) by a HOBART planetary mixing machine.
0:00	Adding the alkali solution and keeping speed 1.
3:30	Pause, scraping the bottom and wall of the container.
4:00	Mixing at speed 2 (124 rpm).
6:00	Stopping, and casting/printing.

4.2.7. Mixture designs

In Table 4.7, the mixture designs for the fast screening are given, in which the influence of 4 material parameters is investigated by using an orthogonal design approach. The first 16 mixtures are part of the orthogonal design. Starting from mixture 17, the mixture designs are manually changed to obtain good results for mixtures with high calcined clay content. Naturally, it is not feasible to evaluate all combinations. Therefore, the orthogonal design method provides a solution. A reduced number of mix designs needs to be evaluated, while every variable is taken into account. This method combines the accuracy of experimental design with the ability to produce rapid results by testing multiple components at once. The sand content in the mixtures is set at 800 kg/m^3.

Table 4.7: Mixture designs for the fast screening. CC=proportion calcined clay in binder. MR=modulus ratio. W/B=water to binder ratio. Na_2O=proportion sodium oxide in binder. S/B=sand to binder ratio.

MIX-ID	CC [%]	MR [-]	W/B [-]	Na_2O [%]	S/B [-]
1	20	0.5	0.4	6	1.5
2	40	1	0.43	8	1.5
3	10	0.5	0.37	4	1.5
4	30	1.25	0.46	4	1.5
5	10	1	0.46	6	1.5
6	30	1	0.4	4	1.5
7	20	1.25	0.37	4	1.5
8	10	0.75	0.43	4	1.5
9	40	0.5	0.46	8	1.5
10	20	1	0.43	6	1.5
11	30	0.5	0.4	6	1.5
12	40	0.5	0.4	8	1.5
13	40	1.25	0.4	8	1.5
14	20	1	0.4	6	1.5
15	10	1	0.4	6	1.5
16	30	1	0.4	8	1.5
17	0	1	0.4	6	1.5
18	30	1	0.43	8	1.5

19	30	1	0.46	8	1.5
20	20	0.75	0.4	6	1.5
21	40	1.25	0.43	8	1.5
22	40	1.25	0.46	8	1.5

4.3. Test methods

There are various testing methods available to measure the rheological behaviour and strength properties of printed concrete. Key aspects of ensuring successful 3D-printing of concrete are as follows:

- Pumpability;
- Extrudability;
- Buildability;
- Workability;
- Open time.

In Table 4.8, an overview of the available testing methods to determine the rheological behaviour of 3D-printed concrete is presented. A couple of testing methods will be selected for this research to determine the rheological behaviour of printed concrete, based on the complexity and cost-effectiveness of the testing method.

Printability parameters and mechanical properties that are important for the laboratory research will be discussed in the following paragraphs.

Table 4.8: Overview of the available rheological testing methods used in 3DCP. *(Jayathilakage, 2021)*.

Rheology testing method	**Measurable rheological parameters**
Rotational rheometer	Yield stress (static and dynamic) Viscosity Structural build-up rate (A_{thix}) Storage modulus (SAOS only) Loss modulus
Slump test	Yield stress
Flow table test	-
Direct shear test	Cohesion/yield stress Friction angle Dilation angle
Vane shear test	Yield stress Structural build-up rate (A_{thix})
Triaxial test	Cohesion/yield stress Friction angle Dilation angle Elastic modulus at early age Compressive strength at early age
RAM extrusion test	Uniaxial yield stress Shear yield stress Flow consistency and flow index
Squeeze flow test	Elongational yield stress Cohesion Friction angle Viscosity
Penetration test	Yield stress Structural build-up rate (A_{thix})

4.3.1. Fresh properties

Slump and slump-flow tests

The slump and slump-flow tests are both relatively easy test methods to give an indication of the printability of fresh mixtures. Determining the slump and flow of fresh mixtures is field-friendly and standardized across Europe through the Eurocode. Having a mixture with zero slump and high shape retention is ideal for 3D-printing applications, as it ensures that the filament keeps its shape when extruded. The spread diameters for the slump flow test should be as low as possible for 3D-printing applications, as this indicates great shape retention after extrusion and a high dynamic yield stress.

According to *Tay et al. (2019)*, the slump value depends greatly on the static yield stress of a fresh mixture. Determining the slump of a mixture may therefore also provide information on the shape retention and buildability of a concrete mixture. The slump-flow test for determining the flowability provides information about the pumpability and extrudability of fresh mixtures *(Ma et al., 2019)*. *Tay et al.* reports optimal printing quality and buildability for fresh mixtures with a slump value between 4-8 mm and spread diameter between 150-190 mm. The slump value is determined by using the Hägermann cone. *Ma et al.* found optimal printing quality and buildability for slump values in the range of 32-88 mm and spread diameter in the range of 174-210 mm. The slump value was determined with the *mini-slump cone* for mortar. These differences in optimal slump value and spread diameter are probably caused by differences in the setup of the 3D-printer and used slump cone in the slump test. In this study, the Hägermann cone will be used as well, with dimensions of a 70 mm upper internal diameter, 100 mm bottom internal diameter, and 60 mm height.

The target value for the slump and slump-flow will be based on the recommendations provided by *Tay et al. (2019)*: a slump value between 4-8 mm and a spread diameter between 150-190 mm.

Setting time

In order to ensure good interlayer bonding, interval time between layers should be smaller than the initial setting time. The goal is to prevent setting of one layer, before the other layer is deposited on top. Initial setting time indicates the time from which the fresh mortar starts to lose its plasticity. After the final set, there is no plasticity of the mortar left. The setting time is an important parameter for 3DCP, as it indicates the strength and stiffness development over time. The interval time between layers should be at least higher than the initial setting time to prevent weak, cold joints. The time needed for printing one layer depends on the scale of the construction. For printing on lab scale, a much smaller setting time will suffice, while printing on industry scale requires a delayed setting time. For 3D-printing on large scale, the printing period may be up to 3-4h for one building component *(Perrot et al., 2016)*. It is important to adapt the setting time of the concrete mixtures to the scale of the construction elements. The initial and final setting time is determined by using a Vicat apparatus (Fig. 4.5). The target value for the initial setting time will be in the range of 60-90 minutes to ensure continuity during printing.

Open time

The open time of a fresh mixture is often referred to as the printability window. The open time describes the timespan during which a mixture can maintain its extrudability. The loss of printability is mostly related to the increase of yield strength over time, due to formation of hydration products. The open time can be measured in various ways. It can be determined while printing, as the end of open time is marked by disruption of the extrusion process. It can also be measured with a Vicat apparatus (initial setting time) or with a slump flow test over specific time intervals. To simplify the testing procedure, only the initial and final setting time will be determined.

Figure 4.5: The automatic Vicat apparatus that is used in this study. (Automatic Vicat Apparatus, n.d.).

Rheology tests
Important parameters for description of the rheology of mortars can be identified as viscosity, yield stress and thixotropy. The yield stress is defined as the minimum shear stress at the onset of material flow. After exceeding the yield stress, the material will start to flow. The viscosity is a measure of a fluid's resistance to flow. To ensure good pumpability and flow of the mortar, it is necessary to maintain a low yield stress and viscosity during pumping. A low yield stress means that little stress is required to make the material flowable, hence making the mixture perfect for extrusion of cementitious materials. However, when the yield stress and viscosity are too low, the material will not be able to hold its shape when extruded and will therefore exhibit low buildability. The concrete mixture must therefore be thixotropic in nature. Thixotropy is a reversible, isothermal, time-dependent decrease in the apparent viscosity when a material is subjected to increased shear rate *(Mewis, 1979)*. Ideally, the mixture must show low viscosity during flow and a high yield stress at rest.

Rheology can be measured with different types of rheometers (Fig. 4.6), depending on material properties and setting time. The rheometer used in this study is given in Fig. 4.7. Only the parallel plate and vane rheometer is considered.

The rheological behaviour of a material can be described by various models, either linear or non-linear. The Bingham model is an example of a linear model (eq. 4.1). With a rheometer, the shear stress (τ) is measured under an imposed shear rate ($\dot{\gamma}$). A pre-shearing step (τ_0) is often performed to homogenize the mortar. In this way, an identical initial condition is ensured for each formulation. The Bulkley model (eq. 4.2) is a nonlinear model to describe rheological behaviour of cementitious materials. The non-linear equation of the Bulkley model is expressed by the exponent n, which either indicates shear-thickening behaviour (n $>$ 1), shear-thinning behaviour (n $<$ 1) or the Bingham model (n = 1).

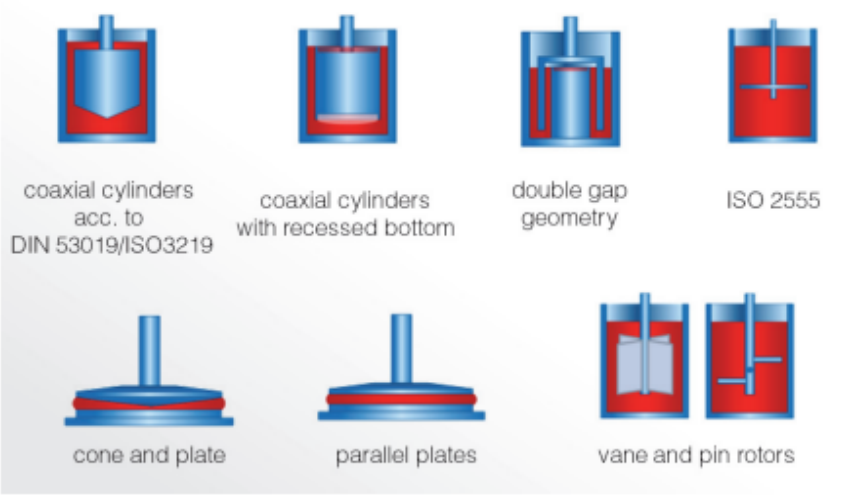

Figure 4.6: Overview of different types of rheometers. *(Rheometers | Viscometers | Thermo Fisher Scientific - NL, n.d.)*.

Figure 4.7: Rheometer used in the study. *(Modular Compact Rheometer: MCR 102e/302e/502e, Anton-Paar.com, n.d.)*.

$$\tau = \tau_0 + K\dot{\gamma} \tag{4.1}$$

4.1: Bingham model.

$$\tau = \tau_0 + K\dot{\gamma}^n \tag{4.2}$$

4.2: Herschel-Bulkley model.

With:
τ=shear stress [Pa]
τ_0=yield stress [Pa]
$\dot{\gamma}$=shear rate [s^{-1}]
K=plastic viscosity [Pa.s]
n=power index representing the deviation from the Bingham behaviour [-]

There are various methods available to assess the rheological behaviour of cementitious materials (Table 4.8). Rheological behaviour can be characterized by determining the flow curves of the pastes. In Fig. 4.8, an example of a flow curve is given. Dynamic yield stress and plastic viscosity can be determined from the curves that fit the chosen model (either Bingham or Herschel-Bulkley). This method is perfect of simulation of the pumping process, in which the material is sheared before being extruded. A material that is shear-thinning is favoured in 3DCP-applications, as this would mean that the material is viscous at rest and fluid during shearing.

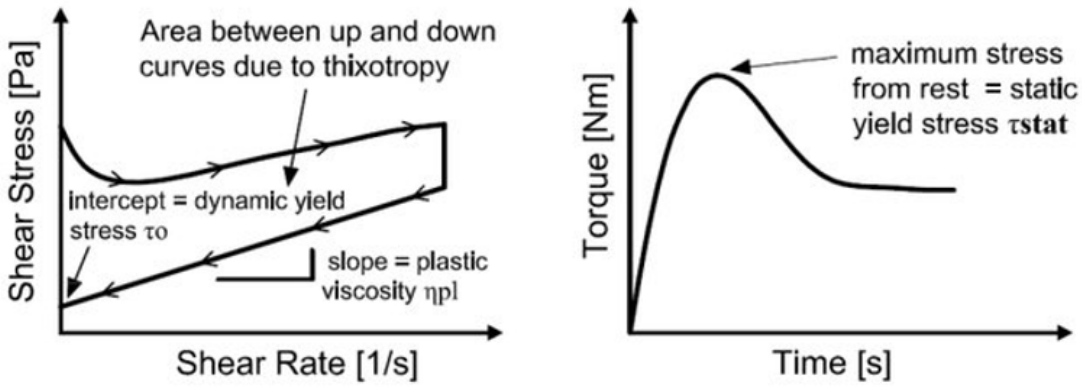

Figure 4.8: The flow curve of concrete - determination of the hysteresis loop. *(Gołaszewski et al., 2014)*.

In the study of *Dai et al. (2020)*, the experimental protocol consists of a couple of steps: a) pre-shearing at 200 s^{-1} for 30 s, b) a resting period of 30 s, c) increase of the shear rate in eight consecutive steps from 25 s^{-1} to 200 s^{-1} and d) decrease of the shear rate from 200 s^{-1} to 0 s^{-1} (Fig. 4.9). Each shear rate is maintained for 1 min to ensure that the paste reaches a steady-state condition. The whole process is completed in approximately 15 minutes. Aldin (2019) has conducted a similar experiment to determine the flow curve of the pastes, while assuming a Bingham model (Fig. 4.9). Aldin starts with a pre-shearing step, after which the shear rate is changed by 20 s^{-1} every 10 seconds. From 0 to 50 seconds, the shear rate is increased with increments to a maximum of 100 s^{-1}. After 50 seconds, the shear rate again gradually decreases to the original value of 20 s^{-1}.

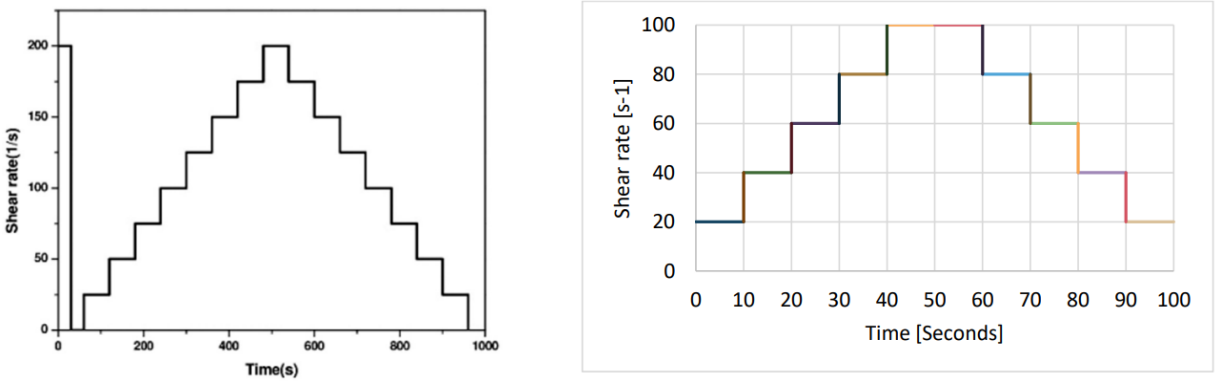

Figure 4.9: Testing protocol in the study of *Dai et al. (2020)*. b) Testing protocol in the study of *Aldin (2019)*.

The Danish Technological Institute has demonstrated that mixtures containing CEM I and fly ash with a plastic viscosity and dynamic yield stress in the ranges of 38.7 ±4.5 Pa.s and 0.59 ±0.08 kPa respectively were suitable for pumping and extrusion. For mixtures containing CEM I and limestone filler, other values for the plastic viscosity and yield stress were recommended: 21.1 ±2.4 Pa.s and 0.27±0.03 kPa respectively *(Thrane et al., 2009). Le et al. (2012)* recommends values for the dynamic yield stress in the range of 0.3-0.9 kPa to prevent blockage during pumping and filament failure during extrusion. These values are in accordance with the findings of the Danish Technological Institute. These recommendations all are applicable for printable mortars. *Alghamdi et al. (2019)* & *Nair et al. (2019)* recommend a dynamic yield stress in the range of 150-500 Pa for extrudable and printable pastes.

As the rheology will be investigated on paste level, the target value will be based on recommendations of *Alghamdi et al. (2019)* & *Nair et al. (2019)*: a dynamic yield stress in the range of 150-500 Pa. There is no specific target value for the viscosity. The goal is to have a mixture that shows fast recovery in viscosity after extrusion. The material should regain its strength rapidly after extrusion. To ensure this behaviour, viscosity should be low during pumping and high at rest. The flow test will be performed with a vane shear rheometer to investigate the very-early rheological behaviour of calcined and slag based AAMs.

Structural build-up

Typically, 3D-printed cementitious materials show an increase in static yield stress with time. It's necessary to study the development of static yield stress up to 30 minutes starting from the time of mixing to ensure that the evolution of the static yield stress and viscosity is fast enough for good buildability and stability of the layers. This indicates that 3D-printed concrete should inhibit rapid yield strength evolution, transitioning from a pumpable mix to a strong, high yield strength mix.

Small-amplitude oscillatory sweep (SAOS) test is an example of a test method to obtain information on structural build-up of cementitious materials. The response of the material subjected to a continuous sinusoidal excitation is measured in SAOS testing. The SAOS-test is commonly used to evaluate the viscoelastic properties of fresh cementitious materials. The excitation is kept in the range of linear viscoelastic domain (LVED) of the cementitious material to ensure that the sample is not influenced nor ruptured during structural evolution. The method can therefore be considered as non-destructive. The measured responses can be converted to parameters such as the storage modulus (G') and the loss modulus (G"). The storage modulus provides information about the amount of energy stored in the structure and represents the elastic behaviour of a material. It can be directly used as the Elasticity modulus in a linear static analysis. Contrarily, the loss modulus provides information about the energy that is lost in each cycle and represents the viscous behaviour of a material. If the material is an ideal solid, the loss modulus will be zero, as the material is perfectly elastic. If the material is an ideal liquid, the storage modulus will be zero, as there is no rigidity. Two test methods are generally performed before starting the SAOS-test, namely the oscillatory frequency sweep and the oscillatory amplitude sweep method. In the oscillatory frequency sweep test, the amplitude is kept constant, while the frequency is incrementally increased up to 100 Hz. This method is performed to find an appropriate frequency for the SAOS-test. In the oscillatory amplitude sweep test, the frequency is kept constant, while the amplitude is increased

incrementally above the critical strain limit of the mix. This method is used to determine the critical strain amplitude. After performing both tests, the oscillation in the SAOS-test is performed with a constant frequency and amplitude (smaller than the critical strain amplitude). *Moeini et al. (2020)* points out that the SAOS-test is mainly suitable for determining the structural build-up of already printed material, as the material is considered in an undisturbed state.

In the study of *Dai et al. (2022)*, a SAOS test is performed to measure the structural build-up over time. The strain amplitude is kept at 0.005%, with a constant frequency of 1 Hz, to guarantee that the fresh paste remains in the linear viscoelastic domain. After mixing, the fresh mixture is subjected to a pre-shearing step to obtain a reference state. After pre-shearing, a shear cycle is initiated, that is repeated a couple of times. In the study of *Dai et al. (2022)*, the shear cycle depicted in Fig. 4.10 is assumed.

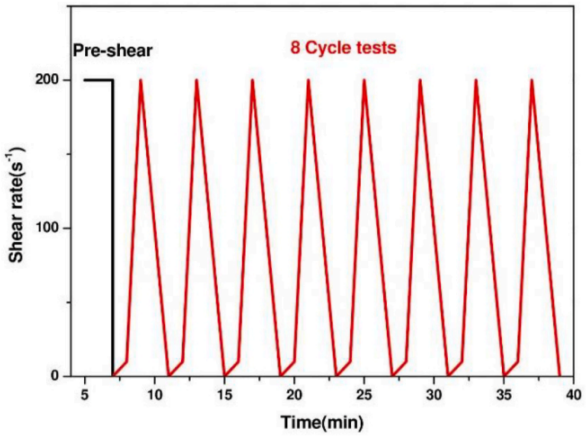

Figure 4.10: Testing protocol of shear cycle tests. *(Dai et al., 2022)*.

In this study, the SAOS-test will be executed at time intervals of t=0 min, t=10 min, t=20 min and t=30 min.

The constant shear rate (CSR) test is another method that can be used to evaluate the structural build-up of printable materials. It is typically used to measure the static yield stress evolution. In the test, a quasi-static rotational velocity (commonly 0.1–0.001 s^{-1}) is applied for flow onset. An example of a testing protocol can be found in Fig. 4.11. In the study of *Zhou et al. (2022)*, the testing protocol consists out of the following steps: a) pre-shearing at 0.5 s^{-1} for 60 s, b) rest for 120 s, c) shearing at a constant rate of 0.01 s^{-1} for 60 s and d) take out the vane, let the material rest and repeat all of the previous steps every 20 min. The peak stress that is responsible for flow onset, measured during each constant shear test, is recorded as the static yield stress of the material.

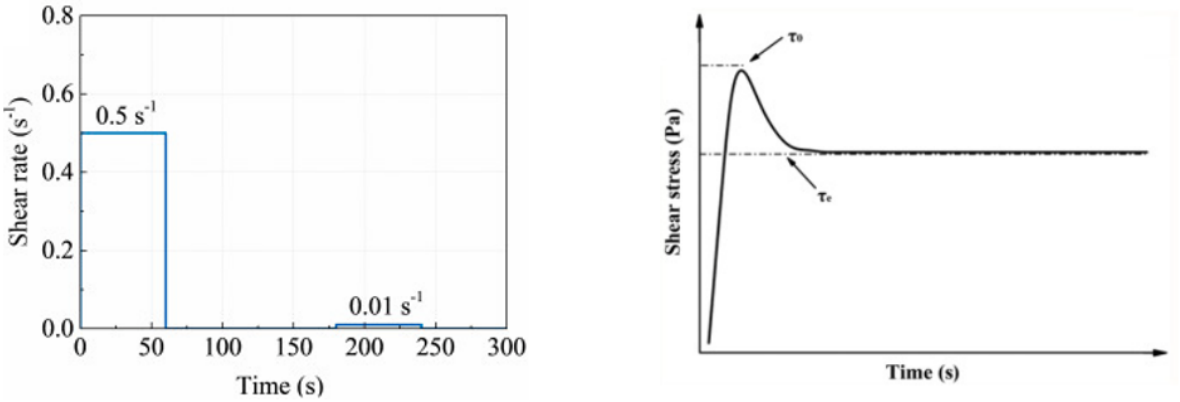

Figure 4.11: Testing protocol of a constant shear test. *(Zhou et al., 2022)*. b) Typical shear stress curves under constant shearing. Peak shear stress (τ_0) represents the static yield stress *(Chen et al., 2020)*.

As the material is in a disturbed state after shearing, the constant shear rate test is good for assessing the yield stress of newly deposited material. Although many researchers use this method to assess the yield stress evolution, it does not necessarily coincide with the printing process. For determining the evolution of the strength of the material at rest, the SAOS-test is more fitting for 3D-printing applications. The SAOS-test will provide adequate information on the structural build-up. The static yield stress can be determined from the flow curve. The structural build-up will be determined with a parallel-plate rheometer to account for the fast setting of some mixtures.

4.3.2. Mechanical properties and green strength

For 3D-printed concrete, early age strength development is of significant importance. It ensures that yield stress evolution of the bottom layers is sufficient before other layers are deposited on top. This is necessary for good buildability of the mortar layers, so that failure between subsequent layers is prevented. It's therefore recommended to ensure a high early compressive strength. In this study, the strength development is divided into two parts: green strength in the first 3 hours and compressive strength at 1, 3 and 7 days.

Green strength

In the study of *Perrot et al. (2016)*, the building rates are simulated. According to this study, it will take at most 3 hours to print a large concrete component with a height of 3 m. When the mixing and transporting time is taken into account, a timespan of 4 hours is sufficient to evaluate the green strength development to assess the structural build-up of the printed material. The green strength is evaluated by determining the uniaxial unconfined compressive strength at early age, e.g. within the first two hours after printing. The method proposed by *Wolfs et al. (2018)* will be used to determine the green strength of the printed samples. The uniaxial unconfined compressive test will be performed on cylindrical samples with a diameter of 53 mm and a height of 95 mm. Furthermore, the test will be performed at the ages of 0 min, 15 min, 30 min, 1 h, 2 h and 3 h to determine the green strength evolution over time. Time zero is recorded after mixing. The fresh mixtures will first be compacted before being demoulded and tested. In Fig. 4.13, the uniaxial unconfined compressive test setup used in this study is given.

Figure 4.12: Schematic of uniaxial unconfined compression test (left) and photograph of a sample (right). The white dots are strain measurements points. *(Wolfs et al., 2018)*..

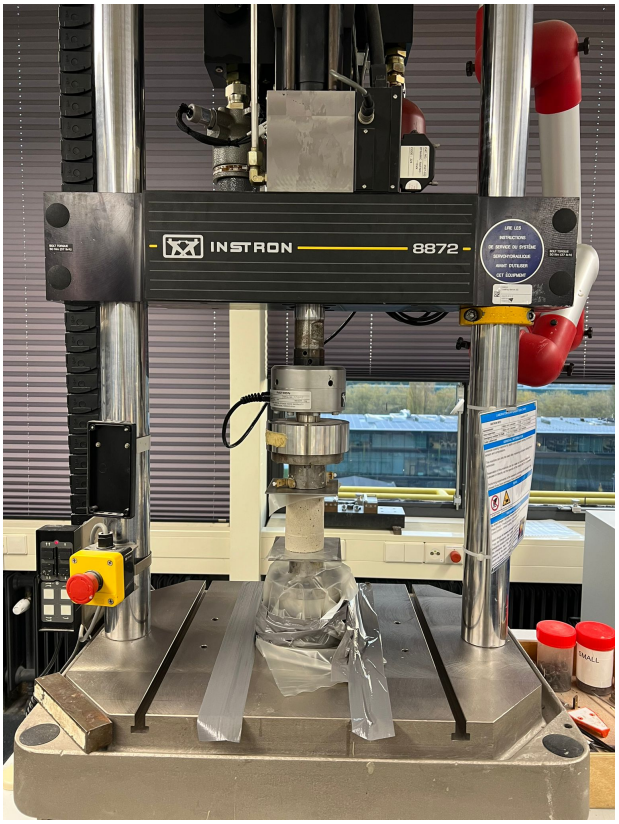

Figure 4.13: Test setup for the uniaxial unconfined compressive strength, with the Instron machine. Cylindrical samples have a diameter of 53 mm and a height of 95 mm.

The target value for the green strength is based on an actual large-scale application of a 3D-printed concrete manufacturer. In approximately 30 minutes, a column with a height of 2 m can be printed. To achieve such a height without collapsing, the material needs to develop a green strength within 30 minutes that is higher than the stress induced by the self-weight of the total structure on the bottom layer. For the column, a hollow cylindrical form is assumed with a height of 2 m and a outer diameter of 40 cm. The thickness per printed layer will be roughly 20 mm. For these assumed dimensions, the material needs to reach a strength of at least 44 kPa within 30 minutes to be able to withstand the self-weight of all the layers. The schematization of the 3D-printed column is provided in Fig. 4.14.

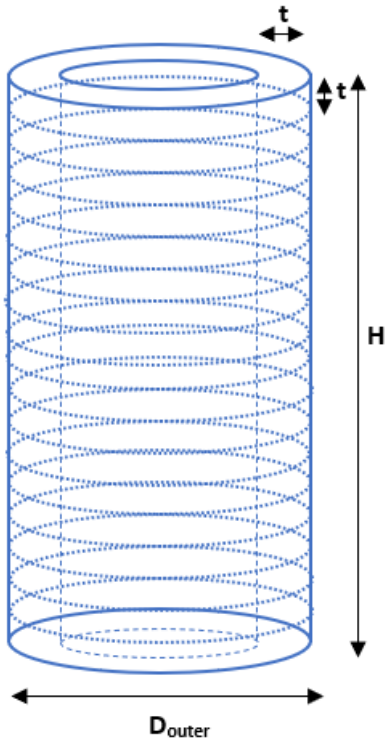

Figure 4.14: Schematization of 3D-printed column.

Compressive strength
The compressive strength is monitored over time by preparing mold-cast mortar specimens (160x40x40 mm^3) and testing the specimens at the material ages of 1, 3 and 7 days. The specimens will be sealed and cured in ambient conditions (20 $\pm$ 2 °C, and above 95% RH) before testing. A loading rate of 2.4 kN/s is employed to perform the compressive strength test, which is in accordance with NEN-EN 196-1. For each mixture, the average value of the compressive strength is obtained by testing three specimens.

4.3.3. Hydration
Characterization of hydration of concrete is a key factor in understanding the fresh properties of concrete, such as rheology, workability and green strength as well as the mechanical properties. The study will therefore partly be devoted to understanding the hydration kinetics of calcined clay and slag based alkali-activated materials.

Hydration of alkali-activated materials can be understood by assessing the heat release, the solid phases and the microstructure. In Fig. 4.15, the various characterization methods to determine the early-age hydration are illustrated. Each method has its purpose, either to determine the heat release, characterization of the solid phases or the microstructure of the alkali-activated materials. These different characterization methods will be further explained in the following paragraphs.

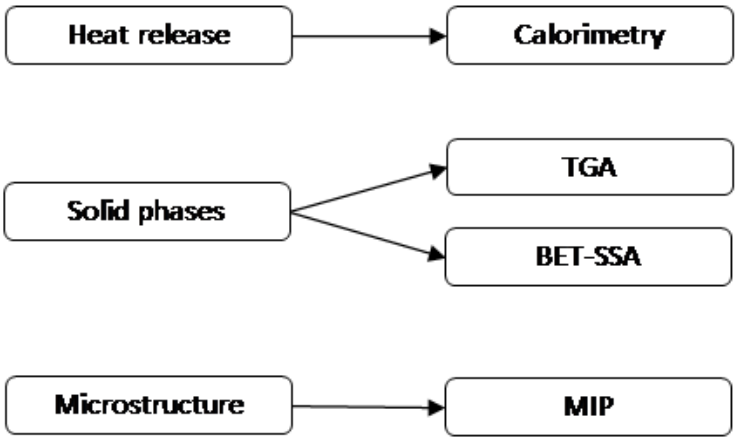

Figure 4.15: Overview of the hydration characterization methods used in this study.

Isothermal calorimetry
An eight-channel TAM Air isothermal calorimeter is used to determine the reaction heat induced by hydration during the first 7 days. The heat evolution that is measured with isothermal calorimetry can provide information on hydration kinetics. There is often a strong correlation between heat evolution and strength development of cementitious materials *(Frølich et al., 2016)*.

For each mixture, 5 g of freshly prepared paste is filled into a 20 mL glass vessel. The glass vessel is then placed in the calorimeter under 20 °C. The heat values are recorded each 20 s over a time span of 7 d. In Fig. 4.16, the eight-channel TAM Air isothermal calorimeter is shown.

Figure 4.16: TAM Air isothermal calorimeter.

Thermogravimetric analysis (TGA)
A thermogravimetric analysis (TGA) is typically used to define water evaporation mechanisms which cause the loss of material weight due to controlled heating. In a TGA, the weight loss is measured while the paste samples are exposed to an increasing temperature (up to 1000 °C). Before performing TGA, the

paste samples are crushed and grounded at the time of testing until fine enough to pass through a 75 µm sieve completely. Afterwards, the powders from the paste samples are soaked in isopropanol to stop the hydration process and then dried using an air pump. The samples are then prepared to be weighed less than 5 mg. Furthermore, the instrument is set to heat from 40 °C to 1000 °C at 10 °C/min in an argon environment. The TGA-analysis will be performed at the material ages of 1 d and 7 d after casting to assess the gel formation of the various mixtures.

BET specific surface area (SSA)

For the formation of geopolymers, aluminosilicate sources are first dissolved in an alkali metal hydroxide and/or alkali silicate-solution. After this dissolution process, a polycondensation process is initiated, in which aluminates and silicates are tetrahedrally linked. Measuring the evolution of the BET specific surface area can give an indication of the stiffness evolution of the material.

According to *Perrot et al. (2016)*, the printing period for one large building component may be up to 3-4 hours. To link the very early-age hydration of the material to the fresh properties of printed concrete, it's necessary to look at the hydration in the first 3-4 hours. Therefore, the SSA_{total} is measured for each mixture at the material ages of 1 h and 3 h to understand the very early-age hydration. The BET specific surface area is determined by physical adsorption of a gas, nitrogen gas in this case, onto the surface of the sample at cryogenic temperatures to quantify the specific surface area. The Brunauer–Emmett–Teller (BET) theory can be applied to systems of multilayer adsorption (Fig. 4.17). Based on the applied vapor pressure, the specific surface area can be determined from the BET-theory.

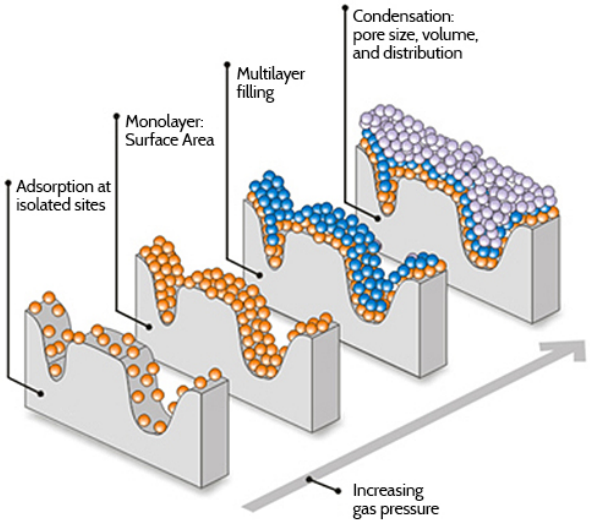

Figure 4.17: Principle of measuring the BET-SSA. *(Micromeritics, n.d.)*.

To stop the hydration of the paste, solvent exchange with isopropanol is employed. To determine the SSA of the calcined clay and slag based alkali-activated material, dry powders (after hydration is stopped) are gently homogenized in an agate mortar. A BET multi-point nitrogen (N2) physisorption apparatus (Gemini VII 2390) is used to measure the SSA_{total} of the dry powders (Fig. 4.18). The evolution of the specific surface area will be determined within the first 3 hours after casting, at times t=1 h and t=3 h.

Figure 4.18: Gemini VII 2390, used to determine the BET-specific surface area. *(Micromeritics, n.d.)*.

Mercury Intrusion Porosimetry (MIP)
Mercury intrusion porosimetry (MIP) is a widely used technique for characterization of the pore structure in cementitious materials. With the use of image analysis, the relationship between MIP and pore distribution and connectivity can be explored. MIP is based on the assumption that a nonwetting liquid will only intrude capillaries under pressure. Mercury is forced into the pores by applying pressure. The relationship between the pressure and the capillary diameter is as follows, according to *Washburn*:

$$P = \frac{-4\gamma \cos(\theta)}{d} \tag{4.3}$$

4.3: Relation between pressure and capillary diameter *(Washburn)*.

With:
P = pressure
γ = surface tension of the liquid
θ = contact angle of the liquid
d = diameter of the capillary pore

Before performing MIP, the mortar samples are crushed into small pieces and soaked in isopropanol for several days to stop the hydration process. The samples are then dried in a vacuum oven for approximately two weeks to remove the free water and the isopropanol. MIP will be performed at the material ages of 1 d and 7 d after casting to assess the pore structure of the various mixtures.

MIP is a widely used technique because of its simplicity. However, the accuracy of the technique is questionable to some extent. For example, large pores might be accessible by narrow throats. This technique misrepresents the size of these large pores by its narrow throats. In literature, this is referred to as the 'ink bottle'-effect. This method may still provide an approximation of the pore size distribution, despite its limitations.

4.3.4. Shrinkage

Shrinkage-induced cracking depends on various factors, like the degree of restraint, stress relaxation, duration of restraint, moisture gradient, etc. As shrinkage-induced cracking is one of the main problems related to large-scale production of alkali-activated materials and 3D-printed concrete, it will be considered in this study as well. Two types of shrinkage will be monitored in this study:

- *Autogenous shrinkage*: volume change occurring without any moisture exchange with the environment. It is a result of internal reactions within the mortar during hydration.
- *Drying shrinkage* volume change under the combined effects of moisture exchange with the environment and internal reactions within the mortar during hydration.

The shrinkage behaviour can be examined in two restrained conditions: free and fully restrained. In this study, only the unrestrained shrinkage will be determined. The tests will be performed on 3D-printed concrete for an accurate judgement of the shrinkage behaviour. The goal is to assess the amount of shrinkage of the various mixtures and to determine whether the mixtures are suitable for 3D-printing.

Unrestrained shrinkage test

In unrestrained conditions, the specimen is free to deform in length. Prisms of dimensions 40x40x160 mm^3 will be prepared for the test. Directly after casting, the prisms will be sealed with plastic to prevent moisture loss. After the first 24 h, the prisms will be demoulded and placed in a climate chamber with a relative humidity of 65% and a temperature of 20°C until testing. To determine the autogenous shrinkage, the prisms will be kept sealed with plastic and waterproof tape after demoulding for the entire duration of the experiment. Measurements for the autogenous shrinkage start after demoulding. For the drying shrinkage, the prisms will be kept sealed for a period of 7 days after demoulding. After 7 days, the specimens will be unsealed and the drying shrinkage will be measured immediately for a time span of 28 days. In Fig. 4.20, the sealed and unsealed specimens are depicted.

The length of the specimens is measured with a digital length comparator (Fig. 4.19). The initial length after demoulding (1 day) is assumed to be the original length of the specimen. The free shrinkage behaviour of the cast samples will be determined for 28 days. The linear shrinkage is calculated with the formula given in eq. 4.4.

$$\varepsilon_L = \frac{L_t - L_i}{L_i} \tag{4.4}$$

4.4: Formula linear shrinkage

With:
L_t = length at t days
L_i = initial length, taken as 160 mm

In the study of *Priyadarshi (2021)*, the rate of shrinkage is compared for cast and 3D-printed samples, for covered as well as uncovered conditions. According to *Priyadarshi*, the rate of shrinkage for cast samples is larger in case of uncovered curing conditions. The cast samples in uncovered conditions are exposed to autogenous as well as drying shrinkage, while drying shrinkage is prevented for samples in covered conditions. Furthermore, the 3D-printed samples show a higher shrinkage rate of 15-20% compared to the cast samples. This is probably caused by the larger amount of capillary pores in the 3D-printed samples due to a lack of compaction. As this study will focus on cast samples, it should be considered that the shrinkage may be larger for actual printed samples.

The target value for shrinkage will be based on a concrete mixture from Weber that is already successfully printed, with a total shrinkage of 1000 µm/m. Note that the measurement of this value is based on German standards (DIN 52540). The total shrinkage is measured after 91 days, with a total curing time of 28 days. Based on the Dutch standard NEN-EN 1992-1-1, the shrinkage can be estimated at 28 days. The estimated shrinkage is approximately 813 µm/m after 28 days. The target value for the shrinkage will therefore be below 813 µm/m. The calculations for the target value according to NEN-EN 1992-1-1 can be found in Appendix A.

Figure 4.19: Digital length comparator.

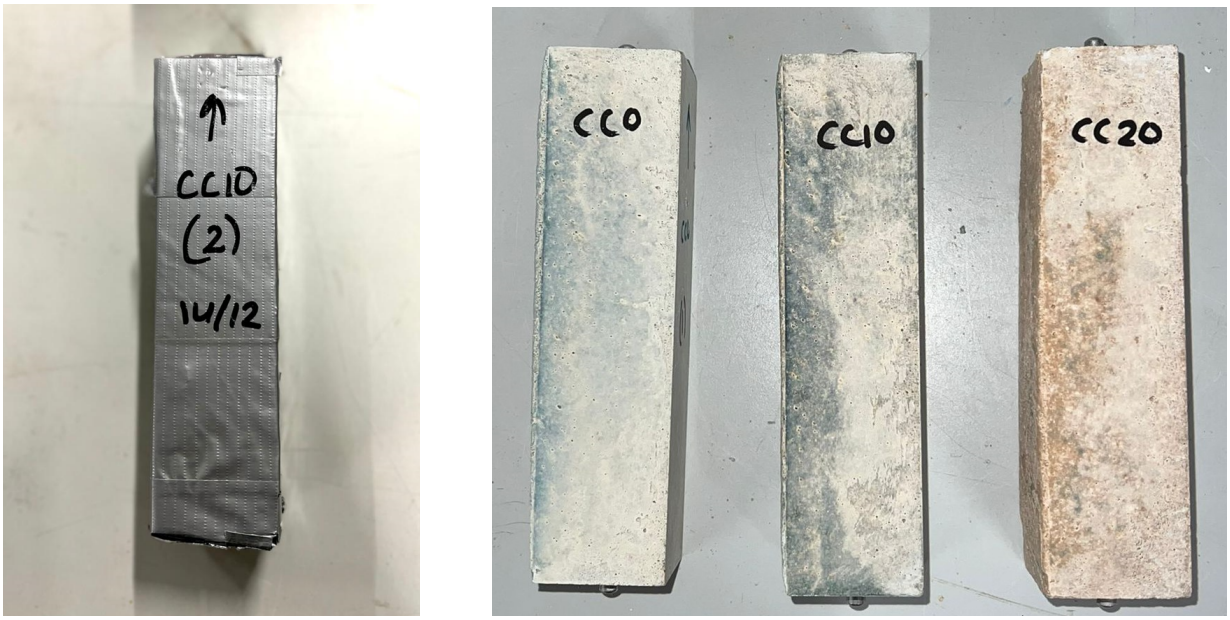

Figure 4.20: Left: sealed specimen for autogenous shrinkage. Right: unsealed specimens for drying shrinkage.

4.3.5. Target values

The target values for calcined clay and slag-based AAMs, for 3D-printing applications, are summarized in Table 4.9.

Table 4.9: Target values for the various parameters based on the literature study.

Property	Target value
Slump and slump-flow	*Tay et al. (2019)* recommends a slump value in the range of 4-8 mm and a spread diameter in the range of 150-190 mm for optimal printing quality and buildability.
Setting time	The target value for the setting time is chosen in the range of 60-90 minutes.
Rheology	The target value of the dynamic yield stress is based on recommendations of *Alghamdi et al. (2019)* & *Nair et al. (2019)*: a dynamic yield stress in the range of 150-500 Pa for extrudable and printable pastes.
Green strength	The green strength should be at least 44 kPa after 30 minutes for optimal buildability.
Shrinkage	Drying shrinkage should be smaller than 813 microstrain after 28 days.

Part II

Results and discussion

5

Fast screening

In this chapter, the results for the fast screening procedure are presented. Based on the fast screening, several promising mixtures are selected for further research on influence of calcined clay content. Promising mixtures are mixtures that show fitting properties for an application in 3D-concrete printing: zero slump, good shape stability and high early (1-day) compressive strength. The mixtures are generated by using an orthogonal design approach to combine the accuracy of experimental design with the ability to produce rapid results by investigating multiple components at once.

5.1. Slump and slump-flow

The slump value depends greatly on the static yield stress of a fresh mixture. Determining this property may therefore offer information on the shape retention and buildability of a mixture. A low slump-value indicates excellent shape retention for 3D-printing. The value for the slump-flow provides information on the pumpability and extrudability of fresh mixtures. *Tay et al.(2019)* reports optimal printing quality and buildability for fresh mixtures with a slump value between 4-8 mm and spread diameter between 150-190 mm. The recommended values will therefore be the target values for the fast screening.

In Table 5.1, values for slump- and slump-flow are presented for the 22 different mixture designs. The minus-sign denotes failure during casting, i.e. the mixture was too dry to be successfully casted.

Table 5.1: Slump and slump-flow.

Mixture	Slump [cm]	Slump-flow [cm]
1	1	18.5
2	1	17
3	-	-
4	1.5	20.5
5	3.5	25
6	0.5	17.5
7	-	-
8	2.5	24
9	2	23
10	1	20
11	0.5	18
12	1	18
13	-	-
14	1	17
15	1	17.5

16	-	-
17	1.5	19.5
18	1	17.5
19	2	20
20	1	18.5
21	-	-
22	0.5	13

5.2. Compressive strength

For 3D-printed concrete, early age strength development is of significant importance. It ensures that yield stress evolution of the bottom layers is sufficient before other layers are deposited on top. This is necessary for good buildability of the mortar layers, so that failure between subsequent layers is prevented. It's therefore recommended to ensure a high early compressive strength. For the fast screening, the 1-day compressive strength is used to select promising mixtures.

In Table 5.2, values for the 1-day compressive strength are presented for the 22 different mixture designs. The minus-sign denotes failure during casting, i.e. the mixture was too dry to be successfully casted.

Table 5.2: 1-day compressive strength.

Mixture	$\sigma_{c,1d}$ **[MPa]**
1	7.71
2	0.27
3	-
4	0.00
5	1.24
6	0.00
7	-
8	0.00
9	0.00
10	0.00
11	0.00
12	0.00
13	-
14	24.92
15	28.99
16	-
17	15.71
18	0.95
19	0.00
20	1.34
21	-
22	0.00

5.3. Concluding remarks

Based on the slump, slump-flow and 1-day compressive strength of the 29 mixtures, mixtures 1 and 15 are selected as the most promising mixtures (Table 5.3). These mixtures show almost zero slump and adequate strength development after 1 day. To determine the influence of calcined clay on fresh properties, mechanical properties and hydration, mixture 1 is selected for further research.

Table 5.3: Selected mixtures based on the fast screening.

MIX-ID	CC content [%]	MR	W/B	Na_2O [%]
1	20	0.5	0.4	6
15	10	1	0.4	6

The results show that a higher sodium oxide to precursor ratio is necessary to ensure strength development in the first day, for higher calcined clay content (up to 40%). In this study, the maximum sodium oxide to precursor rate was set at 8%. From an economical point of view, it would not be appealing to consider higher sodium oxide to precursor ratios, as this would result in a significant increase of the material costs. Higher ratios are also not appealing from an environmental point of view, as the environmental costs of the material would increase considerably. A concentrated alkali solution is very corrosive as a result of a high pH-value and high toxicity level. It may lead to handling issues during production. For this reason, mixtures with a low sodium oxide to precursor ratio are selected for further research. In the next stage of the study, the influence of different calcined clay to slag ratios on fresh properties, mechanical properties, hydration and shrinkage is investigated.

6

Influence of calcined clay content on AAMs

In the previous chapter, mixture 1 (CC=20%, MR=0.5, w/b=0.4, Na_2O=6%) is selected for further research on the influence of the replacement level of calcined clay in AAMs on fresh properties, mechanical properties and hydration. In Table 6.1, an overview of the new mixture designs is presented. All parameters will be fixed, except for the calcined clay content in the precursor.

Table 6.1: An overview of the mixture designs for the alkali-activated mortars. For the pastes, the same mixture design is used, excluding the sand.

MIX-ID	CC [%]	MR [-]	W/B [-]	Na_2O [%]	S/B [-]
CC0S100-REF	0	0.5	0.4	6	1.5
CC10S90	10	0.5	0.4	6	1.5
CC20S80	20	0.5	0.4	6	1.5
CC30S70	30	0.5	0.4	6	1.5
CC40S60	40	0.5	0.4	6	1.5

6.1. Fresh properties

6.1.1. Setting time

Table 6.2: Initial and final setting time according to EN 196-3 (on paste level).

Mixture	Initial setting time	Final setting time
CC0S100P-REF	30 min	160 min
CC10S90P	50 min	$>$ 7 h
CC20S80P	290 min	$>$ 7 h
CC30S70P	340 min	$>$ 7 h
CC40S60P	$>$ 7 h	$>$ 7 h

In general, the results show that for increasing calcined clay content, the setting time is increased and setting is therefore decelerated. The rapid setting time is attributed to the presence of slag in a calcined clay and slag-based AAM. This is in accordance with the study of *Huseien et al. (2018)* & *Hasnaoui et al.*

(2019), who mention decelerated setting for higher metakaolin content in a metakaolin and slag based AAM. The particle size plays an important role in the dissolution process and flow of an alkali-activated material. The fineness in particle size of calcined clay and the considerably lower CaO-content is highlighted as a possible reason for the increase in workability. The amorphous phases in calcium rich alkaline binders, such as blast furnace slag, contribute to an increased dissolution rate and therefore fast setting. Note that the initial and final setting time may decrease when fine aggregates are introduced into the mixtures, as the aggregates can absorb some of the water.

It can be concluded that increasing calcined clay content, as part of an alkaline binder, decelerates the setting of alkali-activated calcined clay and slag based materials.

6.1.2. Workability

Table 6.3: Slump and slump-flow. On mortar level.

Mixture	Slump [cm]	Slump-flow [cm]
CC0S100-REF	1.0	19.5
CC10S90	1.0	18.5
CC20S80	1.0	19.5
CC30S70	1.0	18
CC40S60	0.5	17.5

The workability for the various mixes was evaluated based on the slump and slump-flow test. The results do not show a clear trend for an increasing calcined clay content. *Huseien et al. (2018)* has found an increasing slump-flow for increasing metakaolin content in an alkali-activated calcined clay and slag based material, for replacement ratios between 0-15%. The fineness of metakaolin in comparison to blast furnace slag is mentioned as a possible reason for this effect. Similar results are found in this study for 0% calcined clay and 10% calcined clay: the slump-flow decreases when the calcined clay content is increased from 0 to 10%. However, further increasing the calcined clay content up to 20% does not result in a lower flowability. As calcined clay does not only contain metakaolin, but other impurities as well, this might influence the results. In Fig. 6.1, the influence of calcined clay content on workability is depicted.

To ensure a stable print with little deformation, it's important to have a cohesive mixture with zero slump. The mixtures demonstrate a maximum slump value of 1 cm, and a maximum slump-flow value of 19.5 cm. The target value for the slump and slump-flow is based on recommendations provided by *Tay et al. (2019)*: a slump value between 4-8 mm and a spread diameter between 150-190 mm. The slump values slightly exceed the target range, while most of the slump-flow values are within the target range. The mixtures showed great shape retention, which is desirable for use in 3DCP-applications.

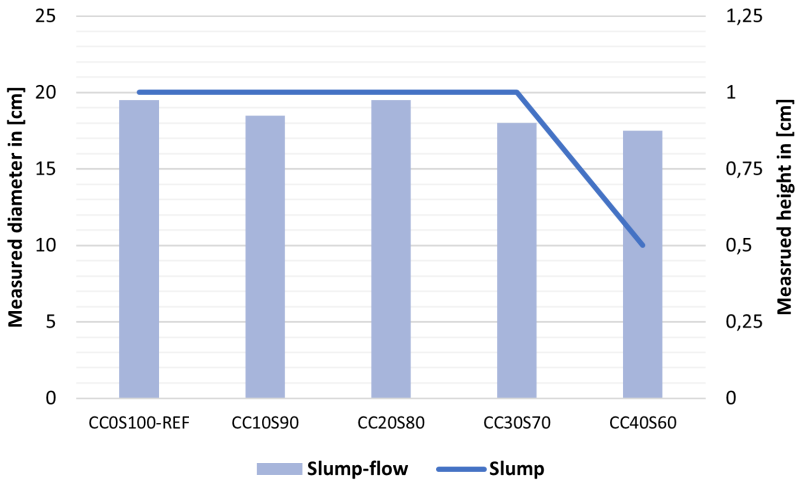

Figure 6.1: Slump and slump-flow in cm.

6.1.3. Rheology

The rheological properties of the various mixtures are measured by using a vane rheometer. The flow curves provide information on rheological properties, such as the static yield stress, dynamic yield stress and the plastic viscosity. A material that is shear-thinning is favoured in 3DCP-applications, as this would mean that the material is viscous at rest and fluid during shearing.

The flow test is performed for three paste mixtures (CC0S100, CC10S90, CC20S90) and repeated twice per mixture. The experimental protocol consists of a couple of steps:

1. Pre-shearing to homogenize the paste;
2. Increase of the shear rate from 0 to 100 s^{-1} in 90 s;
3. Constant shear rate of 100 s^{-1} for 60 s;
4. Decrease of shear rate from 100 s^{-1} to 0 s^{-1} in 90 s.

The flow curve test takes approximately 4 minutes in total and thus represents the very-early rheological behaviour of the alkali-activated pastes. The resulting flow curve for mixture CC0S100-REF is illustrated in Fig. 6.3. The flow curves for the other mixtures are provided in Appendix B.

The mixtures exhibit Bingham behaviour and are therefore described with the linear Bingham model, as described in eq. 4.1. The static yield stress, $\tau_{0,static}$, is determined from the pre-shearing step and is defined as the minimum stress required for initiating flow. The dynamic yield stress, $\tau_{0,dynamic}$, is the intercept of the fitted curve and is defined as the minimum stress for maintaining flow. The plastic viscosity, K, is the slope of the fitted curve and is defined as the resistance offered by a fluid to flow freely. In Table 6.4 and Fig. 6.2, a summary of the rheological properties is provided for the various mix designs. Fig. 6.4 shows the fitted curves, according to the Bingham model, and Fig. 6.5 shows the viscosity for an increasing shear rate for the three different paste mix designs

Table 6.4: Summary of the rheology of the alkali-activated pastes.

	$\tau_{0,static}$ **[Pa]**	$\tau_{0,dynamic}$ **[Pa]**	**K [Pa.s]**
CC0S100-REF	438,23	183,81	2,61
CC10S90	699,81	277,66	2,56
CC20S80	1063,15	324,47	2,62

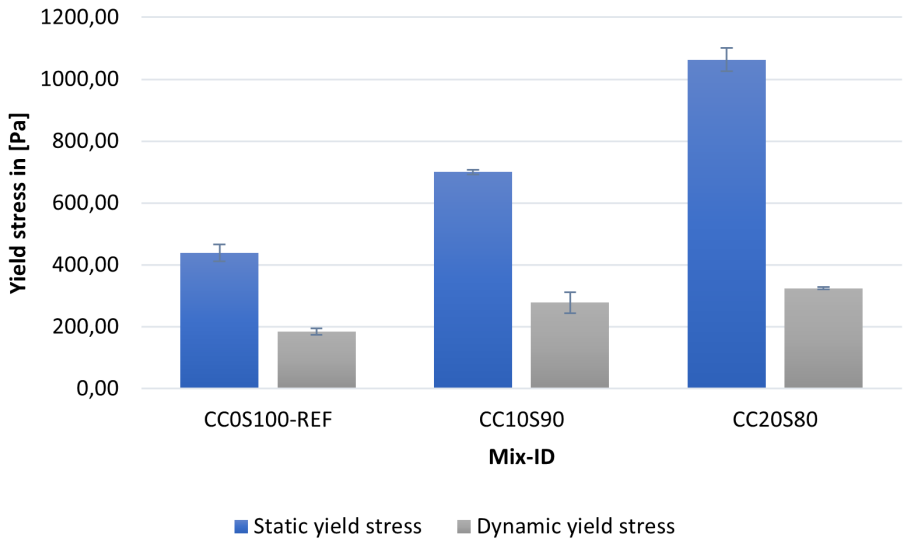

Figure 6.2: Static and dynamic yield stress of alkali-activated pastes.

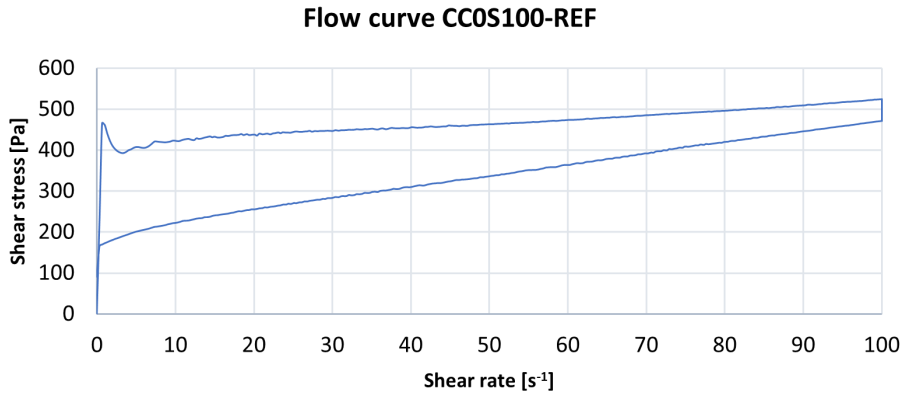

Figure 6.3: Flow curve for mixture CC0S100-REF.

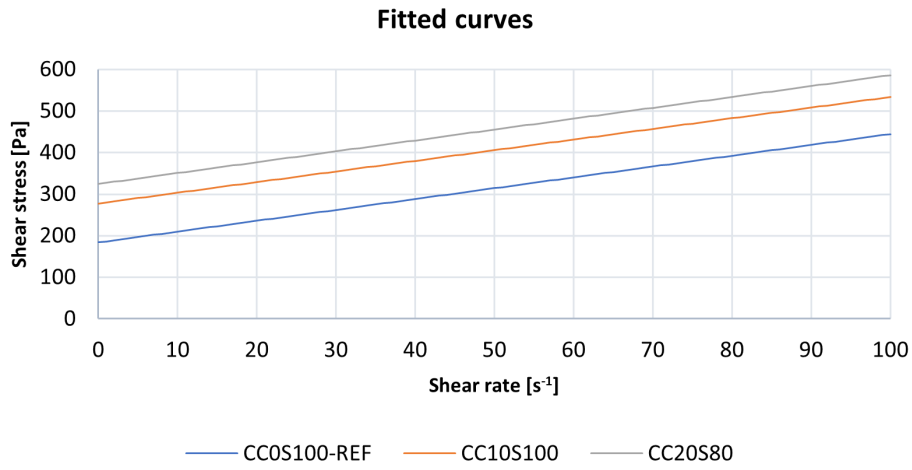

Figure 6.4: Fitted curves (Bingham model) for the mixtures CC0S100, CC10S90 and CC20S80.

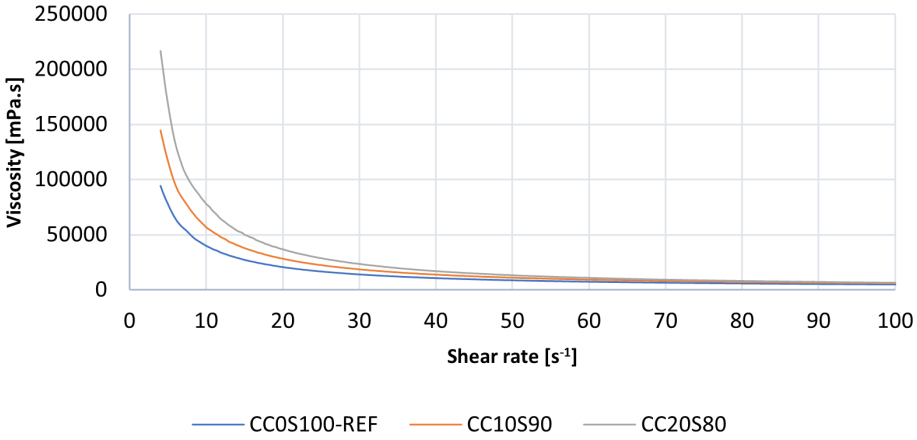

Figure 6.5: Viscosity for mixtures CC0S100, CC10S90, CC20S80.

From Table 6.4 and Fig. 6.2 follows that incorporation of calcined clay contributes to higher static and dynamic yield stress. An increase of the calcined clay content directly results in an enhanced static and dynamic yield stress. The results for the plastic viscosity do not show a clear trendline with respect to incorporation ratio of calcined clay in an alkali-activated material. Furthermore, all mixtures show shear-thinning behaviour: a decreasing viscosity for increasing shear rate. From Fig. 6.5 can be seen that an increasing calcined clay content results in higher viscosity. From the flow curves of the various mixtures can be seen that the shear stress values of the ramp-up curves are higher than the downward curves during the shear process. This is also a result of the shear-thinning behaviour.

The results are in accordance with the findings of *Hasnaoui et al. (2019)*. *Hasnaoui et al. (2019)* has found an increase of the yield stress and plastic viscosity for an increasing incorporation ratio of metakaolin in an alkali-activated metakaolin and slag based material. In the study, this effect is attributed to an increase of the specific surface area of the powder mix (slag + metakaolin), as metakaolin has a much higher fineness than slag. A similar explanation applies to slag based AAMs in which calcined clay is incorporated.

Because of the larger specific surface area and larger total pore area of calcined clay compared to blast furnace slag, as determined from the BET-method, more water is adsorbed onto the surface of calcined clay particles and absorbed into the open pores, therefore reducing the effective water to binder ratio. As less water is actually present in the alkali solution, separation of the particles is reduced and flocculation is enhanced. The lower effective water to binder ratio also contributes to a higher solid volume fraction. This ultimately results in a higher static and dynamic yield stress.

The target value of the dynamic yield stress is based on recommendations of *Alghamdi et al. (2019)* & *Nair et al. (2019)*: a dynamic yield stress in the range of 150-500 Pa for extrudable and printable pastes. From Table 6.4 can be seen that all mixtures exhibit a dynamic yield stress in the targeted range, meaning that these mixtures are likely to be successfully printed. The reference mixture is initially more flowable. Note that this experiment is performed on paste level, as a result of limitations of the used rheometer. The incorporation of sand might further increase the yield stress and viscosity, as some of the water will be absorbed by the fine aggregate.

6.1.4. Structural build-up

It's necessary to study the development of early-age strength and stiffness over time, i.e. the structural build-up, to assess the buildability of a material. 3D-printed concrete should inhibit rapid yield strength evolution, transitioning from a pumpable mix to a strong, high yield strength mix. Small-amplitude oscillatory sweep (SAOS) test is an example of a test method to obtain information on structural build-up of cementitious materials. The SAOS-test will be performed in a total time span of 1 h after mixing of the dry and wet ingredients.

Strain-sweep response

In Fig. 6.6, the strain-sweep responses of the AAM pastes with different calcined clay contents are presented. In the curves, two main regions are observed: a region in which the storage modulus remains almost constant and a region in which the storage modulus decreases due to shear-induced breakdown of the material. The critical strain is defined as the limit of the strain after which the storage modulus decreases, indicating a disturbance of the material. Strain values smaller than the critical strain fall in the linear viscoelastic region (LVER). For all mixtures can be seen that the value of the critical strain falls between 0.01 and 0.1%. The strain amplitude for the SAOS-test should therefore be chosen in this interval.

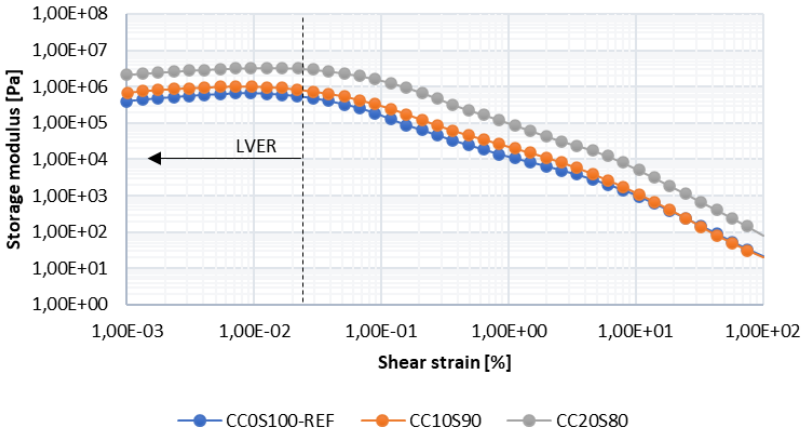

Figure 6.6: Linear viscoelastic range of various pastes by the strain-sweep tests.

SAOS-test

The SAOS-test is performed by using a parallel-plate rheometer to account for the relatively fast setting. The pastes are subjected to a sinusoidal excitation in the range of the linear viscoelastic region (LVER) to prevent disturbance or rupture of the material during testing. This method is therefore assumed to be non-destructive.

During a timespan of 1 h, the structural build-up of the different pastes is measured by converting the measurements to parameters like the storage modulus, loss modulus and loss factor. The storage modulus (G') provides information on the amount of energy stored in the structure and represents the elastic behaviour of a material. Contrarily, the loss modulus (G") provides information about the energy that is lost in each cycle and represents the viscous behaviour of a material. The loss factor is defined as the ratio between the loss modulus (G") and the storage modulus (G'), as given in eq. 6.1. The storage modulus and the loss factor will provide enough information on the evolution of the structural build-up and buildability over time *(Dai et al., 2020)*.

$$tan\delta = \frac{G''}{G'} \tag{6.1}$$

6.1: Formula loss factor.

With:
tanδ = loss factor [-]

G” = loss modulus [Pa]
G’ = storage modulus [Pa]

The evolution of the storage modulus is presented in Fig. 6.7 and Fig. 6.8, on a normal and logarithmic scale respectively.

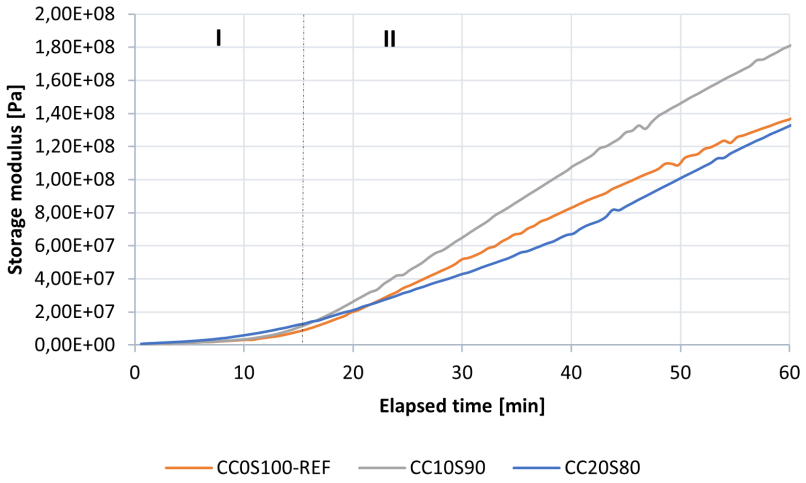

Figure 6.7: Evolution of the storage modulus over time (normal scale).

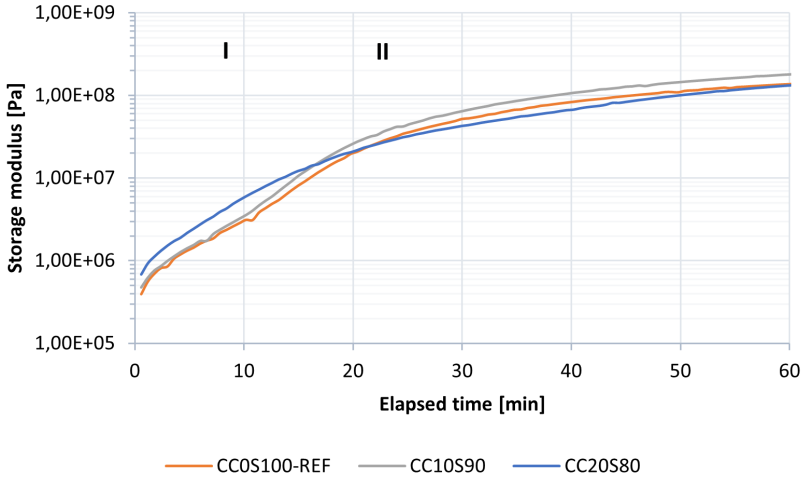

Figure 6.8: Evolution of the storage modulus over time on a logarithmic scale.

The evolution of the storage modulus (Fig. 6.7) can be divided into two main phases. The first phase is characterized by a very slow increase of the storage modulus. In this phase, BFS and CC particles are continuously dissolved in the alkali solution, but structural formation has not yet started. The increase in storage modulus in phase I is caused by flocculation and clumping of calcined clay and slag particles. In the second phase, a very sharp and fast increase of the storage modulus is observed. The dissolved ions from the first phase are starting to interact and hydration product is formed, which results in rigid networks. This explains the fast rate in structural build-up in the second phase.

From the plots also follow that the initial storage modulus in the very-early stage increases when 10% and 20% calcined clay (CC20S80) is incorporated into the binder. This may indicate an enhanced structural formation in the very-early stages, induced by inter-particle interaction forces. This observation is in line with the results from the flow curve test of calcined clay and slag based AAMs, in which an increasing static

and dynamic yield stress is observed for mixtures with increasing calcined clay content. The enhanced structural formation may be a result of the higher specific surface area of calcined clay and the improved grading of binary binders.

As time passes, the storage moduli for mixtures CC10S90 and CC0S100-REF become larger than CC20S80. A slower evolution in structural build-up was expected for mixtures with increasing calcined clay content, as AAMs containing more blast furnace slag typically show a higher structural build-up rate *(Dai et al., 2020)* as a result of rapid dissolution of slag particles and therefore rapid formation of very-early hydration product. That is not the case for mixture CC10S90, which shows the highest storage modulus after 1 h (30% higher than the reference mixture). The storage moduli after 1 h of the reference mixture CC0S100 and CC20S80 are very similar (3% difference). From the SAOS-test follows that mixture CC20S80 has the best structural build-up within the first 15 minutes after casting, while mixture CC10S90 shows the best overall structural build-up in 1 h.

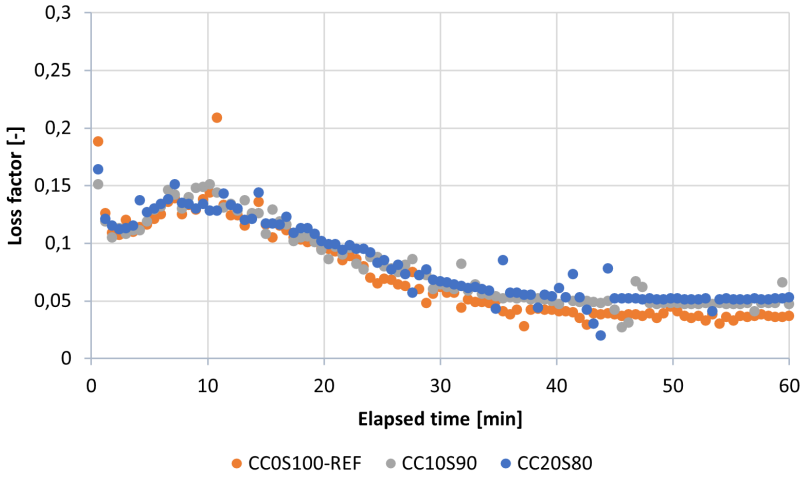

Figure 6.9: Evolution of the loss factor over time.

In Fig. 6.9, the evolution of the loss factor is given. Typically, pastes transition from viscous behaviour to elastic behaviour over time. As the loss factor is the ratio between the loss modulus (G") and storage modulus (G'), it is supposed to decrease over time as a result of ongoing hydration and structural formation. From Fig. 6.9 follows that the evolution of the loss factor is very similar for all mixtures. After 60 minutes, the loss factor does not decrease until zero, meaning that the material has not fully transitioned from viscous to elastic behaviour. The loss factor first increases until a maximum is reached, after which the loss factor steadily decreases. After approximately 10 minutes, the loss factor starts to decrease, which means that the transitioning from viscous behaviour to elastic behaviour has started. In the study of *Dai et al.*, a similar trend in the loss factor is observed with the peak at early ages. This peak is linked to a temporarily faster increase of the loss modulus (lost deformation energy) over the storage modulus (stored deformation energy).

6.1.5. Green strength

For 3D-concrete printing, early-age strength development is an important parameter. It ensures that yield stress evolution of the bottom layers is sufficient before other layers are deposited on top. This is necessary for good buildability, so that failure between subsequent layers is prevented. The early-age strength is determined at the material ages of t = 15 min, 30 min, 1 h, 2 h and 3 h.

In Fig. 6.10, Fig. 6.11 and Fig. 6.12, the load-displacement curves of mixtures CC0S100-REF, CC10S90 and CC20S80 are given. All specimens were subjected to monotonic loading. The changes in strength over time follow a clear trend line. The older the sample, the higher the peak load. The load increases almost linearly until the maximum load is reached. After the peak, the loading rate decreases, while the displacement continuously increases until final failure of the sample. This behaviour is a result of unloading of the material. The load-displacement curves are transformed into stress-strain curves. In Fig. 6.13, Fig. 6.14 and Fig. 6.15, the stress-strain curves of the various mixtures are given.

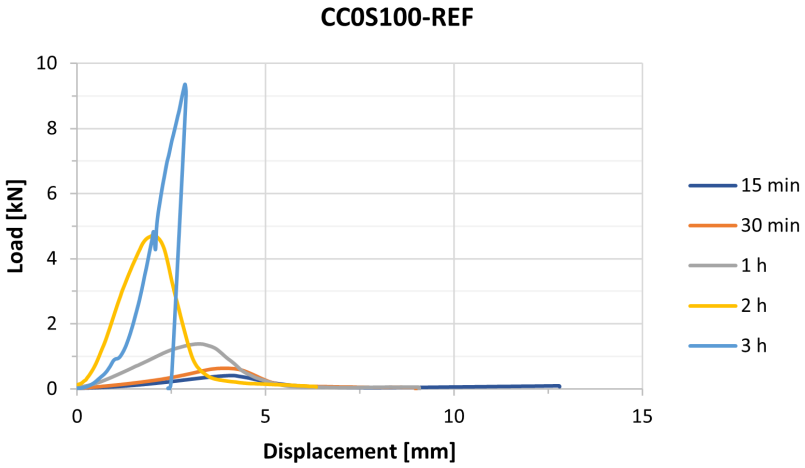

Figure 6.10: Load-displacement curve CC0S100-REF.

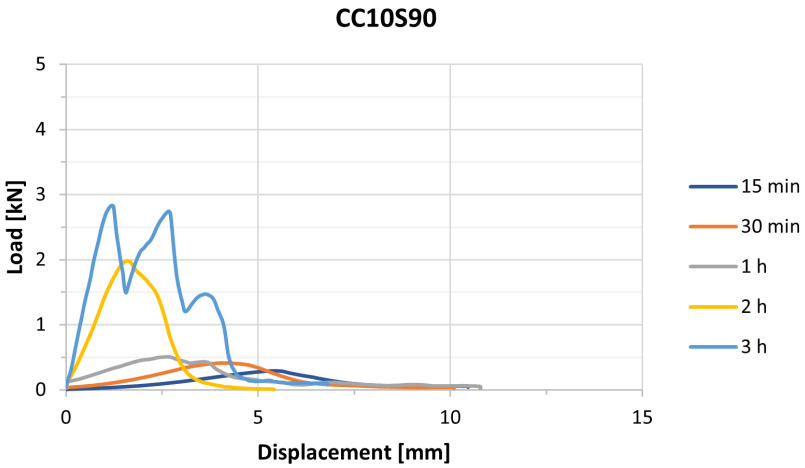

Figure 6.11: Load-displacement curve CC10S90.

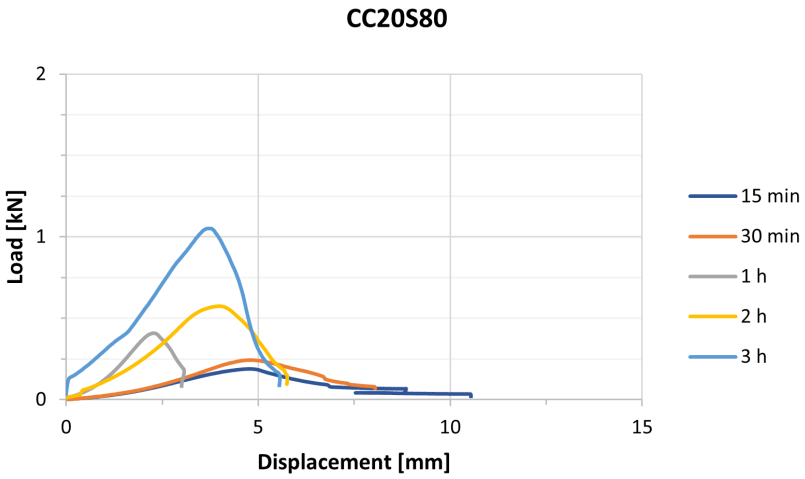

Figure 6.12: Load-displacement curve CC20S80.

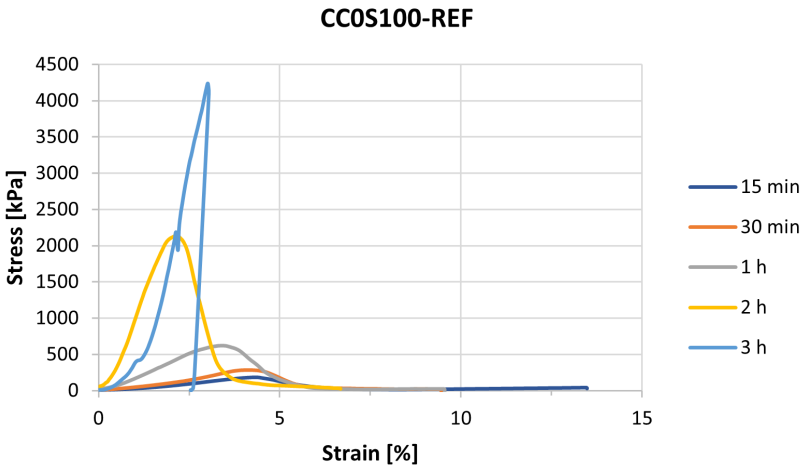

Figure 6.13: Stress-strain curve of CC0S100-REF.

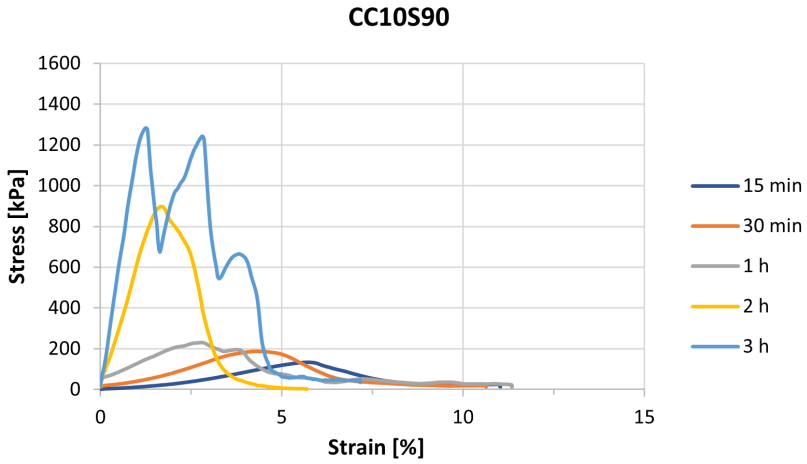

Figure 6.14: Stress-strain curve of CC10S90.

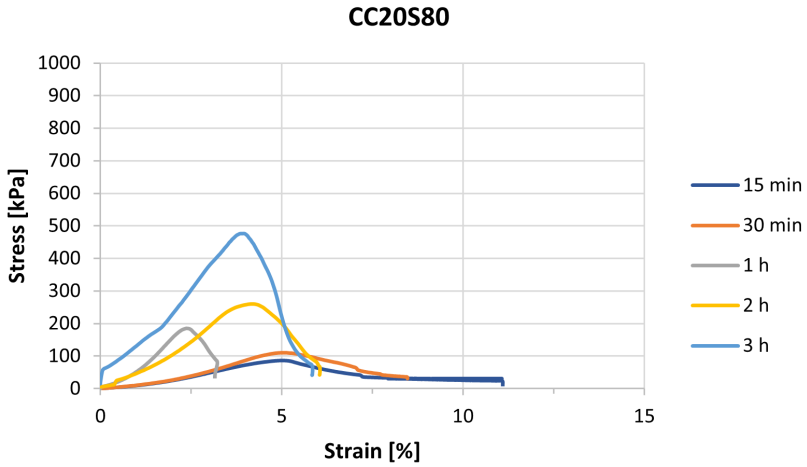

Figure 6.15: Stress-strain curve of CC20S80.

In Fig. 6.16, the green strength is given as a function of time for the various mixtures. From Fig. 6.16, it is clear that the increase in green strength is the highest for the reference mixture and decreases for increasing calcined clay content. The results shows that incorporating calcined clay in AAMs does not benefit the early-age strength. The early-age strength is considered to be an important parameter to evaluate the buildability of a cementitious material. For successful 3D-concrete printing, each layer should exhibit high early strength and fast green strength evolution to support the self-weight of the layers added on top.

Fig. 6.17, Fig. 6.18 and Fig. 6.19 show photographs of the damages samples at different material ages. From these figures, it is clear that young samples show a different crack pattern than older samples. At young ages, the specimens fail by barreling and show ductile behaviour, while older samples show a typical crack pattern (hourglass fracture pattern) and brittle behaviour. This observation is related to the setting time of the alkali-activated materials. The setting is decelerated for increasing calcined clay content, hence resulting in a longer setting time and more ductile behaviour, as the material has not set completely yet.

Although the green strength decreases for increasing calcined clay content in the precursor, this also means that extrusion is positively affected by addition of calcined clay. As a result of the decelerated

setting, the printability window will increase and less pressure is needed for extrusion of the material. The key is to find the balance between very-early strength and extrudability. Note that the green strength of the weakest sample (CC20S80) is still much larger than the target value of 44 kPa after 30 min. Buildability will probably not be the problem for these mixtures, rather the fast setting and fast decrease in workability.

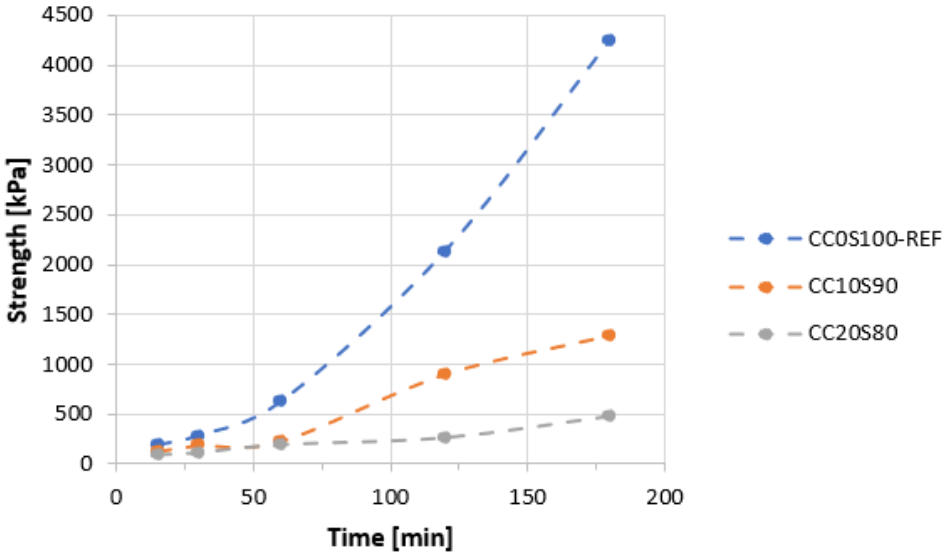

Figure 6.16: Green strength evolution.

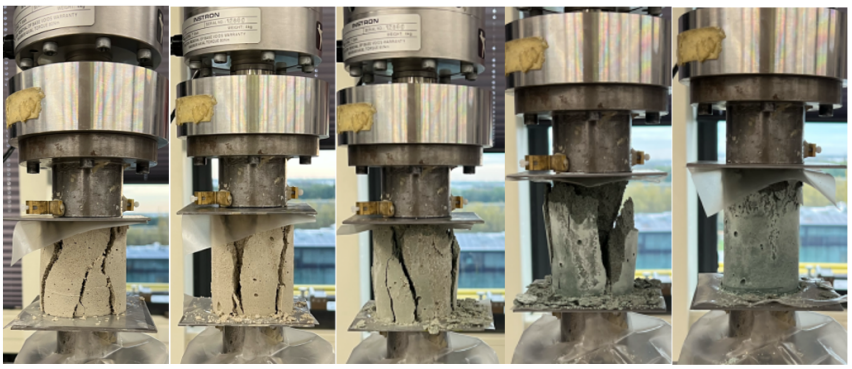

Figure 6.17: Mixture CC0S100-REF in the green strength test. Photographs of damaged samples at different ages.

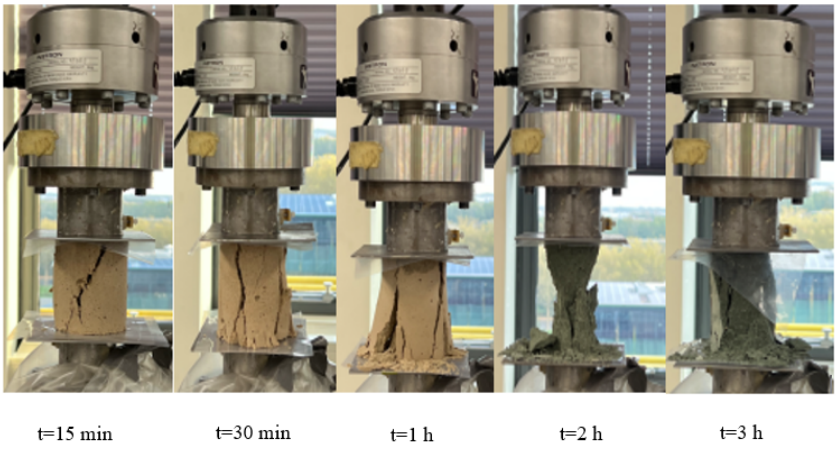

Figure 6.18: Mixture CC10S90 in the green strength test. Photographs of damaged samples at different ages.

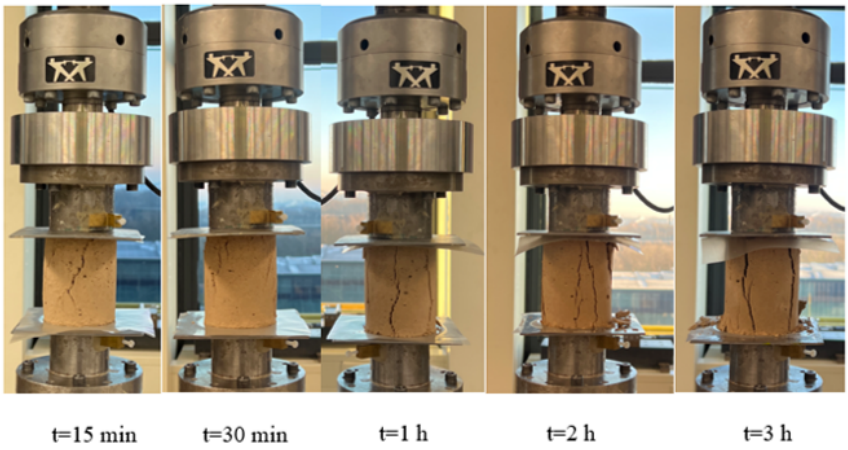

Figure 6.19: Mixture CC20S80 in the green strength test. Photographs of damaged samples at different ages.

6.2. Mechanical properties

6.2.1. Compressive strength

The compressive strength is monitored over time (1, 3, 7 days) to assess the influence of calcined clay on the strength development of a slag-based AAM.

The results show an improved 1-day, 3-day and 7-day compressive strength of the mixtures with 10% calcined clay compared to the reference mixture. The mixture with 20% calcined clay, CC20S80, shows lower 1-day strength and higher 3-day and 7-day strength than the reference mixture. Mixtures with 30% and 40% calcined clay content show zero strength development, even after 7 days. This observation was already done in the fast screening. For low-calcium binders, more aggressive working conditions are necessary for successful activation of the binder, i.e. elevated curing temperatures and a higher alkalinity of the activator solution. A high sodium oxide content in the binder is therefore a requisite to ensure strength development in the first couple of days after casting, in the case of alkali-activated materials with high calcined clay content.

Table 6.5: Compressive strength after 1, 3 and 7 days of curing. Mortar level.

Mixture	$\sigma_{c,1d}$ [MPa]	$\sigma_{c,3d}$ [MPa]	$\sigma_{c,7d}$ [MPa]
CC0S100-REF	12.82	16.08	23.47
CC10S90	21.27	26.15	35.58
CC20S80	4.44	22.77	42.97
CC30S70	0.00	0.90	1.29
CC40S60	0.00	0.00	0.00

In Fig. 6.20, the influence of calcined clay content on the compressive strength is illustrated after 1, 3 and 7 days of curing in ambient conditions. From the results follow that the mixture with 10% calcined clay has higher compressive strength at all curing ages compared to the reference mixture. Mixture CC20S80 shows the highest 7-day compressive strength, despite the low reactivity of calcined clay. The differences in pore structure and hydration will provide an explanation for this trend in mechanical properties.

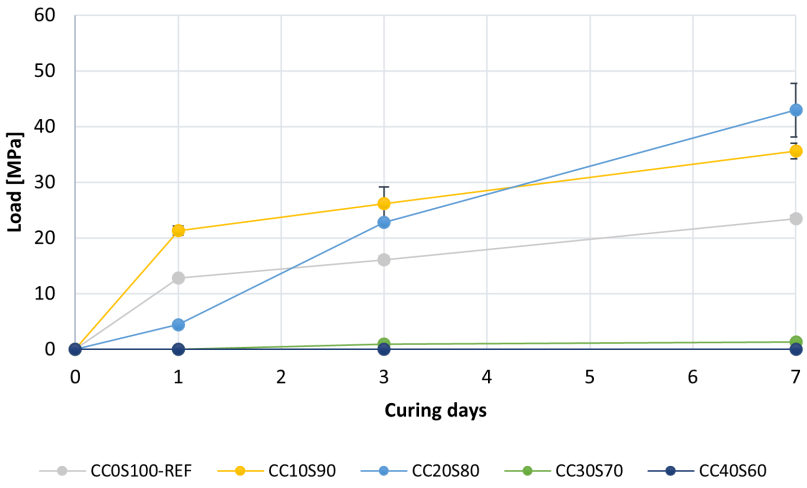

Figure 6.20: Compressive strength after 1, 3 and 7 days of curing. The standard deviation is depicted as well in the graph.

6.3. Hydration

6.3.1. Isothermal calorimetry

In this section, isothermal calorimetry test results of the different paste mixtures are presented. Isothermal calorimetry is commonly used to study hydration of cement pastes. The heat evolution can provide information on hydration kinetics, hydration reactions and strength development of cementitious materials.

The normalized heat flow as well as the cumulative heat by mass of paste for a time span of 7 days after casting are plotted in Fig. 6.21, Fig. 6.22, Fig. 6.23 and Fig. 6.24.

From Fig. 6.21 can be seen that the highest cumulative heat is obtained for the reference mixture CC0S100, containing only slag and zero calcined clay. With the increase of the calcined clay content, the cumulative heat decreases. This observation indicates a dilution effect on hydration caused by the higher calcined clay content. Based on these results, it is highly probable that calcined clay does not contribute to the chemical reaction at early ages and is acting as a filler in an alkali-activated system.

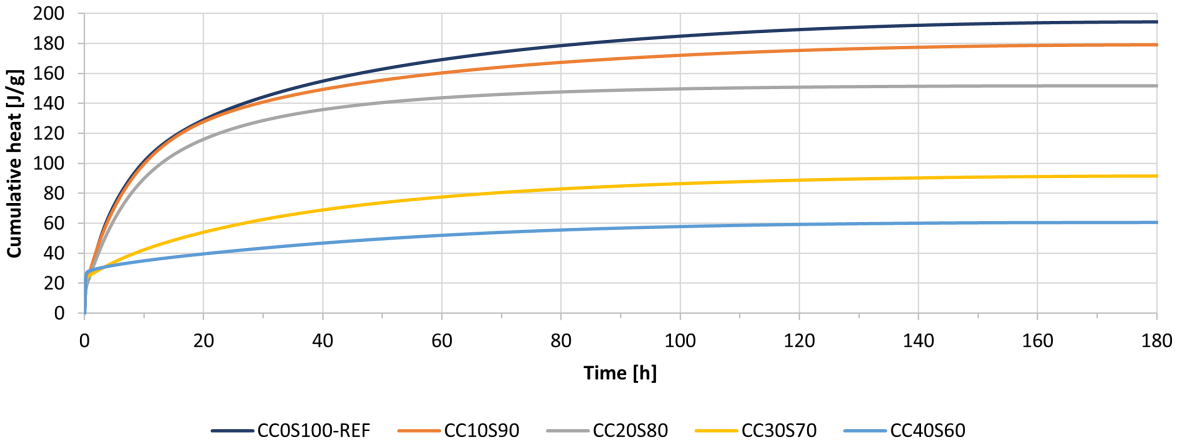

Figure 6.21: Cumulative heat flow by mass of paste with time (7 days).

Fig. 6.22, Fig. 6.23 and Fig. 6.24 illustrate the influence of calcined clay content on the normalized heat flow. An exothermic peak, e.g. the main hydration peak, immediately appears after mixing the activator with the solid material. This initial peak can be clearly seen in Fig. 6.23. This peak is designated as the wetting and dissolution of solid material *(Shi et al., 2006)*. The initial exothermic heat response increases for increasing calcined clay content, indicating an enhanced dissolution.

For mixtures CC30S70 and CC40S60, with 30 and 40% of calcined clay content, a single exothermic heat response is observed. The heat flow after dissolution is weak for these mixtures. For the remaining mixtures, two exothermic heat responses are observed. The first exothermic peak is followed by a short dormant period, after which the second exothermic peak appears. The dormant period is considered to be the time needed for the concentrations to increase in the pore solution*(Shi et al., 2006)*. After the concentrations of the dissolved ion species reach a threshold, the polymerization and condensation of geopolymeric gels will begin, hence resulting in a secondary exothermic peak. Precipitation of reaction products, such as C-A-S-H-gel and N-A-S-H-gel is reported to be responsible for the second exothermic peak *(Shi et al., 2006)*.

In Fig. 6.22 and Fig. 6.24, the normalized heat flow is plotted without the first exothermic peak to magnify the secondary heat response. From these figures can be seen that the peak value gradually decreases for increasing calcined clay content, supporting the idea that calcined clay only acts as a filler in an alkali-activated system.

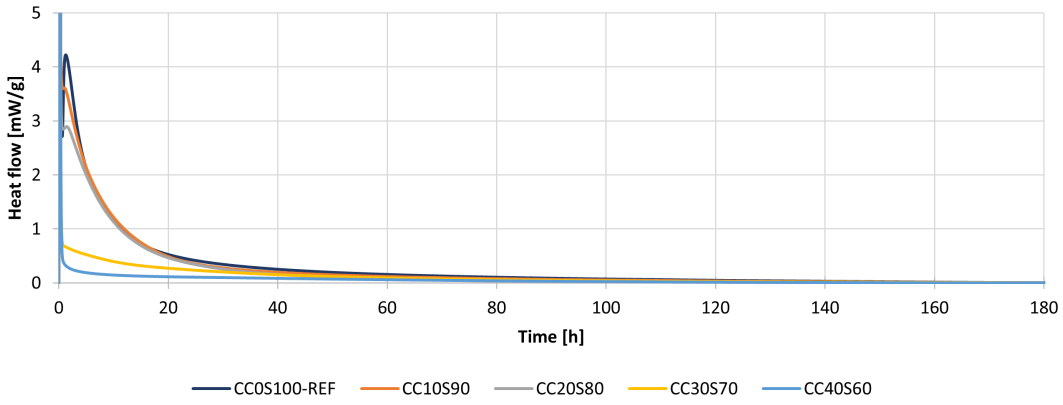

Figure 6.22: Normalized heat flow by mass of paste with time (7 days).

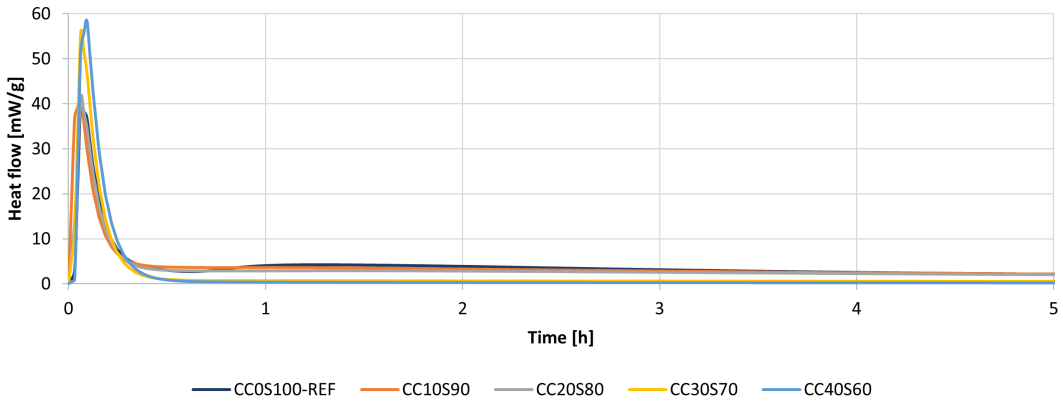

Figure 6.23: Normalized heat flow by mass of paste with time (first 5 h), including the first exothermic peak.

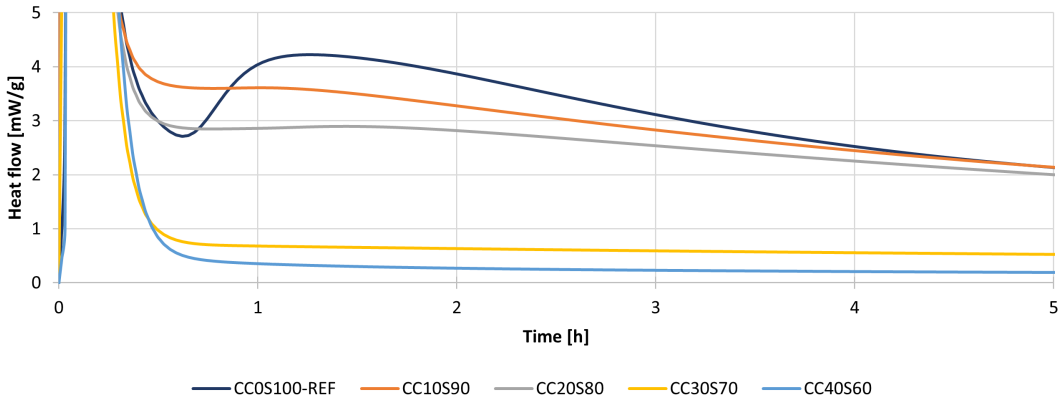

Figure 6.24: Normalized heat flow by mass of paste with time (first 5 h), excluding the first exothermic peak.

6.3.2. Thermogravimetric analysis (TGA) and differential thermogravimetric analysis (DTGA)

In order to investigate gel formation in alkali-activated calcined clay and slag based materials, thermogravimetric and differential thermogravimetric analysis is performed. Fig. 6.25 shows the thermogravimetric curves of the various mixtures.

Mass loss during heat treatment can be caused by water evaporation and dihydroxylation. Physical water (pore water) evaporates at 20-100 °C, while chemically bound water (gel water) evaporates at 100-300 °C. Hydroxyl groups typically evaporate at temperatures above 300 °C *(He et al., 2020)*. Therefore, mass loss between 40-700 °C is assigned to the combined dehydration and dihydroxylation effect of hydration products such as C-A-S-H- and/or N-A-S-H-gel, katoite, $Al(OH)_3$ and AFm phases.

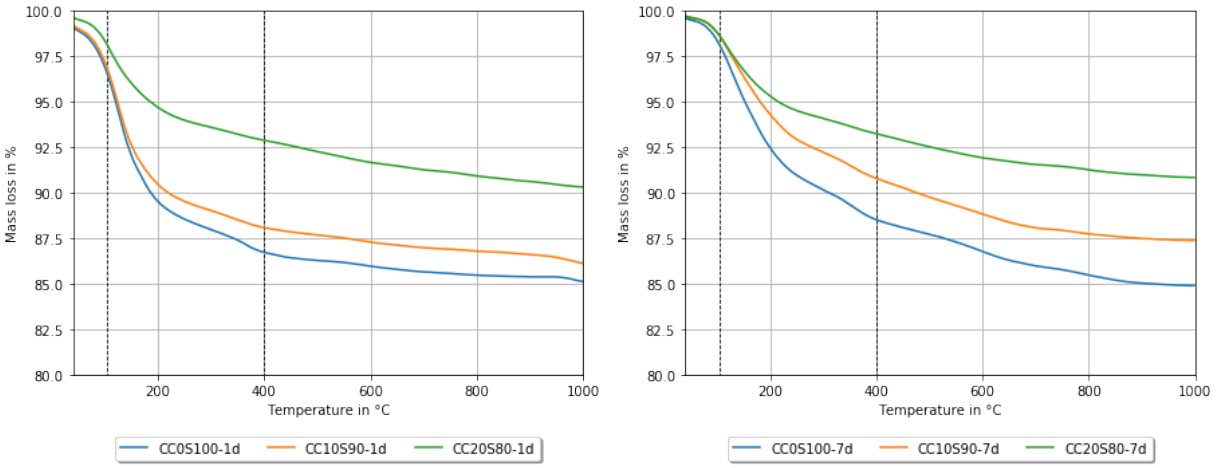

Figure 6.25: TGA-spectra of the alkali-activated pastes at 1 day and 7 days.

In the region of 800-1000 °C, low mass loss is detected (Fig. 6.25). This indicates that thermal decomposition stops at high temperatures. The majority of the weight loss is observed at temperatures below 400 °C for all of the mixtures. Based on this observation, it is likely that most of the mass loss is from interlayer and structurally bound water either in C-A-S-H- and/or N-A-S-H-gel.

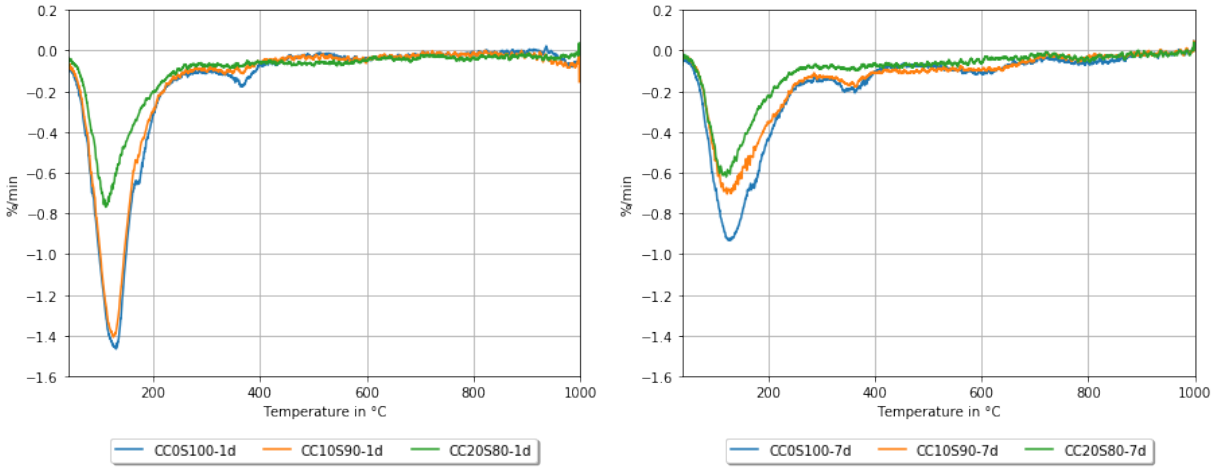

Figure 6.26: DTGA of the alkali-activated pastes at 1 day and 7 days.

Fig. 6.26 shows the differential thermogravimetric analyses of the various mixtures. Similar peaks are observed, centred at 100-150 °C, 350-400 °C and 600 °C. This suggests the formation of similar gel products. The first peak, centred at 100-150 °C, corresponds to the removal of hygroscopic (free) water.

The second peak, centred at 350-400 °C, is caused by removal of water molecules from either C-A-S-H- or N-A-S-H-gel, i.e. chemically bound water.

It is assumed that the mass loss within the temperature range of 105-400 °C is caused by dehydration of the amorphous gel phases. The mass loss in this temperature range is therefore taken as a measurement of the gel formation for the various alkali-activated pastes. In Table 6.6, the mass losses at 1 day and 7 days for the various pastes are given. From the table follows that the mass loss decreases for increasing calcined clay content, which suggests less gel formation for mixtures with higher calcined clay content. The reference mixture, CC0S100-REF, shows the highest mass loss and therefore the most gel formation of all the mixtures. This supports the idea that calcined clay does not effectively contribute to chemical reactions and is mostly acting as a filler instead in an alkali-activated system.

Table 6.6: Mass loss in alkali-activated pastes at 1 d and 7 d, in the temperature range of 105-400 °C.

Mixture	CC0S100-REF	CC10S90	CC20S80
Mass loss at 1d [%]	9,79	8,73	5,23
Mass loss at 7d [%]	9,60	7,81	5,40

6.3.3. BET-specific surface area (BET-SSA)

Measuring the evolution of the BET specific surface area can give an indication of the stiffness evolution of the material. Therefore, the SSAtotal is measured for each mixture at the material ages of 1 h and 3 h to understand the very early-age hydration. The BET-specific surface area is determined by physical adsorption of a gas, nitrogen gas in this case, onto the surface of the sample at cryogenic temperatures to quantify the specific surface area. The Brunauer–Emmett–Teller (BET) theory can be applied to systems of multilayer adsorption. Based on the applied vapor pressure, the specific surface area can be determined from the BET-theory.

In Fig. 6.27, the total specific surface area (SSA_{tot}) of the various samples is plotted at 1 h and 3 h after casting. From the figure can be seen that the SSA_{tot} is increasing over time for all mixtures. The increase in SSA_{tot} for all mixtures is a result of the formation of hydration product over time. Hydration products such as C-A-S-H-gel and/or N-A-S-H-gel are formed around the slag and calcined clay particles. As a result of crystal nucleation and growth of the hydrates, the specific surface area is increasing over time. The formation of hydration product is directly related to the loss in workability and the stiffness evolution of the various alkali-activated pastes, as water is consumed during hydration.

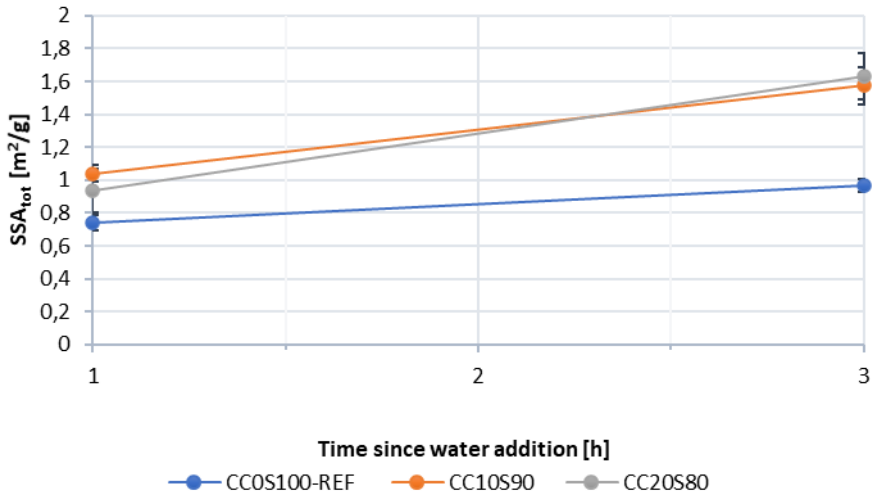

Figure 6.27: SSA_{tot} of different paste mixtures at the material ages of 1 h and 3 h.

Furthermore, there is a clear trend-line in growth rate of the SSA_{tot} from 1 h to 3 h (Fig. 6.29). An increasing calcined clay content in the precursor contributes to a higher growth rate of the SSA_{tot}. All mixtures show similar SSA_{tot} at the age of 1 h. The higher SSA_{tot} of the mixtures containing either 10% or 20% calcined clay after 1 h of curing, compared to the reference mixture, is attributed to the significantly higher specific surface area of calcined clay compared to blast furnace slag (Table 6.7). The higher growth rate for mixtures containing 10% and 20% calcined clay may indicate increased nucleation on calcined clay particles, as a result of the favorable surface structure. However, this still does not necessarily lead to higher very-early strength. If the layer of hydration product around the particles is not dense and uniformly distributed, the very-early strength will not be necessarily higher. This very-early strength is crucial in ensuring high buildability for successful 3D-printing. This concept is illustrated in Fig. 6.28. Two particles are depicted with a similar grain size, but a different specific surface area. The particle with the higher specific surface area (right) shows a a larger distribution of the hydration product around the perimeter, as a result of the more favorable structure. However, as the amorphous content of slag, i.e. the reactive part of the material, is higher than calcined clay, the density of the hydration product might be larger as well.

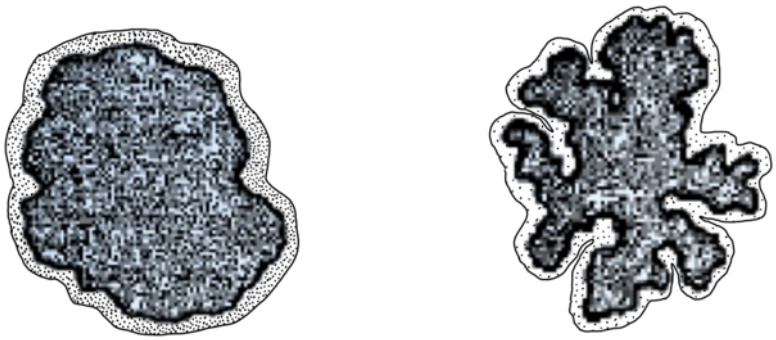

Figure 6.28: Left: formation of hydration product on a particle with a low SSA. Right: formation of hydration product on a particle with a high SSA.

From Table 6.7 follows that calcined clay is much more porous compared to blast furnace slag, as the total pore volume and average pore width, determined with BET, is much higher. Besides the more porous nature of calcined clay, the material also has a lower amorphous content than blast furnace slag. The green strength of the reference mixture in the first three hours after casting was higher compared to the mixtures containing 10 and 20% calcined clay. This supports the idea that hydration product around the slag particles are denser and more uniformly distributed at very-early ages.

Table 6.7: Characteristics of calcined clay and blast furnace slag, determined by BET.

Material	**BET-SSA [m^2/g]**	**Total pore volume [cm^2/g]**	**Average pore width [nm]**
CC	12.02	0.003722	1.24
BFS	1.44	0.000396	1.10

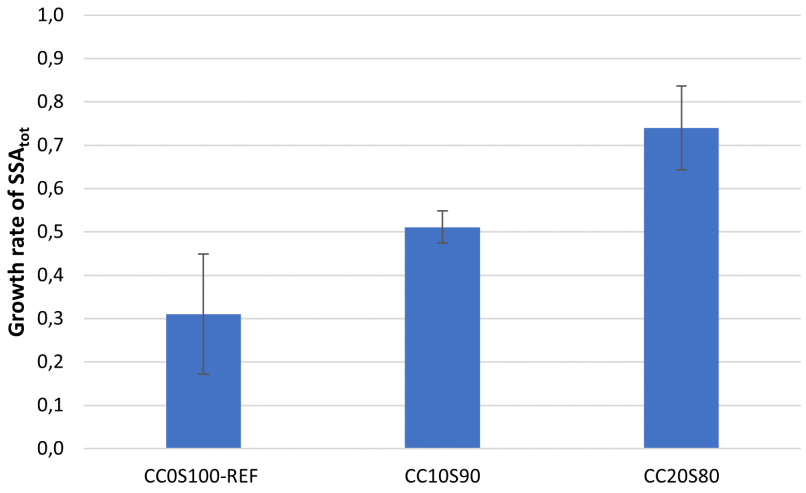

Figure 6.29: Growth rate of SSA_{tot} of the different paste mixtures, between 1 h and 3 h.

Note that this testing method has its limitations. The specific surface includes the surface of the particles as well as accessible open pores. A fraction of the pore space will always remain inaccessible to nitrogen and will therefore not be included in the calculations of the specific surface area. The impermeability is a result of the narrow ink-bottle pores that are inaccessible by N_2 *(Odler, 2003)*.

6.3.4. Mercury Intrusion Porosimetry (MIP)

The influence of the replacement level of calcined clay on the microstructure of alkali-activated calcined clay and slag based materials is verified by looking at the pore distribution. To determine the pore structure, Mercury Intrusion Porosimetry (MIP) is used. In Fig. 6.30 and Fig. 6.31, the differential and cumulative pore volumes for specimens containing various amounts of calcined clay after 1 day of curing are presented. In Fig. 6.32 and Fig. 6.33, the differential and cumulative pore volumes for AAM-pastes after 7 days of curing are presented.

In cementitious materials, pores can be classified into two main groups *(Mindess & Young, 1981)*:

- Gel pores **(I)**, with a pore size smaller than 10 nm.
- Capillary pores, with a pore size larger than 10 nm. Capillary pores can be subdivided into medium capillary pores **(II)** (10 nm < d < 50 nm) and large capillary pores **(III)** (50 nm < d < 10 μm) .

The classification for the pore sizes is also depicted in Fig. 6.30 and Fig. 6.32. The maximum size of the pores in the alkali-activated materials lies between 0.0076 μm and 100 μm. From the graphs representing the differential intrusion follows that the main peaks shift towards smaller pore sizes when the curing age increases. Over time, there is a clear shift to a finer pore structure. This means that the total amount of pores, i.e. total porosity, and the average pore diameter are larger at early ages and decrease over time as a result of continuous hydration.

The results show that incorporation of calcined clay may contribute to pore refinement of slag based AAMs. Table 6.8 shows that the average pore diameter decreases for increasing calcined clay content in the precursor after 1 day of curing. The largest pore diameter is found for the reference mixture. There is no clear relation between calcined clay content and total porosity for the samples after 1 day of curing. Mixture CC20S80 shows the lowest porosity and most refined pore structure, while mixture CC10S90 has the highest porosity. From Fig. 6.30 can be seen that CC10S90 has the largest amount of large capillary pores (area **III**). The increased amount of large capillary pores contributes significantly to the total porosity, which explains why the total porosity is the highest for CC10S90. From the same figure follows that the reference mixture, CC0S100-REF, has the largest amount of medium capillary pores (area **II**).

Table 6.8: Total pore area, average pore diameter and porosity of AAMs with various calcined clay contents after 1 day curing.

Sample	Average pore diameter [nm]	Total porosity [%]	Total pore surface area [m^2/g]
CC0S100-REF	29.65	10.05	6.81
CC10S90	25.06	10.08	8.17
CC20S80	19.07	9.76	10.29

A similar relation between average pore diameter and calcined clay content is found for calcined clay and slag based AAMs after 7 days of curing. The average pore diameter and total porosity clearly decrease for increasing calcined clay content, as can be seen from Table 6.9. Mixtures with 10 and 20% calcined clay have a more refined pore structure than the reference mixture. This can also clearly be seen from Fig. 6.32. The reference mixture has the most medium capillary pores (area **II**), while mixtures with 10 and 20% calcined clay show an increased amount of gel pores (area **I**). According to *Jeon et al. (2015)*, there is an inverse-proportional relationship between the average pore diameter and the compressive strength. A decrease in average pore diameter will therefore directly result in an increased compressive strength. According to *Hu et al. (2019)*, there is also an inverse-proportional relation between the total porosity and the compressive strength. A decrease in porosity therefore contributes to an increase in compressive strength. The same trend-line is found in this study as well: an increased compressive strength for increasing calcined clay content after 7 days of curing, which might be the result of smaller pores and a lower total porosity.

Furthermore, from Table 6.8 and Table 6.9 can be seen that the total pore surface area increases for increasing calcined clay content. The increased pore surface area for increasing calcined clay content is probably a result of the increased amount of gel pores. The increased amount of gel pores for increasing calcined clay content can be clearly seen in area **I** of Fig. 6.32. An increase in amount of gel pores does not result in mechanical strength reductions *(Jeon et al., 2015)*.

Table 6.9: Total pore area, average pore diameter and porosity of AAMs with various calcined clay contents after 7 days curing.

Sample	Average pore diameter [nm]	Total porosity [%]	Total pore surface area [m^2/g]
CC0S100-REF	25.11	10.01	8.31
CC10S90	21.57	9.58	9.21
CC20S80	16.99	9.20	11.10

Although the average pore diameter and total porosity of mixture CC20S80 after 1 day of curing is higher than the reference mixture and mixture CC10S90 (Table 6.8), mixture CC20S80 still shows the lowest compressive strength. The pore structure is one way to describe the trend in mechanical properties. However, other factors, such as gel formation and the type and structure of the reaction product that is formed, might also influence strength properties. The reference mixture only contains blast furnace slag in the precursor and therefore only C-A-S-H-gel is formed. In a hybrid alkaline binder, consisting out of calcined clay and blast furnace, an aluminosilicate source is added, which might change the type and structure of the reaction product. Furthermore, as a result of the low calcium oxide content present in calcined clay, the formation of reaction product is delayed at early-ages (1-day), which may also be governing the strength properties.

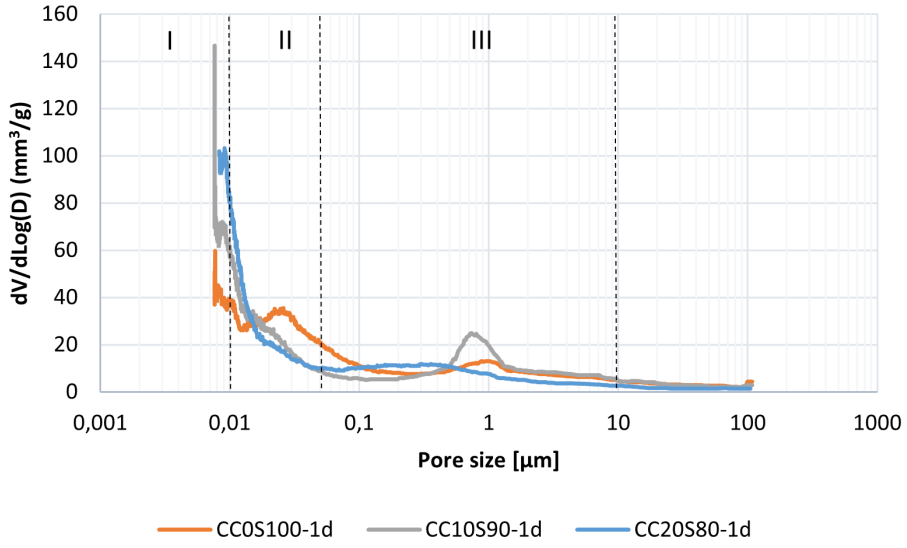

Figure 6.30: MIP - differential intrusion after 1 day of curing (pore size distribution).

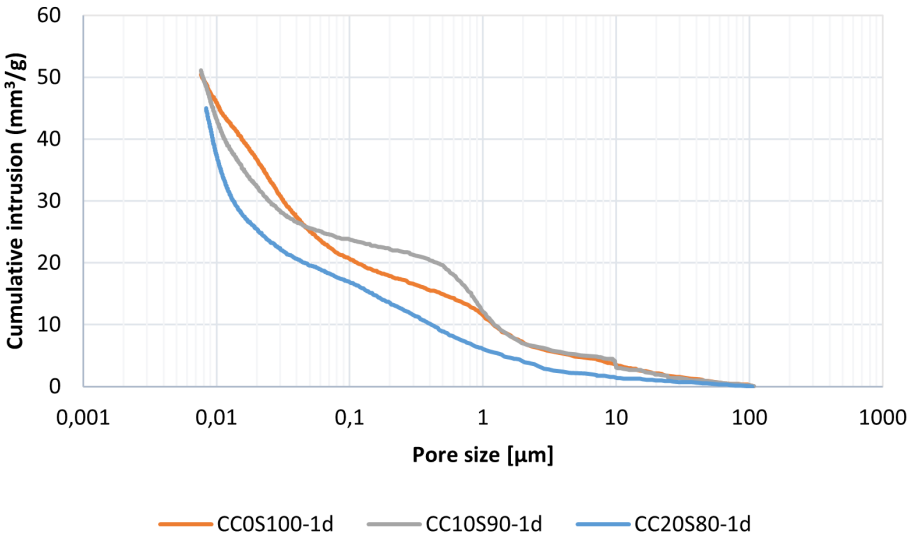

Figure 6.31: MIP - cumulative intrusion of mercury after 1 day of curing.

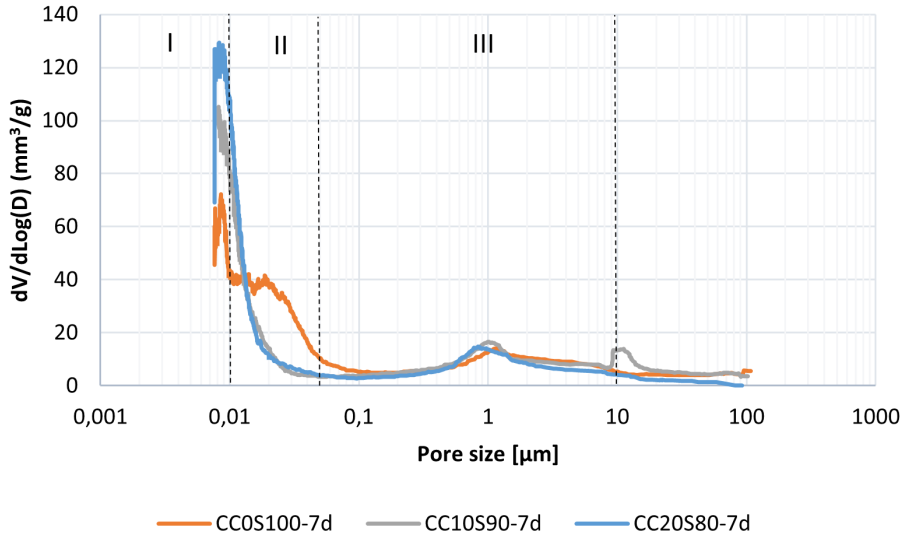

Figure 6.32: MIP - differential intrusion after 7 days of curing (pore size distribution).

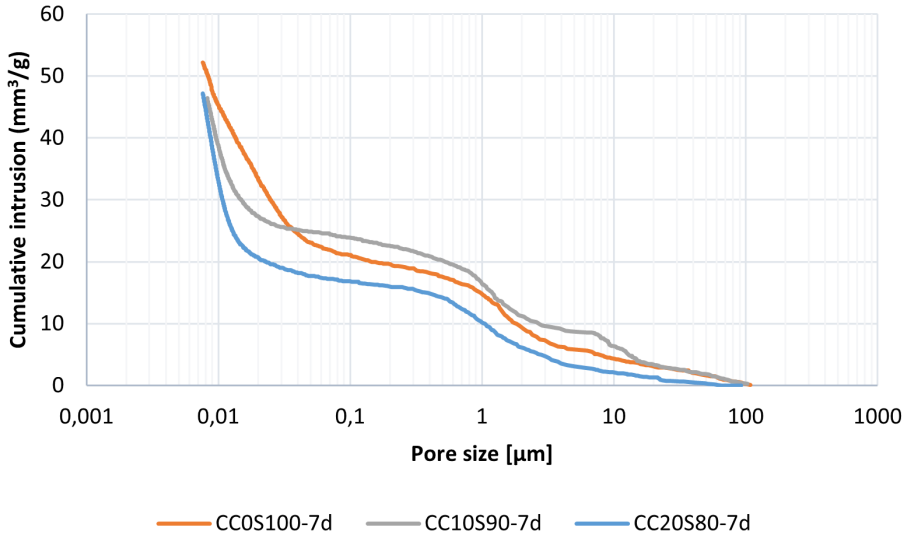

Figure 6.33: MIP - cumulative intrusion of mercury after 7 days of curing.

It is generally known that MIP fails to include complex-shaped pores in the analysis. This is denoted as the 'ink bottle'-effect in literature. Large pores can be misrepresented by their narrow throats. Only the open pores are correctly measured in this technique and therefore, the total volume of mercury that intrudes the bulk density of the material is related to the open porosity *(Cook & Hover, 1999)*. Note that porosity obtained by MIP might be smaller than the actual porosity of the sample, if the pores are too small or isolated to be intruded by mercury.

Packing density of the various mixtures

Many researchers have tried to find the ideal grading curve for concrete mixtures, as the grain size of the aggregates and binding materials influences the properties considerably. An important researcher is Fuller, who designed the Fuller-curve *(Fuller & Thompson, 1907)*. The curve is described by eq. 6.2 with q = 0.5. In this model, only the upper limit of the grain size is taken into account and a parameter to adjust for fineness or coarseness (q). Many researchers have tried to improve this model. *Funk & Dinger (1980)*

have adjusted the model in such a way that also the lower limit of the grain size is taken into account (d_{min}). In the model of *Funk & Dinger*, the maximum and minimum grain size is taken into account to represent the real size distribution. The improved model is described by eq. 6.3, with q = 0.37.

$$P(d) = (\frac{d}{d_{max}})^q \tag{6.2}$$

6.2: Equation for the fuller curve *(Fuller & Thompson, 1907)*.

$$P(d) = \frac{d^q - d_{min}^q}{d_{max}^q - d_{min}^q} \tag{6.3}$$

6.3: Equation for the improved particle distribution curve *(Funk & Dinger, 1980)*.

With:
P(d) = size cumulative distribution function [-]
d = particle diameter being considered [m]
d_{min} = minimum particle diameter in the mixture [m]
d_{max} = maximum particle diameter in the mixture [m]
q = parameter, to adjust the curve for fineness or coarseness [-]

By using particle packing models, the packing density of the various mixtures with different calcined clay contents can be determined. By using the ideal grading curve of the binder and fine aggregate, the influence of calcined clay on the packing of calcined clay and slag based AAMs can be determined.

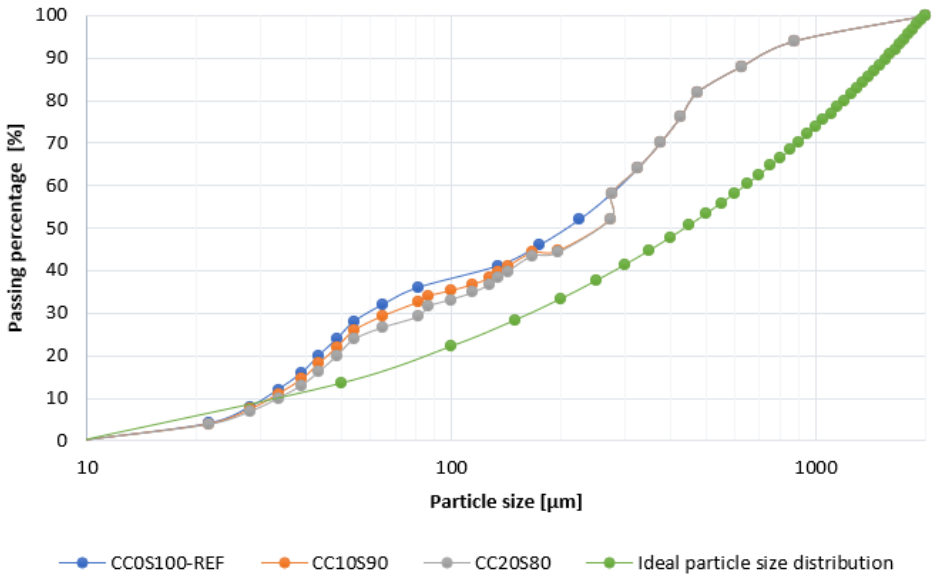

Figure 6.34: Particle size distribution of the various mixtures and the ideal particle size distribution *(Funk & Dinger, 1980)*.

From Fig. 6.34 can be seen that addition of calcined clay improves the packing of AAMs and therefore also the performance of the material. The curves of binary binders with calcined clay and slag approach the ideal curve better, determined from eq. 6.3. The improved grading of the mixtures ensures that more voids are filled, which in turn contributes to an improved pore structure. An improved pore structure can result in better mechanical properties, lower shrinkage and better workability. This therefore explains the refined pore structure for AAMs with increasing calcined clay content, as seen from the MIP-results.

6.4. Shrinkage

As shrinkage-induced cracking is one of the main problems related to large-scale production of alkali-activated materials, it is considered in this study to assess the potential of calcined clay and slag-based AAMs. Two types of shrinkage were monitored in this study for a duration of 28 days:

- *Autogenous shrinkage*: volume change occurring without any moisture exchange with the environment. It is a result of internal reactions within the mortar during hydration.
- *Drying shrinkage*: volume change under the combined effects of moisture exchange with the environment and internal reactions within the mortar during hydration. Mechanisms of autogenous and drying shrinkage are similar, as they are both related to an internal drop in relative humidity.

The autogenous and drying shrinkage of mixtures CC0S100-REF, CC10S90 and CC20S80 are presented in Fig. 6.35 and Fig. 6.36. The autogenous shrinkage measurements start after demoulding, i.e. 1 day after casting. The measurements for the drying shrinkage start immediately after the samples are unsealed, after 7 days of curing in sealed conditions.

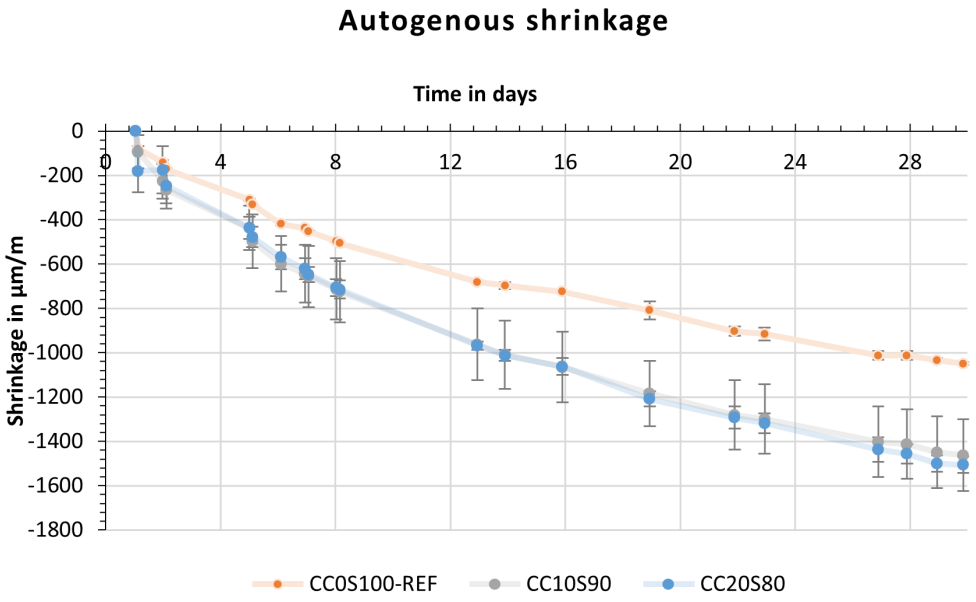

Figure 6.35: Autogenous shrinkage of the various samples during 28 days. The standard deviation is depicted as well in the graph.

From Fig. 6.35 follows that the autogenous shrinkage increases for increasing calcined clay content in the precursor. The highest autogenous shrinkage is measured for mixture CC20S80. Increasing the calcined clay content in an alkali-activated material does not benefit the autogenous shrinkage. Autogenous shrinkage is highly influenced by the ongoing hydration process and therefore the formation of hydration product. Thermogravimetric analysis and isothermal calorimetry have confirmed that the reference mixture has the most gel formation and reactivity: the highest mass loss in the temperature range of 105-400°C and the highest cumulative heat over a time span of 7 days.

In this study, the increased autogenous shrinkage is attributed to the finer pore structure when calcined clay is introduced in an alkali-activated material, as has been confirmed by MIP. As a result of ongoing hydration, radii of the menisci generally decrease over time, hence resulting in an increase in autogenous shrinkage. A denser pore structure can also contribute to a smaller radius of the menisci formed within the paste *(Li et al., 2020)*. The relation between pore pressure and radius of the meniscus is described with the Laplace equation, in eq. 6.4. A smaller radius of the menisci can eventually lead to higher capillary pressure in the pores and therefore higher shrinkage. A schematic representation of capillary pore pressure is provided in Fig. 6.37.

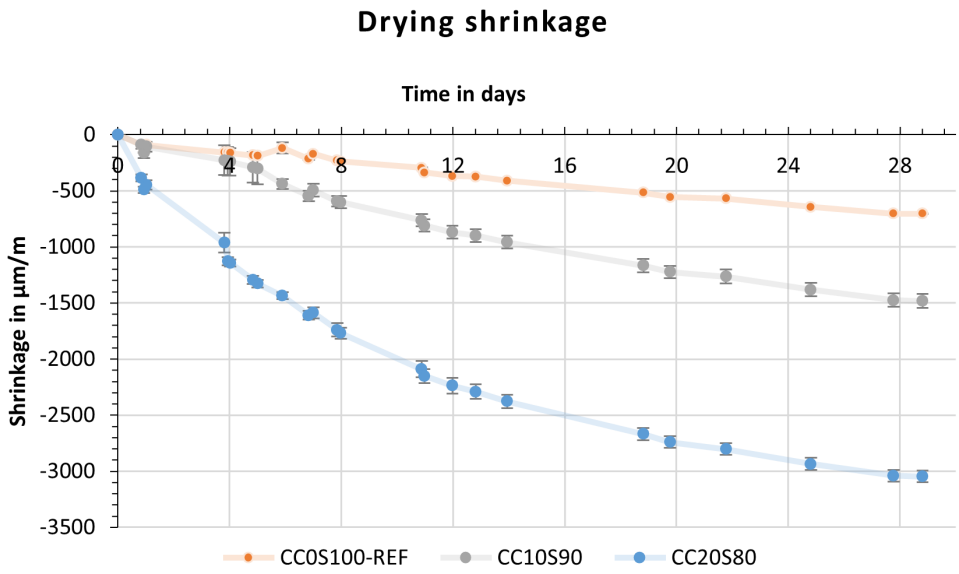

Figure 6.36: Drying shrinkage of the various samples during 28 days, exposed at 7 days. The standard deviation is depicted as well in the graph.

$$\sigma = -\frac{2\gamma}{r} \tag{6.4}$$

6.4: Laplace equation.

With:
σ = the pore pressure (MPa)
γ = the surface tension of the pore solution (N/m)
r = the radius of the menisci (m)

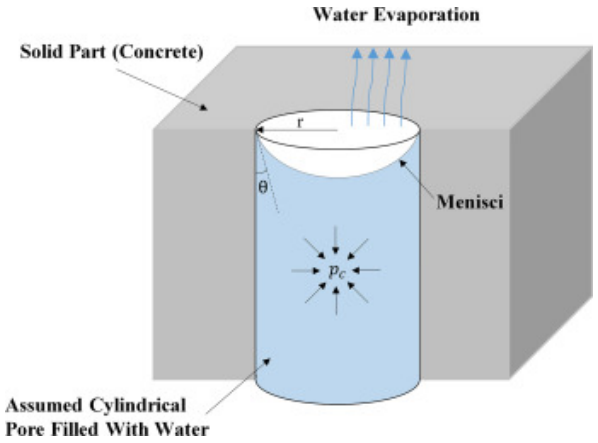

Figure 6.37: A schematic representation of capillary pressure in AAMs due to formation of menisci. *(Jamali et al., 2022)*.

From Fig. 6.36 follows that drying shrinkage increases for increasing calcined clay content. Note that no visible cracks were observed on the surface of the samples. This effect might be the result of the pore-refining effect of calcined clay particles. MIP-results have shown that mixtures containing more calcined clay have a lower average pore diameter and a finer pore structure. Substitution rate of blast

furnace slag by calcined clay is therefore positively correlated with drying shrinkage. Increasing the calcined clay content in AAMs does not benefit the drying shrinkage. In the study of *Ye et al. (2017)*, similar results regarding the pore structure and amount of drying shrinkageare found. In this study, drying shrinkage of AAM and OPC-based materials are compared by focusing on the pore structure. AAMs show a more refined pore structure than OPC, while the drying shrinkage is considerably larger as well. In the study, it is concluded that this may be the result of more loosely bound water. *Collings & Sanjayan (2000)* have conducted a similar study. Alkali-activated materials show a finer pore size distribution compared to OPC-based materials. As the pores are generally smaller in AAMs, drying of water from smaller pores can result in higher capillary forces set up at the meniscus, i.e. the interface between water and air. This can ultimately result in higher drying shrinkage. In the study of *Collings & Sanjayan*, weight-loss is also monitored to link the moisture loss to drying shrinkage of AAMs and OPC-based materials. AAMs show much less weight loss and much higher drying shrinkage than OPC-paste. This confirms the idea that the refined pore structure of AAMs is responsible for the increased drying shrinkage.

The same applies to alkali-activated slag and calcined clay. Incorporating more calcined clay in the binder directly results in a finer pore structure, hence a smaller radius of the menisci, a higher pore pressure and therefore increased drying shrinkage.

The target value for the drying shrinkage was set at 1000 microstrain. The drying shrinkage found for alkali-activated calcined clay and slag based materials with 10% and 20% calcined clay is well above the target value after 28 days. The mixture with 10% calcined clay, CC10S90, shows shrinkage of 1480 microstrain after 28 days, while mixture CC20S80 shows a drying shrinkage of approximately 3000 microstrain, which is almost four times the target value. This would mean that this material is not suitable for applications in 3D-printing, as the material will crack very rapidly in restrained conditions when exposed to the environment.

Part III

Conclusion and recommendations

7

Conclusion

In this thesis, the focus is placed on the following two research questions:

> *Research question 1: What is the influence of calcined clay content on fresh properties, mechanical properties, hydration and shrinkage behaviour of calcined clay and slag-based AAMs?*
>
> *Research question 2: To what extent is calcined clay and slag based AAM interesting for use in 3DCP?*

In this chapter, the answers to the research questions will be presented into two parts. The chapter is finished with the final conclusion of the study.

7.1. Influence of calcined clay on properties of AAMs

The influence of calcined clay on the fresh properties, mechanical properties, hydration and shrinkage of an calcined clay and slag-based alkali-activated material is discussed in Table 7.1.

Table 7.1: The influence of calcined clay content on properties of AAMs.

Fresh properties	
Workability	Partial replacement of slag by calcined clay does not influence the slump and slump-flow of the mixtures. No clear trend-line is found. However, the consistency and shape stability of calcined clay and slag based AAMs is clearly improved with addition of calcined clay to the binder as a result of the decelerated setting.
Setting time	The results show that an increasing calcined clay content decelerates the setting of an alkali-activated calcined clay and slag based material. Calcined clay has a much lower CaO content, lower amorphous content and therefore a lower reactivity compared to blast furnace slag, which results in a delayed setting.
Rheology	The incorporation of calcined clay in a slag-based AAM directly contributes to a higher static and dynamic yield stress. Furthermore, all mixtures show shear-thinning behaviour: a decreasing viscosity for increasing shear rate. Because of the larger specific surface area and larger total pore area of calcined clay compared to blast furnace slag, more water is adsorbed onto the surface of calcined clay particles and absorbed into the open pores, therefore reducing the effective water to binder ratio and improving the very-early rheological behaviour of alkali-activated pastes.
Structural build-up	From the SAOS-test follows that the initial storage modulus in the very-early stage increases when 10% and 20% of calcined clay is incorporated into the binder. This may indicate an enhanced structural formation in the very-early stages, induced by inter-particle interaction forces. This observation is in line with the results from the flow curve test of calcined clay and slag based AAMs, in which an increasing static and dynamic yield stress is observed for mixtures with increasing calcined clay content.

Green strength	Incorporating calcined clay in AAMs does not benefit the early-age strength. The fastest green strength evolution is found for the reference mixture. Note that all mixtures show a green strength after 30 minutes that is higher than the target value.
Mechanical properties	
Compressive strength	The compressive strength is improved at the material ages of 1 day, 3 days and 7 days when calcined clay is incorporated into a slag-based alkali-activated binder. Mixtures with 30% and 40% calcined clay content show zero strength development, even after 7 days. A high sodium oxide content in the binder is a requisite to ensure strength development in the first couple of days after casting. From the results follows that the mixture with 10% calcined clay has optimal compressive strength at all curing ages, with enhanced compressive strength at all curing ages compared to the reference mixture containing only slag.
Hydration properties	
Isothermal calorimetry	With the increase of the calcined clay content in the binder, the cumulative heat and the peak value of the normalized heat flow decreases. This observation indicates a dilution effect on hydration caused by the higher calcined clay content. Based on these results, it is highly probable that calcined clay does not contribute to the chemical reaction at early ages and is acting as a filler in an alkali-activated system.
TGA	Total mass loss in the region of 105-400°C, caused by dehydration of C-A-S-H- and/or N-A-S-H-gel, decreases for increasing calcined clay content, which indicates less gel formation for mixtures with higher calcined clay content. The reference mixture, CC0S100-REF, shows the highest mass loss and therefore the most gel formation of all the mixtures. Similar peaks are observed in the DTGA-plots, which indicates the formation of similar gel products in the various mixtures after 1 day and 7 days of curing. This supports the idea that calcined clay does not contribute to chemical reaction, acting as a filler instead.
BET-SSA	An increasing calcined clay content in the precursor contributes to a higher growth rate of the total specific surface area in the first three hours of curing. This may indicate increased nucleation on calcined clay particles, as a result of the favorable surface structure. However, this still does not necessarily lead to higher very-early strength. If the layer of hydration product around the particles is not dense and uniformly distributed, the very-early strength will not be necessarily higher.
MIP	The results show that incorporation of calcined clay contributes to pore refinement of slag based AAMs. For 1 day and 7 days of curing, the average pore diameter and total porosity decrease for increasing calcined clay content.
Shrinkage	
Autogenous shrinkage	Autogenous shrinkage increases for increasing calcined clay content. Pore refinement is probably the reason for the increase in shrinkage. As the pores are smaller for mixtures containing calcined clay, drying of water from smaller pores can result in higher capillary forces set up at the meniscus and therefore a higher pore pressure. The increase in pore pressure is a driving mechanism for autogenous shrinkage.
Drying shrinkage	Drying shrinkage increases for increasing calcined clay content. The explanation for the increased drying shrinkage is similar to the one given for autogenous shrinkage.

7.2. Assessment of potential in 3DCP

The following key aspects are highlighted in literature to ensure successful 3D-printing of concrete:

- *High yield stress after extrusion. The yield stress is an important factor to ensure buildability and shape stability of the 3D-printed material after extrusion. A high yield stress ensures limited deformation under the self-weight of the printed material*.

The flow test shows that the static yield stress, the dynamic yield stress and the viscosity, immediately after extrusion, are increasing for increasing calcined clay content, compared to the reference mixture. This is

beneficial for the shape stability of the printed material under self-weight immediately after extrusion. The target value of the dynamic yield stress is chosen in the range of 150-500 Pa for extrudable and printable pastes. All mixtures (CC0S100, CC10S90, CC20S80) exhibit a dynamic yield stress in the targeted range, meaning that these mixtures are all likely to be successfully printed.

- *Shear-thinning behaviour, i.e. the structure is gradually broken down at a constant shear rate. This property ensures continuity during pumping and prevent blockage of the pump.*

Based on the flow test can be concluded that all mixtures show shear-thinning behaviour, regardless of the calcined clay content.

- *Fast recovery in strength after extrusion. The material regains its strength rapidly after extrusion. This property is related to the structural build-up of the material after extrusion and is crucial for good buildability.*

To ensure high buildability, a fast recovery of the material after extrusion is needed, meaning that the material needs to regain its strength rapidly. This property can be assessed by focusing on the structural build-up (storage modulus) and green strength evolution of the material. The structural build-up is determined at paste level by using a rheometer, while the green strength is determined at mortar level. At paste level, the influence of aggregates on strength and stiffness development is ignored.

From the structural build-up test follows that the initial storage modulus (time zero) increases when 10% and 20% of calcined clay is incorporated into the binder. From the SAOS-test follows that mixture CC20S80 has the best structural build-up within the first 15 minutes after casting, while mixture CC10S90 shows the best overall structural build-up in 1 h. Note that the storage modulus provides information about the stiffness of the materials.

This study has also shown that incorporation of calcined clay in AAMs (mortar level) does not benefit the green strength evolution. The green strength decreases considerably for increasing calcined clay to slag ratios. Although the green strength decreases for increasing calcined clay content in the precursor, this also means that extrusion is positively affected by addition of calcined clay. As a result of the decelerated setting, the printability window will increase and less pressure is needed for extrusion of the material. Note that the compressive strength at later ages (1, 3 and 7 days) is actually improved when calcined clay is included in the binder. The green strength of the weakest sample (CC20S80) is still higher than the target value after 30 minutes.

- *Long initial setting time to ensure continuity during printing. A short setting time ultimately means that the material is rapidly gaining strength and buildability, but adhesion between layers (interlayer bond strength), workability and pumpability may decrease.*

A delayed setting is observed for the mixtures with calcined clay. An increase of the calcined clay to slag ratio directly results in a longer setting time and therefore also better workability for an extended time and higher pumpability. A delayed setting is beneficial for the adhesion between layers, i.e. interlayer bonding. However, if the setting time is too long, this may hinder the buildability of the material.

- *Limited drying shrinkage when exposed to the environment. 3D-printed materials generally show increased shrinkage when compared to conventional concrete. 3D-printed AAMs show even higher drying shrinkage compared to OPC-based materials. Controlling the shrinkage is crucial in ensuring that the 3D-printed structure reaches its desired service life time.*

From the results follow that autogenous and drying shrinkage increase for increasing calcined clay content in the precursor. The incorporation of calcined clay therefore does not benefit the shrinkage of AAMs. The target value for the drying shrinkage was set at 813 microstrain.

The drying shrinkage found for alkali-activated calcined clay and slag based materials with 10% and 20% calcined clay is well above the target value after 28 days. The mixture with 10% calcined clay, CC10S90, shows shrinkage of 1480 microstrain after 28 days, while mixture CC20S80 shows a drying shrinkage of approximately 3000 microstrain, which is almost four times the target value. This would mean that this material is not suitable for applications in 3D-printing, as the material will crack very rapidly in restrained conditions when exposed to the environment.

Table 7.2: Target values in this study.

Property	Target value	Observed value
Workability	*Tay et al. (2019)* recommends a slump value in the range of 4-8 mm and a spread diameter in the range of 150-190 mm for optimal printing quality and buildability.	The values of the slump are slightly larger than the target value (approximately 10 mm), while the spread diameters of the various mixtures are almost all within the range of the target value (175-195 mm). All mixtures show excellent shape stability after the cone is lifted.
Setting time	The target value for the setting time is chosen in the range of 60-90 minutes.	The reference mixture CC0S100 and mixture CC10S90 show too fast setting, below the target value. Mixture CC20S80 shows too slow setting. None of the mixtures show a setting time in the targeted range.
Rheology	The target value of the dynamic yield stress is based on recommendations of *Alghamdi et al. (2019)* & *Nair et al. (2019)*: a dynamic yield stress in the range of 150-500 Pa for extrudable and printable pastes.	All mixtures exhibit a dynamic yield stress in the targeted range, meaning that these mixtures (CC0S100, CC10S90, CC20S80) are likely to be successfully printed.
Green strength	The green strength should be at least 44 kPa after 30 minutes for optimal buildability.	All mixtures show excellent green strength evolution within the range of the target value. The green strength exceeds 44 kPa after 30 minutes for all the mixtures. Buildability will therefore not be an issue for the chosen mixtures.
Shrinkage	Drying shrinkage should be smaller than 813 microstrain after 28 days.	The drying shrinkage found for alkali-activated calcined clay and slag based materials is well above the target value. This suggests that calcined clay and slag-based AAMs are not suitable for applications in 3D-printing.

7.3. Final conclusion

All in all, it can be concluded that the use of calcined clay and slag based AAMs is ineffective for 3D-printing applications. Although the mixtures with calcined clay show good rheology, green strength evolution, workability and mechanical properties, drying shrinkage and setting might still be a big issue. The mixture with 20% calcined clay shows a drying shrinkage that is four times larger than the target value. In general, AAMs already show a drying shrinkage that is much larger than OPC-based cementitious materials. Introducing calcined clay into an AAM might even further increase the total drying shrinkage. As of now, it is not recommended to use this material for 3D-printing applications. Introducing admixtures might help in solving these problems, so that an application in 3DCP can be possible in the future to account for the lower supply of fly ash and blast furnace slag.

Regarding the role of calcined clay in an alkali-activated system: it is highly probable that calcined clay mostly acts as a filler at early-ages in an alkali-activated system, hence the pore refinement, and barely contributes to gel formation. If it does contribute to gel formation, the gel is probably very porous and inhomogeneous.

There is still a lot of research that needs to be conducted to further improve the mixture designs. Admixtures and additives need to be introduced to further optimize the properties for an actual application in 3DCP. Problems related to shrinkage and fast setting need to be solved to ensure that the proposed

mixture can be actually used in the industry. Furthermore, the use of this type of calcined clay is only recommended in small quantities (<20% in mass of the binder) for optimal performance. If the goal is to have a higher replacement of slag by calcined clay, the alkali-activator needs to be adjusted accordingly. The use of a stronger, more concentrated alkali activator is key in promoting more gel formation by calcined clay. Furthermore, more research is needed to properly describe the influence of calcined clay on reaction kinetics of AAMs. This study will provide a proper basis for further research.

8

Recommendations

This research answers questions related to the influence of calcined clay content on properties of AAMs and the potential of using this material for 3D-printing applications. There is still plenty of research that can be performed to further explore the material behaviour of calcined clay and slag based AAMs and its potential for use in 3DCP. For this reason, the recommendations for future research are as follows:

- The range of the mix design parameters is limited in this research. It is recommended to expand the array for a better selection of promising mixtures.
- More elaborate research can be conducted on microscale. This research provides a general understanding of the microstructure. It is recommended to perform an air void analysis with a CT-scan and a SEM-analysis to analyse the different phases present in the various samples.
- Characterization of the pore solution composition with ICP-OES can shed more light on reactions kinetics of calcined clay and slag based AAMs.
- In further research, it is important to take the influence of the grading of the fine aggregate into account, as well as the influence of different grades of calcined clay (low and high grade). This research only focuses on one type of calcined clay, with high amorphous content, and one type of grading for the fine aggregate.
- To ensure higher replacement ratios of slag by calcined clay, it is recommended to use a calcined clay with higher metakaolin content to increase the reactivity of the binder. In this study, the best properties are obtained for mixtures containing less than 20% calcined clay. Another option for increasing the reactivity of calcined clay is adding calcium hydroxide powder to the binder. Calcium hydroxide will accelerate the reactivity of calcined clay, thus enhancing the very-early strength development.
- To reduce shrinkage, improve durability and strength of 3D-printed materials, it is recommended to consider aggregates larger than 2 mm. The shrinkage can also be further reduced by keeping the total water content in the mixtures as low as possible. Addition of superplasticizers might help in further reducing the water to binder ratio, while maintaining the same workability.
- It is recommended to introduce additives and/or admixtures in further research to finetune the mixtures for 3DCP-applications or for other applications.

9

Bibliography

Ahmed, Z., Wolfs, R., Bos, F., Salet, T. (2022). A Framework for Large-Scale Structural Applications of 3D Printed Concrete: the Case of a 29 m Bridge in the Netherlands. Open Conference Proceedings, 1, 5–19. https://doi.org/10.52825/ocp.v1i.74

Alanazi, H., Yang, M., Zhang, D., Gao, Z. J. (2017). Early strength and durability of metakaolin-based geopolymer concrete. Magazine of Concrete Research, 69(1), 46–54. https://doi.org/10.1680/jmacr.16.00118

Albidah, A., Alghannam, M., Abbas, H., Almusallam, T., Al-Salloum, Y. (2021). Characteristics of metakaolin-based geopolymer concrete for different mix design parameters. Journal of Materials Research and Technology, 10, 84–98. https://doi.org/10.1016/j.jmrt.2020.11.104

Aldin, Z. (2019). 3D printing of geopolymer concrete. TU Delft.

Alegbe, J., Ayanda, O. S., Ndungu, P., Alexander, N., Fatoba, O. O., Petrik, L. F. (2018). Chemical, Mineralogical and Morphological Investigation of Coal Fly Ash Obtained from Mpumalanga Province, South Africa. Research Journal of Environmental Sciences, 12(3), 98–105. https://doi.org/10.3923/rjes.2018.98.105

Alghamdi, H., Nair, S. A., Neithalath, N. (2019). Insights into material design, extrusion rheology, and properties of 3D-printable alkali-activated fly ash-based binders. Materials Design, 167, 107634. https://doi.org/10.1016/j.matdes.2019.107634

Anton, A., Reiter, L., Wangler, T., Frangez, V., Flatt, R. J., Dillenburger, B. (2021). A 3D concrete printing prefabrication platform for bespoke columns. Automation in Construction, 122, 103467. https://doi.org/10.1016/j.autcon.2020.103467

Automatic Vicat Apparatus. (n.d.). https://en.utest.uz/magazin/product/automatic-vicat-apparatus

Burciaga-Díaz, O., Escalante-García, J. I., Arellano-Aguilar, R., Gorokhovsky, A. (2010). Statistical Analysis of Strength Development as a Function of Various Parameters on Activated Metakaolin/Slag Cements. Journal of the American Ceramic Society, 93(2), 541–547. https://doi.org/10.1111/j.1551-2916.2009.03414.x

Cement and Concrete: The Environmental Impact. (2020, 3 november). PSCI. https://psci.princeton.edu/tips/2020/11/3/cement-and-concrete-the-environmental-impact

Chen, M., Li, L., Wang, J., Huang, Y., Wang, S., Zhao, P., Lu, L., Cheng, X. (2020, February). Rheological parameters and building time of 3D printing sulphoaluminate cement paste modified by retarder and diatomite. Construction and Building Materials, 234, 117391. https://doi.org/10.1016/j.conbuildmat.2019.117391

Chen, Y., He, S., Zhang, Y., Wan, Z., Çopuroğlu, O., Schlangen, E. (2021). 3D printing of calcined clay-limestone-based cementitious materials. Cement and Concrete Research, 149, 106553. https://doi.org/10.1016/j.cemconres.2021.106553

Collins, F., Sanjayan, J. Effect of pore size distribution on drying shrinking of alkali-activated slag concrete. Cem. Concr. Res., 30 (9) (2000), pp. 1401-1406.

Corazzo, I. (2021). TECLA Technology and Clay 3D Printed House. https://www.archdaily.com/960714/tecla-technology-and-clay-3d-printed-house-mario-cucinella-architects

Dai, X., Aydın, S., Yardımcı, M. Y., Lesage, K. De Schutter, G. (2022, januari). Rheology and microstructure of alkali-activated slag cements produced with silica fume activator. Cement and Concrete Composites, 125, 104303. https://doi.org/10.1016/j.cemconcomp.2021.104303

Dai, X., Aydın, S., Yardımcı, M. Y., Lesage, K., De Schutter, G. (2020). Effects of activator properties and GGBFS/FA ratio on the structural build-up and rheology of AAC. Cement and Concrete Research, 138, 106253. https://doi.org/10.1016/j.cemconres.2020.106253

Favier, A., Hot, J., Habert, G., Roussel, N., d'Espinose De Lacaillerie, J. B. (2014). Flow properties of MK-based geopolymer pastes. A comparative study with standard Portland cement pastes. Soft Matter, 10(8), 1134. https://doi.org/10.1039/c3sm51889b

Frølich, L., Wadsö, L., Sandberg, P. (2016). Using isothermal calorimetry to predict one day mortar strengths. Cement and Concrete Research, 88, 108–113. https://doi.org/10.1016/j.cemconres.2016.06.009

Fuller, W.B. and Thompson, S.E. (1907) The laws of proportioning concrete. ASCE J. Transport., Vol. 59, pp. 67-143.

Funk, J.E., Dinger, D.R. and Funk, J.E.J. (1980) Coal Grinding and Particle Size Distribution Studies for Coal-Water Slurries at High Solids Content. Final Report, Empire State Electric Energy Research Corporation (ESEERCO). New York.

Garcia-Lodeiro, I., Palomo, A., Fernández-Jiménez, A. (2015). An overview of the chemistry of alkali-activated cement-based binders. Handbook of Alkali-Activated Cements, Mortars and Concretes, 19–47. https://doi.org/10.1533/9781782422884.1.19

Glukhovsky V., (1994), 'Ancient, modern and future concretes', First International Conference Alkaline Cements and Concretes, Kiev, Ukraine, vol.1, pp. 1-8.

Gołaszewski, Jacek & Cygan, Grzegorz & Drewniok, Michal & Kilijanek, Adrian. (2014). Rheological properties of SCC in terms of its thixotropic behaviour and its influence on formwork pressure. IJRET: International Journal of Research in Engineering and Technology. 03. 170–178.

Granizo, M. L., Blanco-Varela, M. T., & Martínez-Ramírez, S. (2007). Alkali activation of metakaolins: parameters affecting mechanical, structural and microstructural properties. Journal of Materials Science, 42(9), 2934–2943. https://doi.org/10.1007/s10853-006-0565-y

Hanein, T., Thienel, K. C., Zunino, F., Marsh, A. T. M., Maier, M., Wang, B., Canut, M., Juenger, M. C. G., Ben Haha, M., Avet, F., Parashar, A., Al-Jaberi, L. A., Almenares-Reyes, R. S., Alujas-Diaz, A., Scrivener, K. L., Bernal, S. A., Provis, J. L., Sui, T., Bishnoi, S., Martirena-Hernández, F. (2021). Clay calcination technology: state-of-the-art review by the RILEM TC 282-CCL. Materials and Structures, 55(1). https://doi.org/10.1617/s11527-021-01807-6

Hasnaoui, A., Ghorbel, E., Wardeh, G. (2019). Optimization approach of granulated blast furnace slag and metakaolin based geopolymer mortars. Construction and Building Materials, 198, 10–26. https://doi.org/10.1016/j.conbuildmat.2018.11.251

He, R., Dai, N., Wang, Z. (2020). Thermal and Mechanical Properties of Geopolymers Exposed to High Temperature: A Literature Review. Advances in Civil Engineering, 2020, 1–17. https://doi.org/10.1155/2020/7532703

Hossain, A. B., Pease, B., Weiss, J. (2003). Quantifying Early-Age Stress Development and Cracking in Low Water-to-Cement Concrete: Restrained-Ring Test with Acoustic Emission. Transportation Research Record: Journal of the Transportation Research Board, 1834(1), 24–32. https://doi.org/10.3141/1834-04

Huseien, G. F., Mirza, J., Ismail, M., Ghoshal, S., Ariffin, M. A. M. (2018). Effect of metakaolin replaced granulated blast furnace slag on fresh and early strength properties of geopolymer mortar. Ain Shams Engineering Journal, 9(4), 1557–1566. https://doi.org/10.1016/j.asej.2016.11.011

Hu, X., Shi, C., Shi, Z., Zhang, L. (2019). Compressive strength, pore structure and chloride transport properties of alkali-activated slag/fly ash mortars. Cement and Concrete Composites, 104, 103392. https://doi.org/10.1016/j.cemconcomp.2019.103392

Jamali, A., Mendes, J., Nagaratnam, B., Lim, M. (2022). A new four stage model of capillary pressure in early age concrete: Insights from high capacity tensiometers. Cement and Concrete Research, 161, 106955. https://doi.org/10.1016/j.cemconres.2022.106955

Jaskulski, R., Jóźwiak-Niedźwiedzka, D., Yakymechko, Y. (2020). Calcined Clay as Supplementary Cementitious Material. Materials, 13(21), 4734. https://doi.org/10.3390/ma13214734

Jayathilakage, R. (2021). Rheology and Buildability investigation of Concrete for 3D Printing. Faculty of Science, Engineering and Technology Swinburne University of Technology Melbourne, Australia. https://researchbank.swinburne.edu.au/file/d39bc71c-6b74-4ef2-bbf5-405815e244cc/1/Roshan_Jayathilakage_Thesis.pdf

Jeon, D., Jun, Y., Jeong, Y., Oh, J. E. (2015). Microstructural and strength improvements through the use of Na2CO3 in a cementless Ca(OH)2-activated Class F fly ash system. Cement and Concrete Research, 67, 215–225. https://doi.org/10.1016/j.cemconres.2014.10.001

Kashani, A., Ngo, T. (2018). Optimisation of Mixture Properties for 3D Printing of Geopolymer Concrete. Proceedings of the International Symposium on Automation and Robotics in Construction (IAARC). https://doi.org/10.22260/isarc2018/0037

Khan S.U., Nurudin M.F., Ayub T., Shafiq N. (2014),'Effects of different mineral admixtures on the properties of fresh concrete', The Science World Journal, vol. 4.

Komljenović, M., Baščarević, Z., Marjanović, N., Nikolić, V. (2013). External sulfate attack on alkali-activated slag. Construction and Building Materials, 49, 31–39. https://doi.org/10.1016/j.conbuildmat.2013.08.013

Ł. Sadowski, Adhesion in Layered Cement Composites. Springer, 2019.

Le, T., Austin, S., Lim, S., Buswell, R., Law, R., Gibb, A., Thorpe, T. (2012). Hardened properties of high-performance printing concrete. Cement and Concrete Research, 42(3), 558–566. https://doi.org/10.1016/j.cemconres.2011.12.003

Li, C., Sun, H., Li, L. (2010). A review: The comparison between alkali-activated slag (Si+Ca) and metakaolin (Si+Al) cements. Cement and Concrete Research, 40(9), 1341–1349. https://doi.org/10.1016/j.cemconres.2010.03.020

Li, Z., Lu, T., Liang, X., Dong, H., Ye, G. (2020). Mechanisms of autogenous shrinkage of alkali-activated slag and fly ash pastes. Cement and Concrete Research, 135, 106107. https://doi.org/10.1016/j.cemconres.2020.106107

Liimatainen, H., Abdollahnejad, Z., Kinnunen, P., Illikainen, M. (2018). One-part alkali-activated materials: A review. Cement and Concrete Research, 103, 21–34. https://doi.org/10.1016/j.cemconres.2017.10.001

Ma, G., Li, Z., Wang, L. (2018). Printable properties of cementitious material containing copper tailings for extrusion based 3D printing. Construction and Building Materials, 162, 613–627. https://doi.org/10.1016/j.conbuildmat.2017.12.051

Materials – 3D Concrete Printing Weber. (z.d.). Weber.https://www.3d.weber/materials/

Mewis, J. (1979, januari). Thixotropy - a general review. Journal of Non-Newtonian Fluid Mechanics, 6(1), 1–20. https://doi.org/10.1016/0377-0257(79)87001-9

Micromeritics. Gemini VII 2390. Retrieved from https://www.micromeritics.com/gemini-vii/

Mindess S, Young JF, Darwin D (1981) Concrete. Prentice Hall, New York.

Modular Compact Rheometer: MCR 102e/302e/502e□:: Anton-Paar.com. (n.d.-b). Anton Paar. https://www.anton-paar.com/us-en/products/details/rheometer-mcr-102-302-502/

Moeini, M. A., Hosseinpoor, M., Yahia, A. (2020, October). Effectiveness of the rheometric methods to

evaluate the build-up of cementitious mortars used for 3D printing. Construction and Building Materials, 257, 119551. https://doi.org/10.1016/j.conbuildmat.2020.119551

Nair, S. A., Alghamdi, H., Arora, A., Mehdipour, I., Sant, G., Neithalath, N. (2019). Linking fresh paste microstructure, rheology and extrusion characteristics of cementitious binders for 3D printing. Journal of the American Ceramic Society, 102(7), 3951–3964. https://doi.org/10.1111/jace.16305

Nedeljkovic, M., Arbi Ghanmi, K., Zuo, Y., Ye, G. (2016). Microstructural and Mineralogical Analysis of Alkali Activated Fly Ash-Slag Pastes.

In C. Miao, W. Sun, J. Liu, H. Chen, G. Ye, K. van Breugel (Eds.), 3rd International RILEM Conference on Microstructure Related Durability of Cementitious Composites: Nanjing, China (Vol. 117, pp. 1-10). RILEM Publications S.A.R.L.

Nerella, V. N., Hempel, S., Mechtcherine, V., Technische Universität Dresden. (2017). MICRO- AND MACROSCOPIC INVESTIGATIONS ON THE INTERFACE BETWEEN LAYERS OF 3D-PRINTED CEMENTITIOUS ELEMENTS. International Conference on Advances in Construction Materials and Systems. 3-8.

Nguyen, Q. D., Afroz, S., Castel, A. (2020). Influence of Calcined Clay Reactivity on the Mechanical Properties and Chloride Diffusion Resistance of Limestone Calcined Clay Cement (LC3) Concrete. Journal of Marine Science and Engineering, 8(5), 301. https://doi.org/10.3390/jmse8050301

Odler, I. (2003). The BET-specific surface area of hydrated Portland cement and related materials. Cement and Concrete Research, 33(12), 2049–2056. https://doi.org/10.1016/s0008-8846(03)00225-4

Palomo, A., Fernández-Jiménez, A., Kovalchuk, G., Ordoñez, L. M., Naranjo, M. C. (2007). Opc-fly ash cementitious systems: study of gel binders produced during alkaline hydration. Journal of Materials Science, 42(9), 2958–2966. https://doi.org/10.1007/s10853-006-0585-7

Palomo, A., Grutzeck, M., Blanco, M. (1999). Alkali-activated fly ashes. Cement and Concrete Research, 29(8), 1323–1329. https://doi.org/10.1016/s0008-8846(98)00243-9

Panda, B., Tan, M. J. (2018). Material properties of 3D printable high-volume slag cement. Nanyang Technological University, Singapore.

Panda, B., Noor Mohamed, N. A., Paul, S. C., Bhagath Singh, G., Tan, M. J., & ŠAvija, B. (2019). The Effect of Material Fresh Properties and Process Parameters on Buildability and Interlayer Adhesion of 3D Printed Concrete. Materials, 12(13), 2149. https://doi.org/10.3390/ma12132149

Panda, B., Paul, S. C., Mohamed, N. A. N., Tay, Y. W. D., Tan, M. J. (2018). Measurement of tensile bond strength of 3D printed geopolymer mortar. Measurement, 113, 108–116. https://doi.org/10.1016/j.measurement.2017.08.051

Panda, B., Singh, G. B., Unluer, C., Tan, M. J. (2019). Synthesis and characterization of one-part geopolymers for extrusion based 3D concrete printing. Journal of Cleaner Production, 220, 610–619. https://doi.org/10.1016/j.jclepro.2019.02.185

Panda, B., Unluer, C., Tan, M. J. (2018). Investigation of the rheology and strength of geopolymer mixtures for extrusion-based 3D printing. Cement and Concrete Composites, 94, 307–314. https://doi.org/10.1016/j.cemconcomp.2018.10.002

Parkes, J. (2022, October 12). First tenants move into 3D-printed home in Eindhoven. Dezeen. https://www.dezeen.com/2021/05/06/3d-printed-home-project-milestone-eindhoven/

Perrot, A.; Rangeard, D.; Pierre, A. Structural built-up of cement-based materials used for 3D-printing extrusion techniques. Mater. Struct. 2016, 49, 1213–1220.

Priyadarshi, R. (2021, June). Shrinkage behaviour of 3D printing concrete mixture. TU Delft.

Provis, J. L., Van Deventer, J. S. J. (Eds.). (2009). Geopolymers: structures, processing, properties and industrial applications. Elsevier. R.A. Cook, K.C. Hover. Mercury porosimetry of hardened cement pastes. Cem. Concr. Res., 29 (1999), pp. 933-943.

Ravenscroft, T. (2022, October 12). World's longest 3D-printed concrete bridge opens in Shanghai. Dezeen. https://www.dezeen.com/2019/02/05/worlds-longest-3d-printed-concrete-bridge-shanghai/

Rheometers | Viscometers | Thermo Fisher Scientific - NL. (n.d.). https://www.thermofisher.com/nl/en/home/life-science/lab-equipment/rheometry-viscometry.html?cid=fl-msd-rheometers

Roussel, N., Cussigh, F. (2008). Distinct-layer casting of SCC: The mechanical consequences of thixotropy. Cement and Concrete Research, 38(5), 624–632. https://doi.org/10.1016/j.cemconres.2007.09.023

Samson, T. (2020). This image shows the structure of a concrete wall printed by a 3D robotic arm at XtreeE's workshop in Rungis, France. AFP. Getty Images. https://www.cnbc.com/2020/08/28/how-3d-printing-could-change-the-way-our-homes-are-built.html

Shi C. and Qian J. (2000), 'High performance cementing materials from industrial slags – a review', Resourc. Conserv. Recyc. 29, 195–207.

Shi, C, Krivenko, P.V., Roy, D.M. (2006). Alkali-Activated Cements and Concretes. Taylor Francis, Abingdon. https://doi.org/10.1201/9781482266900

Shvarzman, A., Kovler, K., Grader, G., Shter, G. (2003). The effect of dehydroxylation/amorphization degree on pozzolanic activity of kaolinite. Cement and Concrete Research, 33(3), 405–416. https://doi.org/10.1016/s0008-8846(02)00975-4

Sousa, G. (2017, 25 April). Top 12 Kaolin Exporting Countries. WorldAtlas. Geraadpleegd op 17 mei 2022, van https://www.worldatlas.com/articles/top-12-kaolin-exporting-countries.html

Srinivas, K., Padmakar, M., Barhmaiah, B., Vijaya, S. K. (2020). EFFECT OF ALKALINE ACTIVATORS ON STRENGTH PROPERTIES OF METAKAOLIN AND FLY ASH BASED GEOPOLYMER CONCRETE. Journal of Critical Reviews, 7(13).

Stoleriu, S., Vlasceanu, I. N., Dima, C., Badanoiu, A. I., Voicu, G. (2019). Alkali activated materials based on glass waste and slag for thermal and acoustic insulation. Materiales De Construcción, 69(335), 194. https://doi.org/10.3989/mc.2019.08518

TURNING WASTE CONCRETE INTO 3D-PRINTED PUBLIC FURNITURE MATERIALDISTRICT. (2020, 25 november). [Photograph]. Material District. https://materialdistrict.com/article/turning-waste-concrete-into-3d-printed-public-furniture/turning-waste-concrete-into-3d-printed-publi

Van Overmeir, A. L. (2020). Designing an interlayer reinforcement solution for printable strain-hardening cement-based composites. TU Delft.

Vollpracht, A. (2018, januari). Isothermal calorimetry and in-situ XRD study of the NaOH activated fly ash, metakaolin and slag. Cement and Concrete Research, 103, 110–122. https://doi.org/10.1016/j.cemconres.2017.10.004

Wang, S. D., Pu, X. C., Scrivener, K. L., Pratt, P. L. (1995). Alkali-activated slag cement and concrete: a review of properties and problems. Advances in Cement Research, 7(27), 93–102. https://doi.org/10.1680/adcr.1995.7.27.93

Warburton, R. (2019). Carbon dioxide emissions by business sector. [Graph]. Global warming has concrete problem when it comes to CO2. https://www.ecori.org/climate-change/2019/10/4/global-warming-has-a-co2ncrete-problem

Wolfs, R., Bos, F., Salet, T. (2018). Early age mechanical behaviour of 3D printed concrete: Numerical modelling and experimental testing. Cement and Concrete Research, 106, 103–116. https://doi.org/10.1016/j.cemconres.2018.02.001

Wolfs, R., Bos, F., Salet, T. (2019). Hardened properties of 3D printed concrete: The influence of process parameters on interlayer adhesion. Cement and Concrete Research, 119, 132–140. https://doi.org/10.1016/j.cemconres.2019.02.017

Y. Chen, C.R. Rodriguez, Z. Li, B. Chen, O. Çopuroglu, E. Schlangen, Effect of different grade levels of calcined clays on fresh and hardened properties of ternary-blended cementitious materials for 3D printing, Cem. Concr. Compos. 114 (2020), 103708, https://doi.org/10.1016/j.cemconcomp.2020.103708

Y.W.D. Tay, Y. Qian, M.J. Tan, Printability region for 3D concrete printing using slump and slump flow test, Compos. Part B Eng. 174 (2019), 106968, https://doi.org/10.1016/j.compositesb.2019.106968

Ye, H., Cartwright, C., Rajabipour, F., Radlińska, A. (2017). Understanding the drying shrinkage performance of alkali-activated slag mortars. Cement and Concrete Composites, 76, 13–24. https://doi.org/10.1016/j.cemconcomp.2016.11.010

Zareiyan, B., Khoshnevis, B. (2017). Interlayer adhesion and strength of structures in Contour Crafting - Effects of aggregate size, extrusion rate, and layer thickness. Automation in Construction, 81, 112–121. https://doi.org/10.1016/j.autcon.2017.06.013

Zhou, D., Wang, R., Tyrer, M., Wong, H., Cheeseman, C. (2017). Sustainable infrastructure development through use of calcined excavated waste clay as a supplementary cementitious material. Journal of Cleaner Production, 168, 1180–1192. https://doi.org/10.1016/j.jclepro.2017.09.098

Zhou, W., McGee, W., Zhu, H., Gökçe, H. S., Li, V. C. (2022, October). Time-dependent fresh properties characterization of 3D printing engineered cementitious composites (3DP-ECC): On the evaluation of buildability. Cement and Concrete Composites, 133, 104704. https://doi.org/10.1016/j.cemconcomp.2022.104704

A

Target value for the shrinkage (NEN-EN 1992-1-1)

Calculation of the shrinkage according to NEN-EN1992-1-1

Fictitious properties of printed concrete			
Fictitious width of the cross-section	40	mm	(h_o)
Characteristics of the printable mortar			
E-modulus W160-3D	30000	N/mm^2	(Weber mechanical properties W160)
$f_{ck,cube}$	56	N/mm^2	(Weber mechanical properties W160)
f_{ck}	44,8	N/mm^2	f_{ck}=0,8*$f_{ck,cube}$
Coefficient of expansion	0,00001		
Characteristics of the environment			
RH	80	%	Relative humidity

Shrinkage (autogenous + drying)					
Shrinkage	case 1		case 2		*target value will be based on case 2*
Shrinkage (Weber, 91d)	1,00	mm/m	1,0	mm/m	
Time in days (t-t_s)	**91,0**	days	**28,0**	days	
$\beta_{ds}(t,t_s)$	0,900		0,7		$\beta_{ds}(t,t_s) = (t - t_s) / [(t - t_s) + 0.04 \cdot h_0^{3/2}]$
k_h	4,30		4,30		*k_h is chosen to fit the data*
$e_{cd,o}$	0,000239		0,000239		*Chosen based on table below*
$e_{cd}(t)$ (drying shrinkage)	0,00093	m/m	0,00076	m/m	$\varepsilon_{cd}(t) = \beta_{ds}(t,t_s) \cdot k_h \cdot \varepsilon_{cd,0}$
Total drying shrinkage	0,926	mm/m	0,756	mm/m	
$\beta_{as}(t)$	0,852		0,653		$\beta_{as}(t) = 1 - \exp(-0.2 \cdot t^{0.5})$
$e_{ca}(\infty)$	0,000087		0,000087		$\varepsilon_{ca}(\infty) = 2.5 \cdot (f_{ck} - 10\ \text{MPa}) \cdot 10^{-6}$
$e_{ca}(t)$	0,000074	m/m	0,000057	m/m	$\varepsilon_{ca}(t) = \beta_{as}(t) \cdot \varepsilon_{ca}(\infty)$
Total autogenous shrinkage	0,074	mm/m	0,057	mm/m	
Total shrinkage	**1,000**	**mm/m**	**0,813**	**mm/m**	$\varepsilon_{cs} = \varepsilon_{cd} + \varepsilon_{ca}$

f_{ck}	MPa	20	25	30	35	40	50
$f_{cm} = (f_{ck} + 8)$	MPa	28	33	38	43	48	58
$f_{ctm} = (0{,}3\ f_{ck}^{(2/3)} \le$ C50/60	MPa	2,21	2,56	2,90	3,21	3,51	4,07
$E_{cm} = (22\ [(f_{cm})/10]^{0{,}3}$	GPa	30,0	31,5	32,8	34,1	35,2	37,3
$E_{c28} = (1{,}05\ E_{cm})$	GPa	31,5	33,0	34,5	35,8	37,0	39,1
$\varepsilon_{cd,0}$ klasse CEM R, HR = 50 %	x 10^{-6}	746	706	668	632	598	536
$\varepsilon_{cd,0}$ klasse CEM R, HR = 80 %	x 10^{-6}	416	394	372	353	334	299
$\varepsilon_{cd,0}$ klasse CEM N, HR = 50 %	x 10^{-6}	544	512	482	454	428	379
$\varepsilon_{cd,0}$ klasse CEM N, HR = 80 %	x 10^{-6}	303	286	269	253	239	212
$\varepsilon_{cd,0}$ klasse CEM S, HR = 50 %	x 10^{-6}	441	413	387	363	340	298
$\varepsilon_{cd,0}$ klasse CEM S, HR = 80 %	x 10^{-6}	246	230	216	202	189	166
$\varepsilon_{ca}(\infty)$	x 10^{-6}	25	38	50	63	75	100

According to German National Annex to EN1992-1-1, Class S corresponds to slow hardening cements, Class N corresponds to normal or fast hardening cements, and Class R corresponds to fast hardening and high strength cements.

Assumption: normal or fast hardening cement (N)

$e_{cd,o}$ = 239*10^{-6} m/m

B

Flow curves

B.1. Flow curve and fitted curve for CC0S100-1

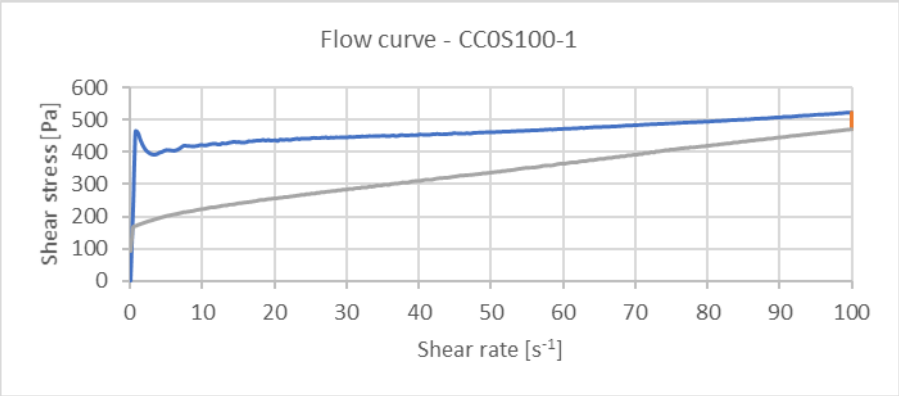

Figure B.1: Flow curve CC0S100-1

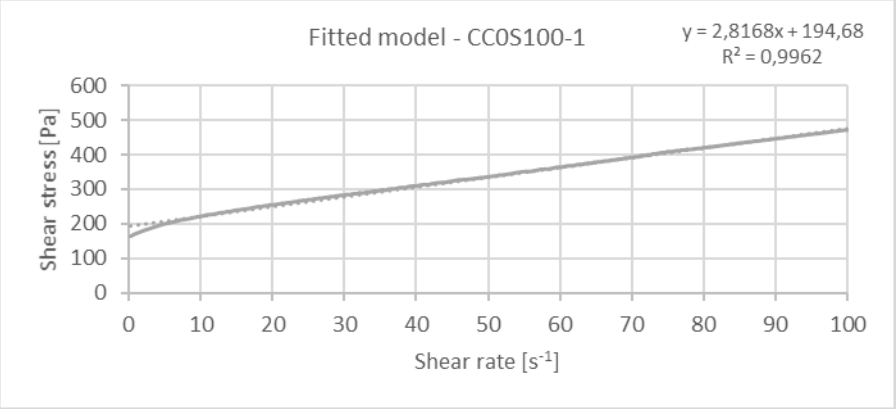

Figure B.2: Fitted curve CC0S100-1

B.2. Flow curve and fitted curve for CC0S100-2

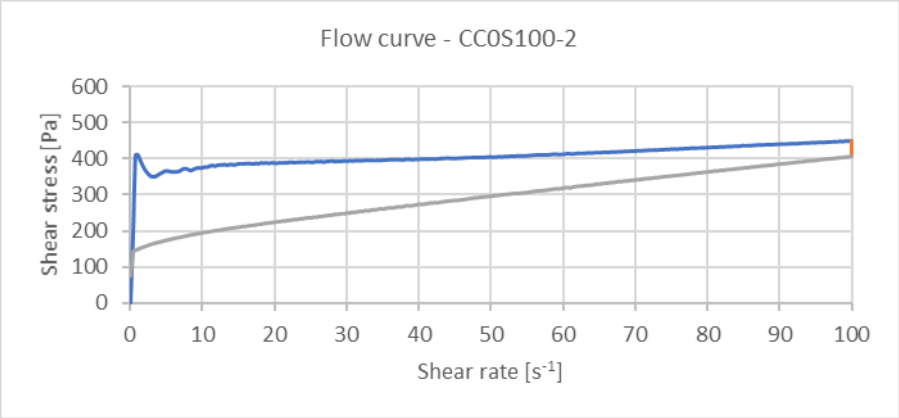

Figure B.3: Flow curve CC0S100-2

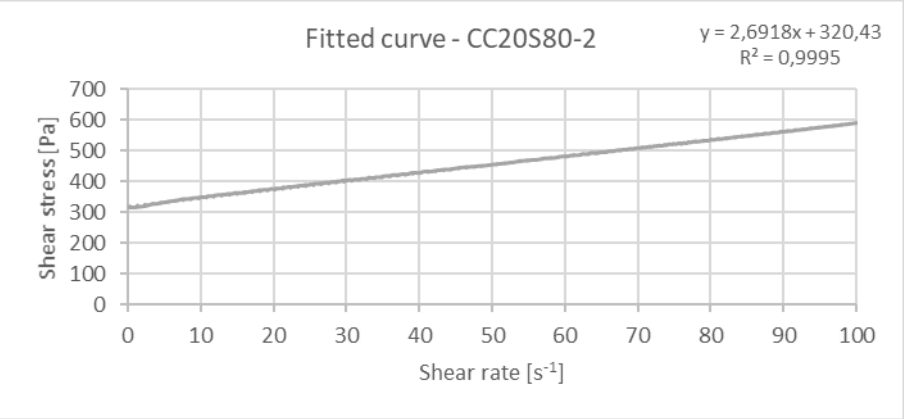

Figure B.4: Fitted curve CC0S100-2

B.3. Flow curve and fitted curve for mixture CC10S90-1

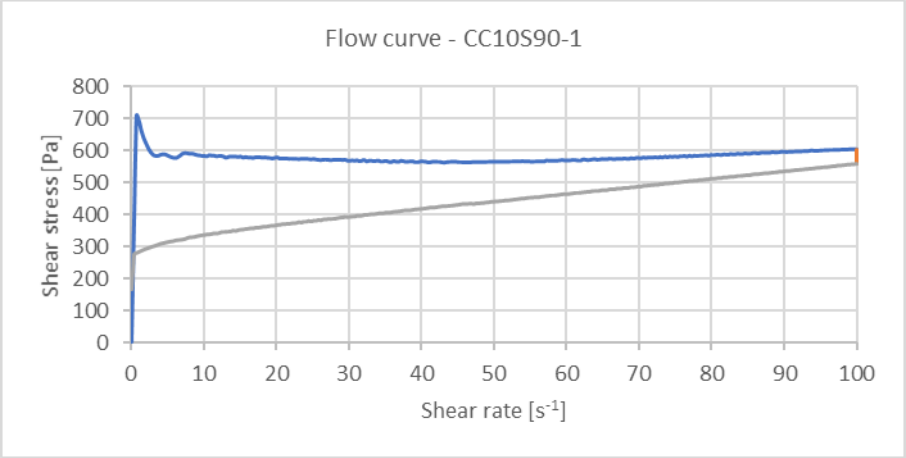

Figure B.5: Flow curve CC10S90-1

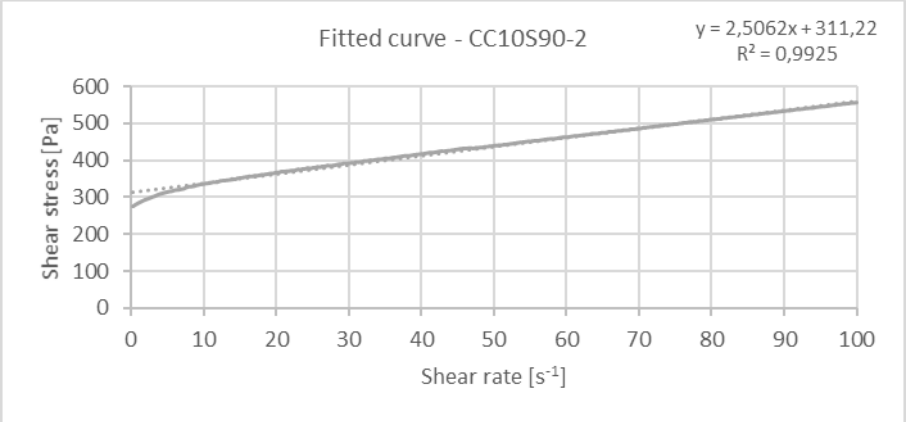

Figure B.6: Fitted curve CC10S90-1

B.4. Flow curve and fitted curve for CC10S90-2

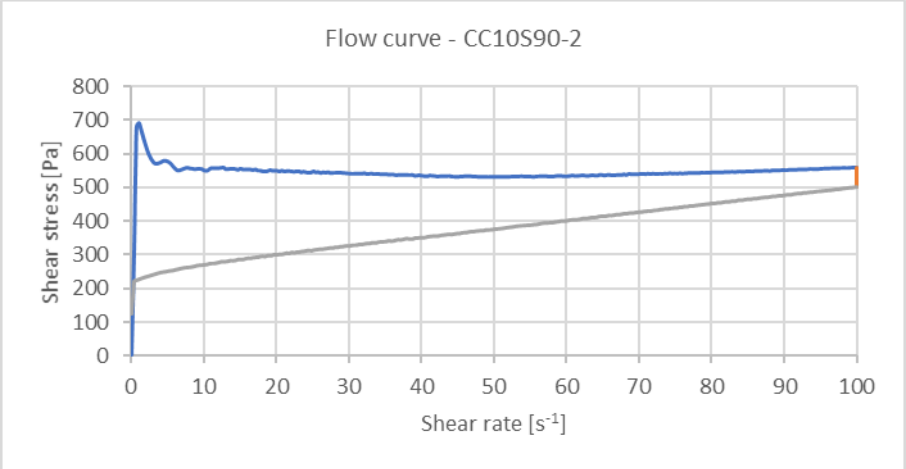

Figure B.7: Flow curve CC10S90-2

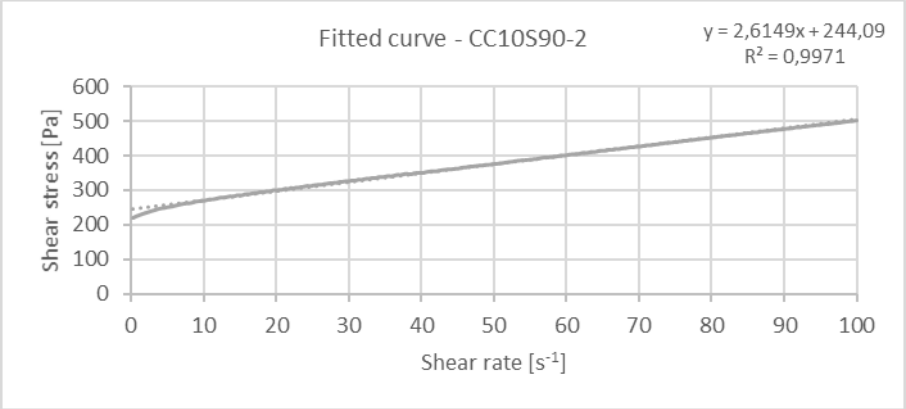

Figure B.8: Fitted curve CC10S90-2

B.5. Flow curve and fitted curve for CC20S80-1

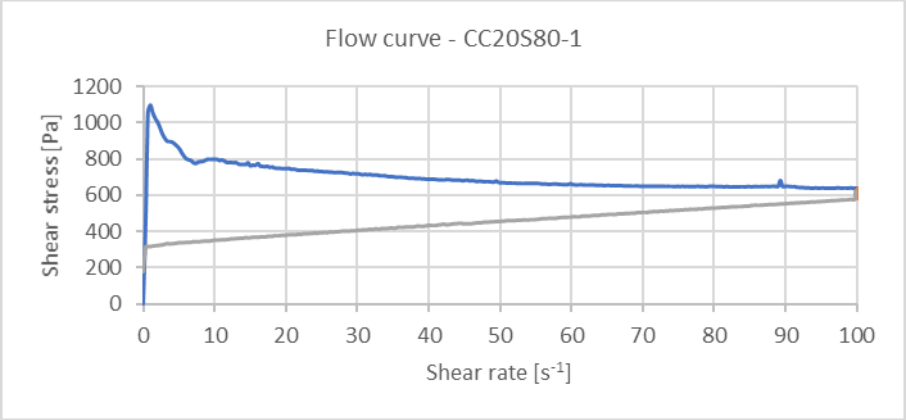

Figure B.9: Flow curve CC20S80-1

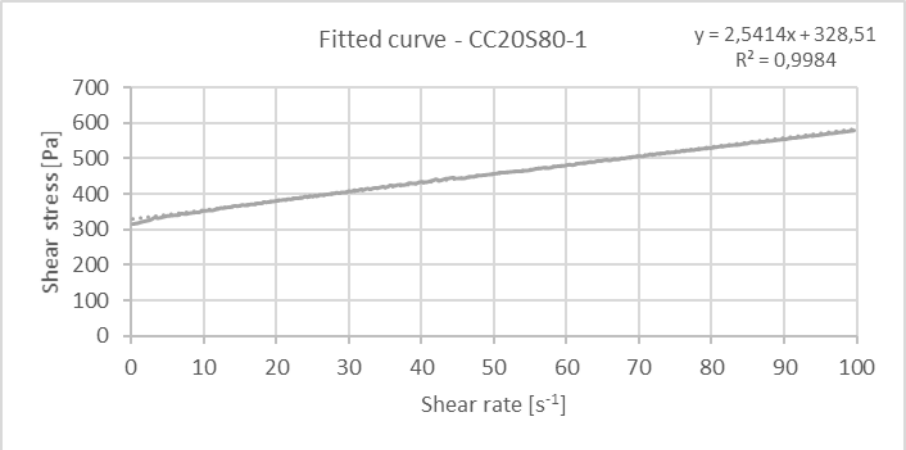

Figure B.10: Fitted curve CC20S80-1

B.6. Flow curve and fitted curve for CC20S80-2

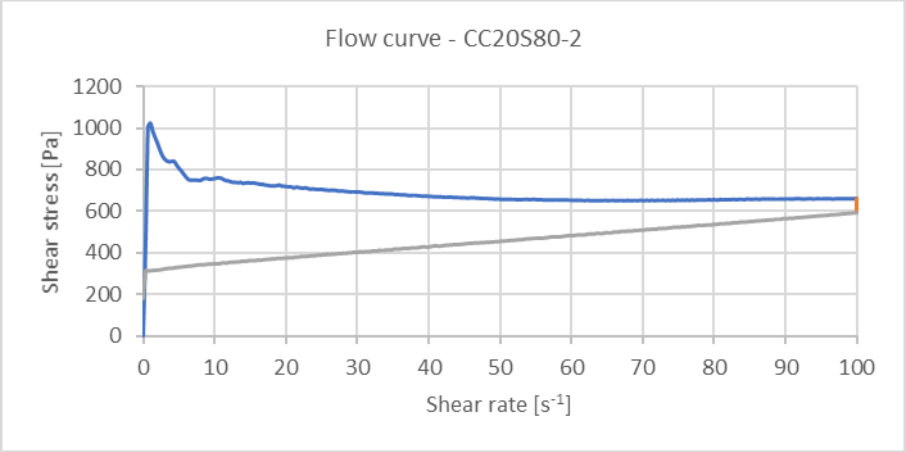

Figure B.11: Flow curve CC20S80-2

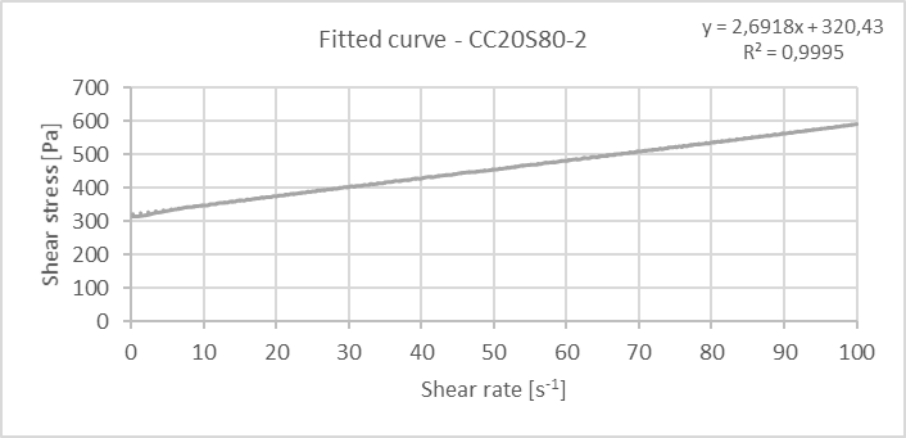

Figure B.12: Fitted curve CC20S80-2